



Forschungszentrum Karlsruhe
in der Helmholtz-Gemeinschaft

Wissenschaftliche Berichte
FZKA 7209

**Spectral resolved
Measurement of the Nitrogen
Fluorescence Yield in Air
induced by Electrons**

T. Waldenmaier
Institut für Kernphysik

April 2006

Forschungszentrum Karlsruhe

in der Helmholtz-Gemeinschaft

Wissenschaftliche Berichte

FZKA 7209

Spectral resolved Measurement of the Nitrogen Fluorescence Yield in Air induced by Electrons

Tilo Waldenmaier

Institut für Kernphysik

Von der Fakultät für Physik
der Universität Karlsruhe (TH)
genehmigte Dissertation

Forschungszentrum Karlsruhe GmbH, Karlsruhe

2006

Für diesen Bericht behalten wir uns alle Rechte vor

Forschungszentrum Karlsruhe GmbH
Postfach 3640, 76021 Karlsruhe

Mitglied der Hermann von Helmholtz-Gemeinschaft
Deutscher Forschungszentren (HGF)

ISSN 0947-8620

urn:nbn:de:0005-072092

Abstract

For the calorimetric determination of the primary energy of extensive air showers, measured by fluorescence telescopes, a precise knowledge of the conversion factor (fluorescence yield) between the deposited energy in the atmosphere and the number of emitted fluorescence photons is essential. The fluorescence yield depends on the pressure and the temperature of the air as well as on the water vapor concentration.

Within the scope of this work the “AirLight” experiment has been built up to measure the nitrogen fluorescence yield in air. The fluorescence yields of the eight strongest nitrogen bands have been measured for electron energies between 250 keV and 2000 keV and pressures ranging from 5 hPa to 1000 hPa. Furthermore, the influence of water vapor has been investigated. A new approach for the parametrisation of the fluorescence yield has been chosen, taking into account all the physical relations between the single nitrogen bands. The global fit of the parametrisation to the measured data, leads to a consistent description of the fluorescence yield with a minimal set of parameters.

The resulting absolute accuracies for the single nitrogen bands are between 13 % and 15 % and are thus of the same order as the best present measurements. In the investigated energy range, the fluorescence yield proved to be independent of the energy of the ionizing electrons. This implies the number of emitted photons to be proportional to the deposited energy in the atmosphere.

Spektral aufgelöste Messung der durch Elektronen induzierten Stickstoff Fluoreszenz in Luft

Zur kalorimetrischen Bestimmung der Primärenergie ausgedehnter Luftschauer, die durch Fluoreszenzteleskope nachgewiesen wurden, ist eine genaue Kenntnis des Umrechnungsfaktors (Fluoreszenzausbeute) zwischen in der Atmosphäre deponierter Energie und der Anzahl der emittierten Fluoreszenzphotonen erforderlich. Die Fluoreszenzausbeute hängt hierbei vom Druck und der Temperatur der Luft ab und wird zusätzlich durch die Luftfeuchtigkeit beeinflusst.

Im Rahmen dieser Arbeit wurde zur Messung der Fluoreszenzausbeute von Stickstoff in Luft das „AirLight“-Experiment aufgebaut. Die Fluoreszenzausbeuten der acht intensivsten Stickstoffbanden wurden für Elektronenenergien zwischen 250 keV und 2000 keV und Drücke zwischen 5 hPa und 1000 hPa bestimmt sowie der Einfluss von Wasserdampf untersucht. Zur Parametrisierung der Fluoreszenzausbeute wurde ein neuer Ansatz gewählt, der die physikalischen Beziehungen zwischen den einzelnen Banden berücksichtigt. Durch eine globale Anpassung an die gemessenen Daten wurde somit eine konsistente Beschreibung der Fluoreszenzausbeute mit einem minimalen Satz von Parametern möglich.

Die absolute Genauigkeit der Ergebnisse für die einzelnen Banden liegt zwischen 13 % und 15 % und ist somit vergleichbar mit den besten bisherigen Messungen. Im untersuchten Energiebereich erwies sich die Fluoreszenzausbeute als unabhängig von der Energie der Elektronen, d.h. die emittierte Photonenzahl ist proportional zur deponierten Energie in der Atmosphäre.

Contents

Abstract	i
1 Cosmic Rays and Fluorescence Detection	1
1.1 Cosmic Radiation	1
1.1.1 Composition	1
1.1.2 Energy Spectrum	3
1.2 Extensive Air Showers	5
1.3 The Pierre Auger Observatory	6
1.4 Fluorescence Detection of Extensive Air Showers	9
2 Nitrogen Fluorescence in Air	13
2.1 Molecular Spectra	13
2.1.1 Rotational States of Diatomic Molecules	15
2.1.2 Vibrational States of Diatomic Molecules	16
2.1.3 Electronic States of Diatomic Molecules	17
2.1.4 Molecular Transitions and the Franck-Condon-Principle	19
2.2 The Spectrum of Molecular Nitrogen	24
2.3 Modelling Nitrogen Fluorescence in Air	24
2.3.1 Excitation	26
2.3.2 De-Excitation	27
2.3.3 Quenching	28
2.3.4 Total Fluorescence Yield	30
3 The AirLight Experiment	33
3.1 Experimental Setup	33
3.1.1 Electron Source Module	35
3.1.2 Electron Detector Module	36
3.1.3 Photon Detector Module	37
3.2 Filters	38
3.3 Gas System and Sensors	41
3.4 Data Acquisition	43
3.4.1 Coincidence Logic	44
3.4.2 Experimental Control	48

3.4.3	Data Format	51
3.5	Calibration	51
3.5.1	Energy Calibration	52
3.5.2	Time Calibration	57
3.5.3	Photoelectron Conversion	58
3.5.4	Relative Calibration of the Photomultipliers	58
3.6	Background Measurements	63
3.6.1	Background in the Photon Detectors	64
3.6.2	Background in the Electron Detector	67
4	GEANT4 Simulations	69
4.1	Program Structure	69
4.1.1	Detector Construction	70
4.1.2	Physics List	70
4.2	Electron Energy Spectrum	72
4.2.1	Detected Energy Spectrum	74
4.3	Energy Deposit in Chamber	75
4.4	Photon Angular Distribution	77
5	Measurement and Data Analysis	79
5.1	Datasets Used	79
5.2	Analysis Procedure	81
5.2.1	Time Distributions	83
5.2.2	General Minimization Function	84
5.2.3	Data Acquisition Efficiency	86
5.2.4	Detection Efficiencies	87
5.2.5	Starting Values and optimal Fit Range	89
5.3	Study of Nitrogen Quenching in different Gas Mixtures	91
5.4	Study of Humidity Effects	99
5.5	Study of Energy Dependence of the Fluorescence Yields	101
5.6	Results and Discussion	105
6	Summary and Outlook	113
	Acknowledgements	115
	Bibliography	117

Chapter 1

Cosmic Rays and Fluorescence Detection

1.1 Cosmic Radiation

Almost one century has passed, since in 1912 Viktor Hess has undertaken his balloon flights at very high altitudes to understand the nature of the ionizing radiation which has been measured at the Earth's surface [25]. Up to this point, the radiation measured at ground had completely been attributed to the natural radioactivity of the Earth. If this was the case, the intensity of the radiation should decrease with higher altitudes, but Viktor Hess observed a totally contrary behavior. Therefore he concluded that the measured radiation must originate from the outer space. The concept of "cosmic radiation" finally was introduced by Millikan, since initially the cosmic radiation was interpreted as pure γ radiation. Today the cosmic radiation is known to consist mostly of light atomic nuclei. Before the era of the big particle accelerators began, the cosmic radiation was the only possibility to do particle physics at higher energies and a lot of outstanding discoveries as, for instance, the discovery of the positron [5] have been made. These days cosmic ray research experiences a renaissance since it provides particles at ultra-high energies far beyond the energies of the man-made particle accelerators. The mechanism of acceleration to these ultra-high energies still is an open topic of discussion and several new experiments as, for instance, the Pierre Auger Observatory are currently under construction to answer some of these questions.

1.1.1 Composition

At low energy, the composition of cosmic rays can be directly measured by space- or balloon-borne experiments. In Fig. 1.1 the relative abundances of the cosmic rays for energies smaller than 2 GeV/nucleon are compared to the abundances in our solar system. Both graphs show the same fluctuations between elements with even or odd atomic numbers and in most cases are in fair agreement to each other. This leads to the assumption that, at least for low energies, cosmic rays consists of stellar matter. Nevertheless, there are two significant

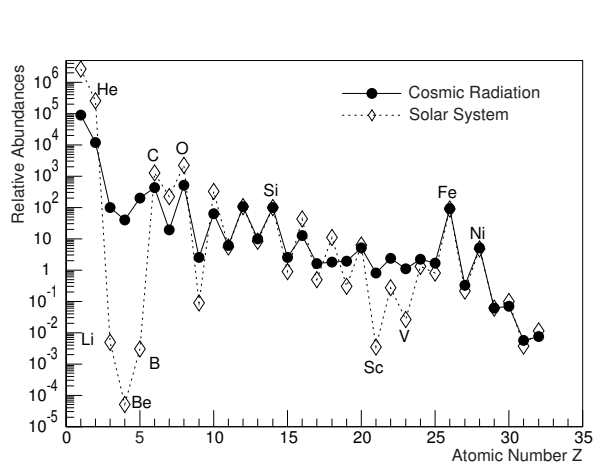


Fig. 1.1: Chemical composition of low energy ($E < 2$ GeV/nucleon) cosmic radiation compared to the composition of the solar system normalized to 100 at Si [47].

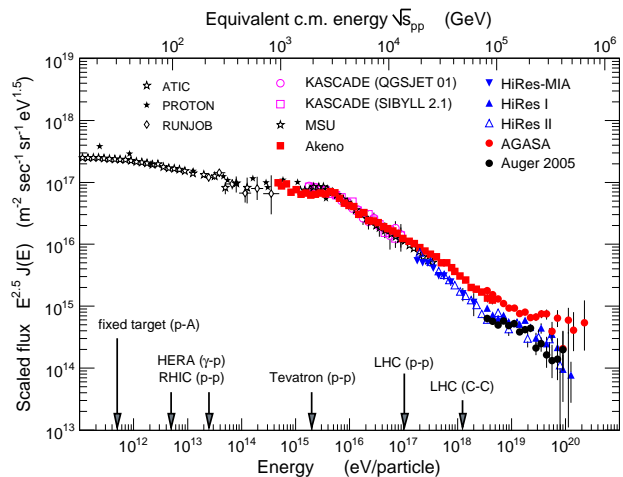


Fig. 1.2: Total flux of the primary cosmic radiation versus the energy as measured by several experiments [16].

deviations between the two curves. At first the elements hydrogen and helium seem to be less abundant in the cosmic radiation. This is not completely understood, but it may be due to the relatively large values of their first ionization potentials compared to the other elements. Therefore the acceleration of hydrogen and helium is less effective as of other elements. This effect is also responsible for some of the smaller deviations between the other elements. A second strong deviation, but the other way around, can be seen for the Li-Be-B group and some elements below iron. The abundances of these elements exceed the solar abundances by several orders of magnitudes. These deviations are well understood for the reason that these elements are not produced by the stellar nucleosynthesis. Instead of that they emerge from spallation processes at collisions of carbon, oxygen and iron nuclei with the interstellar matter. Since the cross-sections of the spallation processes are known from laboratory experiments, it is possible to estimate the amount of traversed matter by means of the differences between the abundances of these elements. These considerations lead to an amount of $X = 5 - 10$ g/cm² of traversed interstellar matter for most of the elements in the cosmic radiation. Since the density ρ of our galaxy is in the order of one proton per cm³, the totally covered distance of the cosmic particles before reaching our detectors follows to be [19]

$$l = \frac{X}{m_p \rho} \approx 3 \times 10^{24} \text{ cm} \approx 1000 \text{ kpc}^1 \quad (1.1)$$

Since the galactic disc just has a diameter of roughly 30 kpc and a width of 0.3 kpc, the particles of the low energetic cosmic rays are assumed to diffuse over a very long period through the Galaxy or the outer halo before they will somewhere be stopped or detected on Earth.

¹1 parsec (pc) = 3.26 light years

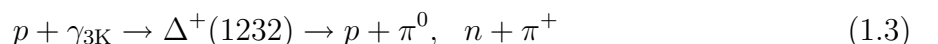
1.1.2 Energy Spectrum

The energy spectrum of the overall flux of the cosmic radiation is illustrated in Fig. 1.2. The energies of cosmic rays are spanning over 12 orders of magnitudes, reaching from a few MeV to roughly 100 EeV (10^{20} eV), which have been measured so far. The flux of the cosmic radiation varies by more than 30 decades over this energy range. Due to this steep fall of the particle flux, a direct measurement in balloon- or space-borne experiments is only possible for energies below 10^{14} eV. At higher energies cosmic radiation can only be measured indirectly by means of extensive air showers. The highest energies of cosmic rays are a hundred million times larger compared to fixed target experiments and incorporate tens of joules in a single particle or nucleus [12]. Thus, apart from astrophysical considerations, the cosmic radiation provides the only possibility to study particle interactions at energies beyond the energies which can be reached by accelerators. The shape of the energy spectrum is described by a broken power law

$$\frac{dN}{dE} \propto E^{-\gamma} \quad , \quad \gamma \approx \begin{cases} 2.75 & , E \leq 10^{15} \text{ eV} \\ 3.05 & , 10^{15} \text{ eV} \leq E \leq 10^{19} \\ 2.75 & , 10^{19} \text{ eV} \leq E \end{cases} \quad (1.2)$$

with slightly different spectral indices γ depending on the energy region. For better visibility of these regions the flux in Fig. 1.2 has been scaled by $E^{2.5}$. The changing of the spectral indices leads to the bending of the energy spectrum. The first sharp bend at $\sim 4 \times 10^{15}$ eV (4 PeV) is called the “knee”, where the flux is of about one particle per m^2 and year. Very likely the knee is caused by a change in the chemical composition from light to heavier elements [45, 28], which has been found by the KASCADE experiment. Nevertheless, there are also other possible scenarios, as for instance different acceleration mechanisms for particles with energies below and above the knee, a transition from galactic to extragalactic radiation or even unknown physical effects. Above $\sim 5 \times 10^{18}$ eV the index is again decreasing to a value of ~ 2.75 . This is the co-called “ankle” of the cosmic ray energy spectrum. In this energy region the particle flux becomes less than one particle per km^2 and year. The ankle may be caused by the cross-over of an extragalactic component with the decreasing galactic component of the energy spectrum.

The energy region around 5×10^{19} eV currently has been of very large interest. At this energy the so-called Greisen-Zatsepin-Kuz'min-effect (GZK-effect) [21, 48] should lead to a sudden drop in the spectrum, if the particles are of extragalactic origin. The GZK-effect describes the interaction of ultra-high energy cosmic rays with the photons of the cosmic microwave background. The mean energy of the background photons is only 0.7 meV in our reference system, but they appear strongly blue shifted in the rest frame of an ultra-high energy cosmic ray particle. If the particle energy exceeds 5×10^{19} eV, which corresponds to the threshold of pion production, processes like



turn out to be possible, which lead to an effective energy loss or the disintegration of the proton. Another important interaction mechanism is given by the Bethe-Heitler pair production

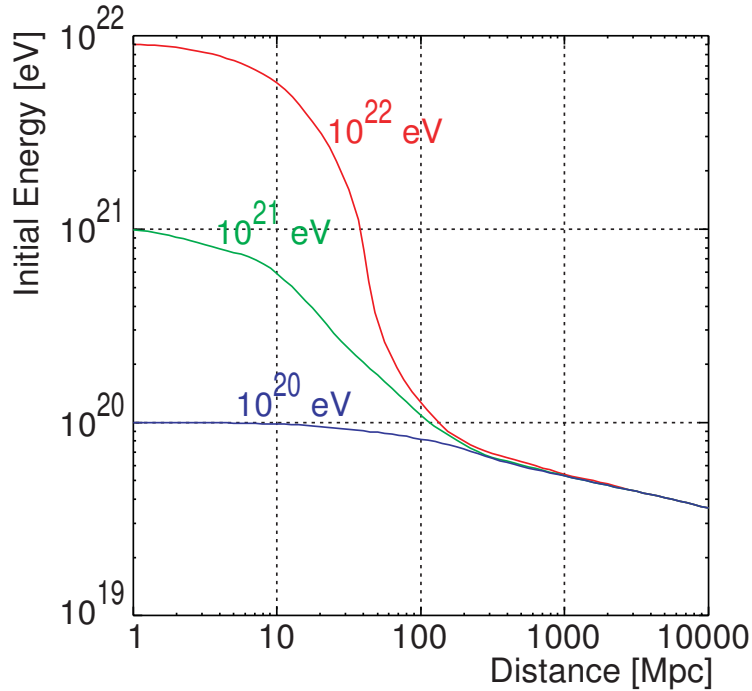
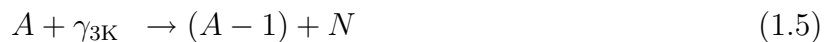


Fig. 1.3: Proton energy as a function of travelled distance through the microwave background for different initial energies [4].

according to



with an energy threshold of about 8×10^{18} eV. Nuclei with mass numbers A suffer energy losses either due to photo-disintegration or pair production, for example,



where N denotes a single nucleon. When ultra-high energy cosmic ray particles are travelling through the space, they will be effectively slowed down by these processes until their energies drop below the corresponding energy thresholds. This happens almost independently from the initial energy after a travelled distance of roughly 100 Mpc, as is shown in Fig. 1.3. Therefore the cosmic ray energy spectrum is expected to be cut-off around an energy of 5×10^{19} eV, if the ultra-high energy cosmic ray particles are assumed to originate from very far sources. At the moment there is a discordance about the existence of this so-called GZK-cut-off. The AGASA [42] data in Fig. 1.2 seem to be consistent with a continuing energy spectrum, but the HiRes [43] is compatible with the existence of the cut-off. The statistics of the Pierre Auger data [31] is not yet sufficient to make a statement to this question.

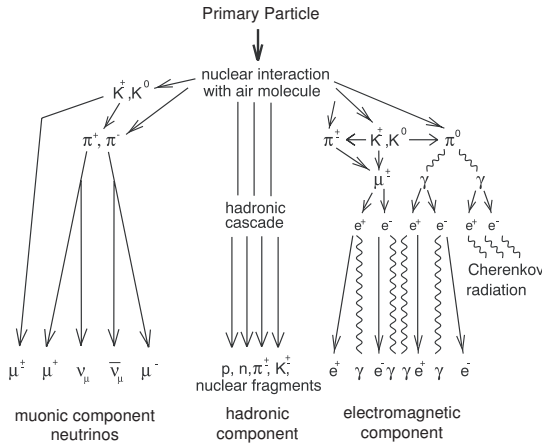


Fig. 1.4: Sketch of the different components in an extensive air shower.

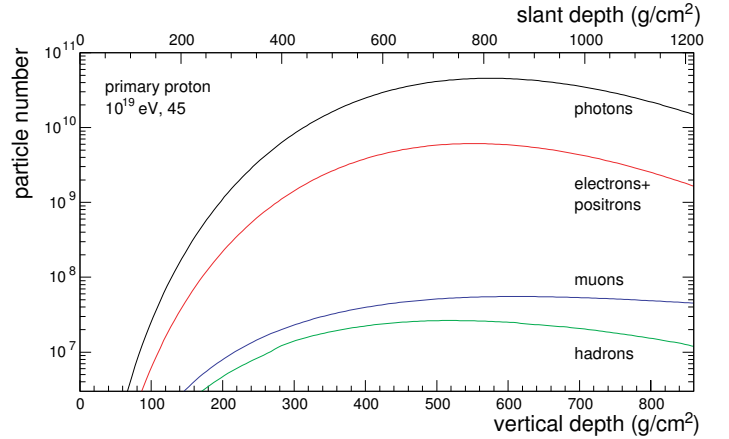


Fig. 1.5: Longitudinal profile showing the proportions of particles within an extensive air shower [39].

1.2 Extensive Air Showers

Twenty-six years after the discovery of the cosmic radiation, in 1938 Pierre Auger [6] and others discovered the existence of extensive air showers (EAS) initiated by the interaction of very high energy cosmic rays with the Earth's atmosphere. The measurement of EAS turned out to be the only method for the detection of cosmic rays with energies higher than 10^{14} eV. By collision of a primary cosmic ray particle with an atom or a molecule of the atmosphere, the particles can undergo all kinds of nuclear reactions leading to the production of nuclear fragments or secondary particles. The secondary products of the first interactions again interact with the molecules of the atmosphere, emitting further secondary particles. This cascade process is repeated until the energy of the secondary particles reaches the energy thresholds of the different processes. In this way the particle multiplicity is increasing dramatically, leading to several million or billion of secondary particles which are heading towards the earth's surface with almost the speed of light. The first interaction of the primary cosmic ray with the atmosphere typically occurs at a height of 20 - 30 km, depending on the energy and the mass of the primary particle. As is shown in Fig. 1.4, an EAS typically is composed by three components.

The hadronic component is the backbone of the EAS, which is feeding the other shower components through the decay of secondary hadrons. The highest energetic hadron of the first interaction is called the leading hadron. It typically reaches the ground after an average of 12 interactions. The hadronic processes can be schematically summarized as

$$N_{\text{CR}} + N_{\text{Air}} \longrightarrow N'_{\text{CR}} + N'_{\text{Air}} + \pi^0, \pi^\pm, K^0, K^\pm, \eta, p, n, \Lambda, \dots \quad (1.7)$$

where N_{CR} denotes the primary or the secondary particles of the cosmic radiation and N_{Air} stands for a nucleus of the atmosphere. Most of the secondary particles ($\sim 65\%$) of the hadronic component consist of charged or neutral pions.

The muonic component of an EAS emerges from the decay of the secondary pions and

kaons of the hadronic component according to

$$\pi^\pm \longrightarrow \mu^\pm + \nu_\mu(\bar{\nu}_\mu) \quad (\tau_0 = 2.6 \times 10^{-8} \text{ s}) \quad (1.8)$$

$$K^\pm \longrightarrow \mu^\pm + \nu_\mu(\bar{\nu}_\mu) \quad (\tau_0 = 1.2 \times 10^{-8} \text{ s}) \quad (1.9)$$

where the lifetimes τ_0 refer to the rest frame of the pions or kaons. Also the muons are unstable particles and decay after a lifetime of 2.2×10^{-6} s into electrons or positrons, which then contribute to the electromagnetic component. Since the lifetime of the muons exceeds the lifetime of the pions and kaons about one hundred times, most of the muons will reach the Earth before they decay. Due to the large mass of the muons they nearly do not interact with the molecules of the atmosphere and thus travel almost on straight trajectories towards the ground. Thus the most energetic muons carry information about the primary energy and the very first interactions in an EAS.

The electromagnetic component of a hadron induced EAS essentially originates from the decay of the neutral mesons, mainly pions, according to the following reactions

$$\begin{aligned} \pi^0 &\longrightarrow \gamma + \gamma && (\sim 98.8\%) \\ \pi^0 &\longrightarrow e^+ + e^- + \gamma && (\sim 1.2\%) \end{aligned} \quad (1.10)$$

where the branching ratios of the two decay channels are given in the brackets. The lifetime of neutral pions amounts to $\tau_0 = 8.4 \times 10^{-17}$ s. Pure electromagnetic cascades can also be initiated directly by high energy photons or electrons. Through the interplay of pair production and Bremsstrahlung an electromagnetic cascade begins to develop. In the electromagnetic field of a nucleus N the pair production proceeds as follows:

$$\gamma + N \longrightarrow N + e^- + e^+ \quad (1.11)$$

On the other hand the Bremsstrahlung process

$$e^\pm + N \longrightarrow N + e^\pm + \gamma \quad (1.12)$$

leads to the emission of further photons, which afterwards again may produce additional e^\pm -pairs. This chain reaction proceeds until the energy of the electrons and positrons drops below the critical energy $E_c = 85.1$ MeV in air, where the ionization energy loss starts to dominate the Bremsstrahlung process.

Most of the charged particles in an EAS are electrons and positrons, as is shown in the longitudinal profile in Fig. 1.5 from the simulation of a proton induced, inclined air shower with a primary energy of 10^{19} eV. Therefore also most of the energy of the primary particle is finally transferred to the electromagnetic component. Part of this energy is released to the atmospheres and leads to the emission of fluorescence light, which can be measured at ground.

1.3 The Pierre Auger Observatory

The Pierre Auger Observatory [2] aims for the measurement of cosmic rays at energies above 10^{18} eV. There are a lot of interesting physical aspects in this ultra-high energy region. The

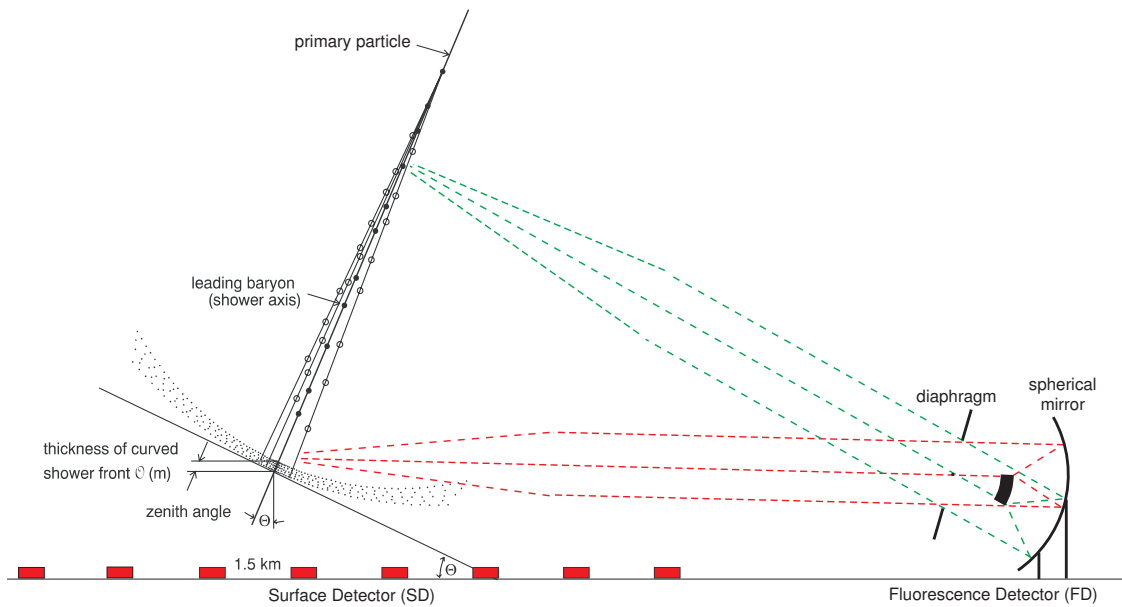


Fig. 1.6: Schematic sketch of the different detection techniques of EAS by means of the surface detector or with the fluorescence telescopes.

nature of the primary cosmic particles, the mechanism of the cosmic accelerators and their location are completely unknown. The combined measurement of the flux, the composition as well as the arrival directions of the ultra-high energy cosmic rays provides a possibility to answer some of these questions. The question about the existence of the GZK-cutoff in the cosmic ray energy spectrum provides a first hint about the origin of the ultra-high energy cosmic rays and the nature of the sources. If there is no GZK-cutoff in the spectrum, either the GZK effect itself may not be applicable to such high energetic particles (e.g. violation of Lorentz invariance) or the cosmic ray particles must originate either from close by sources (bottom up scenarios) or emerge from the decay of heavy exotic particles (top down scenario). Since the cosmic ray particles at ultra-high energies are expected to be less deflected by the galactic and extragalactic magnetic fields, they are assumed to point back to their point of origin. Therefore the distribution of the arrival directions enables to distinguish between different scenarios even to directly identify sources. For instance, the bottom up approach would favour point-like sources which, if located nearby, leads to an anisotropy on small scales in the distribution of the arrival directions. In this case, it may even be possible to perform astronomical observations of the sources in the “cosmic ray light”. On the other hand, some top down scenarios may be identified by a dipole anisotropy of the arrival directions, since the heavy exotic particles, if they exist, are assumed to be clustered in the halo of our Galaxy. All these questions and approaches are strongly related to the propagation mechanism of the ultra-high energy cosmic rays and their deflection at the galactic and extragalactic magnetic fields. Therefore the study of ultra-high energy cosmic rays delivers also new constraints for theoretical propagation models.

Since the particle flux at ultra-high energies is less than 1 particle per km^2 and year, a

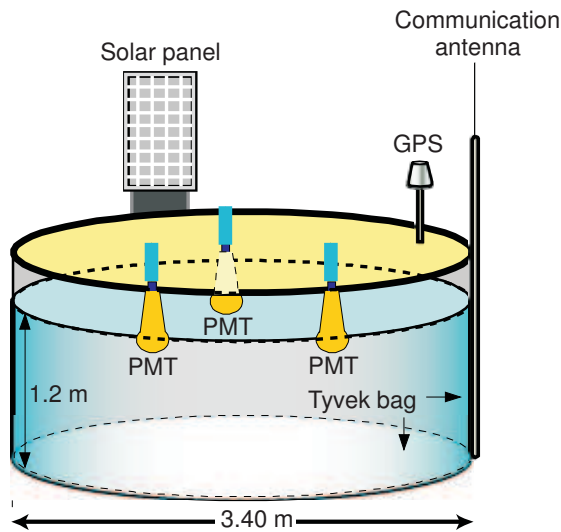


Fig. 1.7: Sketch of a water-Cherenkov detector of the Pierre Auger Observatory.

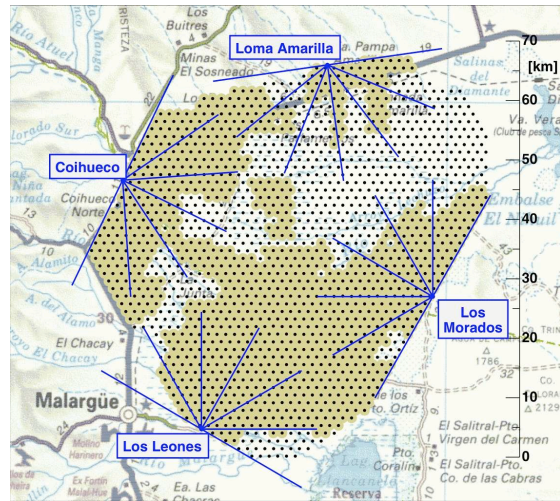


Fig. 1.8: Map of the current status of the surface detector array together with the fluorescence detector stations (eyes).

huge detector size is needed to collect sufficient statistics in a reasonable amount of time. Therefore the Pierre Auger Observatory is situated in the vast Argentinian Pampa Amarilla (yellow prairie) close to the small town Malargue (province Mendoza). The Auger detector is designed as a hybrid detector involving two different and complementary experimental techniques as it can be seen in Fig. 1.6.

At first there is the surface detector array (SD) which is measuring the “footprint” of an EAS at a certain development stage on the ground. It consists of 1600 water-Cherenkov detectors arranged on a triangular grid over a total area of 3000 km^2 . The spacing between the individual detectors amounts to 1.5 km. The detectors measure the Cherenkov emissions of charged particles in the water. The light is detected by three eight-inch photomultipliers (PMT), as shown in Fig. 1.7. The inner part of the tanks is lined with a Tyvek bag to increase the diffuse reflectivity of the walls for the UV-light. Due to the large distances the detectors are controlled and read out by mobile phone technology. Furthermore, they have to be completely self-sustaining concerning the power supply which is achieved by solar panels and batteries. The arrival direction of the EAS can be distinguished by the time differences between the involved surface detectors. The time synchronization of the individual detectors is done by GPS signals. The energy of the primary particle can be estimated by the comparison of the measured particle densities at a certain distance to the shower core to simulations.

The second detector component of the Pierre Auger Observatory is the fluorescence detector (FD). It measures the fluorescence emission of an EAS along the shower axis and therefore is able to observe the whole longitudinal development of the EAS through the atmosphere. The fluorescence detector consists of 24 individual fluorescence telescopes with Schmidt optics arranged in four detector stations (eyes). A single telescope is shown in

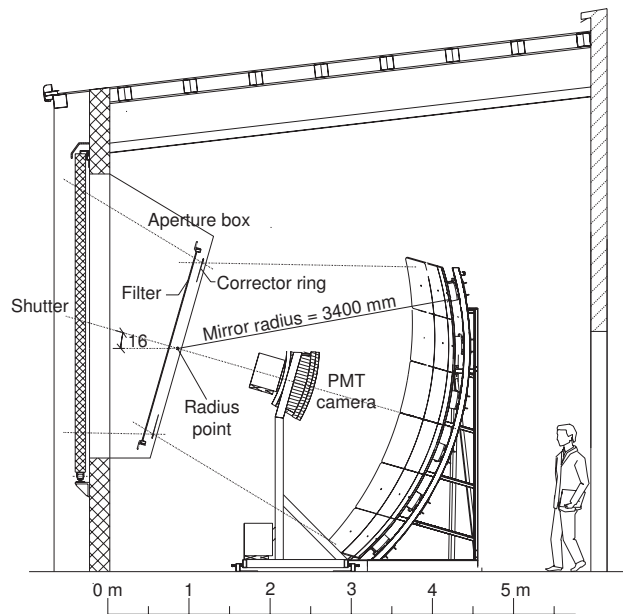


Fig. 1.9: Sketch of a single fluorescence telescope.

Fig. 1.9 and consists of a spherical mirror with a radius of 3400 mm, an aperture box, and the PMT camera with 20×22 PMT pixels. The aperture box contains a diaphragm of 2.2 m diameter, a M-UG6 filter with a transmission region between 300 nm and 410 nm and the corrector ring to correct for spherical aberrations. A single telescope has a field of view of $30^\circ \times 28.6^\circ$ and is inclined by 16° against the horizon. Always six of these telescopes are arranged in the four detector stations, which are situated at the border of the surface detector array, observing the atmosphere above, as is shown in Fig. 1.8. Thus the total field of view of a single eye amounts to $180^\circ \times 28.6^\circ$.

The intensity of the fluorescence light is assumed to be a direct measure of the deposited energy in the atmosphere, from which the primary energy can be reconstructed. Since the fluorescence detector can only be operated in clear, moon-less nights, the duty cycle is 8 to 10 times smaller than that of the surface detector which is always working. On the other hand, the energy determination of the fluorescence detector is much more direct and is therefore used to cross-calibrate the energy determination of the surface detector. The next section will give a closer look on the energy determination by means of the fluorescence detection in order to motivate the experimental studies of this work.

1.4 Fluorescence Detection of Extensive Air Showers

The fluorescence detection of extensive air showers uses the Earth's atmosphere as a scintillator. The secondary particles of an EAS (mostly electrons and positrons) ionize or excite the nitrogen molecules in the air, which subsequently relax to their ground state partially by the isotropic emission of fluorescence photons. Most of the light is emitted in a wavelength range

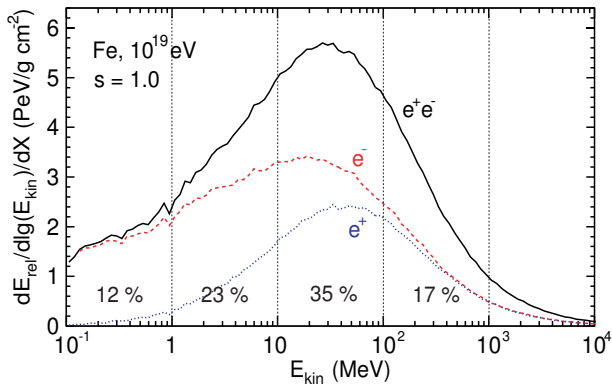


Fig. 1.10: Simulation of the total contribution to the energy release per gram of traversed matter [40].

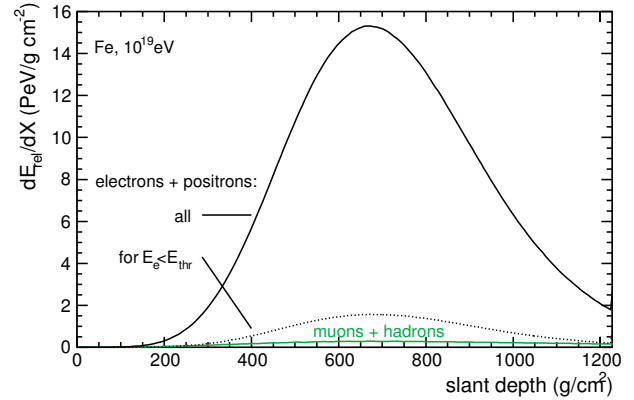


Fig. 1.11: Simulated energy deposit profile of an EAS [40].

between 300 nm and 400 nm. The maximum amount of energy, which in principle could be transferred into fluorescence photons, is given by the energy deposited in the atmosphere. Simulation studies [40] have shown that most of the energy released to the atmosphere arises from electrons and positrons with energies below 1 GeV with a maximum at about 30 MeV, as is shown in Fig. 1.10. From theoretical considerations it is expected that the number of emitted fluorescence photons is proportional to the energy deposit in the atmosphere, as it is shown in Fig. 1.11. First measurements indicate that this proportionality holds within the energy range above ~ 800 keV.

The number of fluorescence photons dN_γ per traversed matter dX , which are detected in the fluorescence detector, can be generally calculated according to

$$\frac{dN_\gamma}{dX} = \int \frac{d^2 N_\gamma^0}{dX d\lambda} \cdot T_{atm}(\lambda, X) \cdot \varepsilon_{FD}(\lambda) d\lambda, \quad (1.13)$$

where ε_{FD} and T_{atm} are the total efficiencies of the fluorescence detector and the transmission of the atmosphere. The atmospheric transmission includes all transmission losses due to optical absorption, Rayleigh- and Mie-scattering from the place of emission until the photons reach the diaphragm of the fluorescence detector. The number of emitted fluorescence photons dN_γ^0 per wavelength interval $d\lambda$ and traversed matter dX can always be written as

$$\frac{d^2 N_\gamma^0}{dX d\lambda} = \int Y(\lambda, T, p, E_{kin}) \cdot \frac{dN_e(X)}{dE_{kin}} \cdot \frac{dE_{dep}}{dX} dE_{kin} \quad (1.14)$$

In this expression, $\frac{dN_e(X)}{dE_{kin}}$ denotes the energy distribution of the secondary electrons or positrons at the atmospheric depths X and $\frac{dE_{dep}}{dX}$ describes the deposited energy per traversed matter dX . The quantity $Y(\lambda, T, p, E_{kin})$ is the so-called “fluorescence yield” in units of photons per deposited energy. It depends on the wavelength λ , the temperature T , the pressure p and in principle even of the energy E_{kin} of the ionizing particles. Assuming the

fluorescence yield to be independent of the energy, it can be moved out of the integral and equation (1.14) transforms to

$$\frac{d^2 N_\gamma^0}{dX d\lambda} = Y(\lambda, T, p) \cdot \frac{dE_{dep}^{tot}}{dX} \quad , \quad (1.15)$$

where dE_{dep}^{tot}/dX is the remaining integral from equation (1.14) corresponding to the total deposited energy in the material layer dX . If this approach is inserted into equation (1.13), the number of detected fluorescence photons becomes proportional to the totally deposited energy per traversed matter:

$$\frac{dN_\gamma}{dX} = \frac{dE_{dep}^{tot}}{dX} \cdot \int Y(\lambda, T, p) \cdot T_{atm}(\lambda, X) \cdot \varepsilon_{FD}(\lambda) d\lambda \quad (1.16)$$

Therefore the number of detected fluorescence photons turns out to be a direct measure of the deposited energy in the atmosphere if the fluorescence yield does not depend on the energy of the ionizing particles. However, up to now this has not yet been totally proven over the relevant energy range as it appears in EAS. Furthermore there are rather large uncertainties about the absolute value of the fluorescence yield. First laboratory measurements in the context of EAS measurements have been made by Bunner [14] in 1967, with an accuracy not better than 30 %. The first cosmic ray experiment using this technique, the Fly's Eye Detector [10], quoted these uncertainties as the dominant systematic error in its measurements. At the end of the nineties, several new cosmic ray detectors employing the fluorescence technique, such as the High Resolution Fly's Eye Detector (HiRes) or the Pierre Auger Observatory, started to take data or began with the construction phase. The statistic of these new detectors is much larger and therefore also the systematic uncertainties of the fluorescence yield need to be reduced in order to exploit the full design capabilities of these detectors. The importance of reducing the systematic uncertainty of the fluorescence yield can also be illustrated by the fact that a 30 % energy shift brings the results of HiRes in Fig. 1.2 into perfect agreement with the AGASA measurements.

First new measurements of the fluorescence yield were made by Kakimoto et al. [27] followed by the measurements of Nagano et al. [34, 35]. In the last years several other groups around the world began working on this topic. The main questions to be answered by these experiments are:

- To which extent is the number of emitted photons proportional to the energy deposit and independent of the energy of the ionizing particles?
- What is the total fluorescence photon yield?
- What is the spectral distribution?
- What is the influence of atmospheric conditions in particular the effect of water vapor and other gases in air?

Chapter 2

Nitrogen Fluorescence in Air

The secondary particles of extensive air showers (EAS), mainly electrons and positrons with energies between 100 keV and 1 GeV [40], are losing their energies through ionization and excitation of the air molecules. Since the nitrogen contribution in air is about 78%, and there are no known strong emission lines [37] of other air constituents in the wavelength range between 300 nm and 400 nm (the Auger filter range), almost all of the air fluorescence emissions in this range originate from transitions of molecular nitrogen N_2 or molecular nitrogen ions N_2^+ [14]. The following sections give a short introduction to molecular spectra and the nomenclature of their energy states. Afterwards, the most important nitrogen band systems for air fluorescence will be presented and finally an expression for the air fluorescence yield will be introduced.

2.1 Molecular Spectra

Molecular spectra are much more complicated than atomic spectra. The different atoms of a molecule are coupled together through ionic or covalent bindings. Thus the atomic base of a molecule has a spatial structure and the nuclei are rotating and vibrating around their center of gravity. These movements of the nuclei itself lead to transitions between their quantized rotational or vibrational states. If such a transition is changing the dipole moment of the molecule, photons can be emitted or absorbed. The spectra of such optical transitions are lying in the far infrared (IR) or microwave regime for rotational transitions and in the infrared region for vibrational transitions. Vibrational spectra always show a rotational substructure, because the change of a vibrational state is accompanied generally by a change in the rotational quantum number. However, diatomic, homo-nuclear molecules such as H_2 , N_2 or O_2 have a cylindrical symmetry and therefore do not have a permanent dipole moment, which can be changed by rotational or vibrational transitions. Such molecules ideally do not show pure rotational or vibrational spectra.

Additionally, molecules also perform electronic transitions between their different electronic states. But in contrast to the relatively simple atomic spectral lines, molecular electronic spectra show a variety of broad bands in the optical and ultra violet (UV) region.

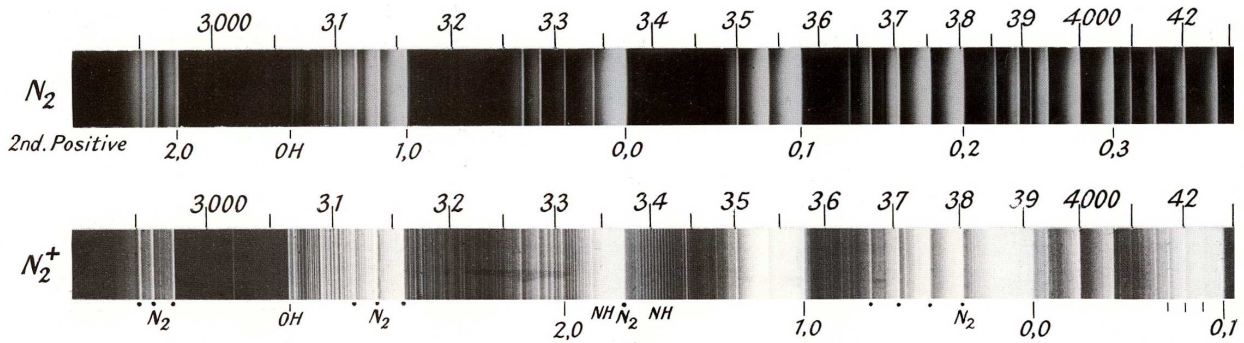


Fig. 2.1: Spectral bands of the second positive (2P) band system of molecular nitrogen N_2 and the first negative (1N) band system of molecular nitrogen ions N_2^+ between 2900 Å and 4300 Å [37].

This is due to the movements of the nuclei, which influence the molecular wave functions of the electrons and change the potential energy of the electronic states. A single electronic transition therefore splits in several vibrational levels and every vibrational level again has a rotational substructure. In other words, the electronic transition determines the absolute position of the band system in the spectrum, the vibrational transitions lead to the different bands of the band system relative to the absolute scale of the electronic transition and finally the rotational transitions are responsible for the fine structure of each band, as can be seen in Fig. 2.1. This implies the energy scales of the three different classes of transitions to be

$$E_{rot} \ll E_{vib} \ll E_{el} \quad . \quad (2.1)$$

The quantum-mechanical calculation of the molecular spectra makes use of the fact, that the mass of the nuclei is much bigger than the mass of the electrons of a molecule. Therefore it is possible to separate the three different contributions to the molecular states Ψ in the following way:

$$\Psi = \psi_{el} \cdot \psi_{vib} \cdot \psi_{rot} \quad (2.2)$$

$$E = E_{el} + E_{vib} + E_{rot} \quad . \quad (2.3)$$

This is the so called Born-Oppenheimer approximation. A semi-classical estimation [9] of the relative orders of magnitude for the three contributions yields:

$$E_{el} : E_{vib} : E_{rot} = 1 : \sqrt{\frac{m}{M}} : \frac{m}{M} \quad (2.4)$$

with the electron mass m and the reduced mass M of the molecular nuclei.

The next three sections will give a short introduction to the three different contributions to the molecular energy states. Since nitrogen is a diatomic homo-nuclear molecule, just this kind of molecular structures will be discussed.

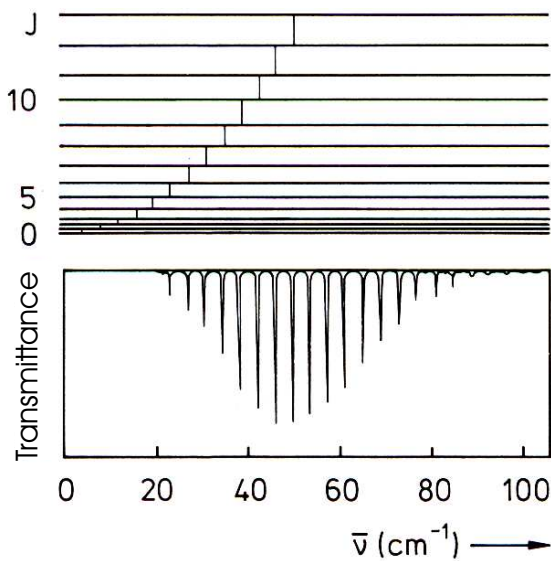


Fig. 2.2: Rotational energy levels of an inelastic rotator [23].

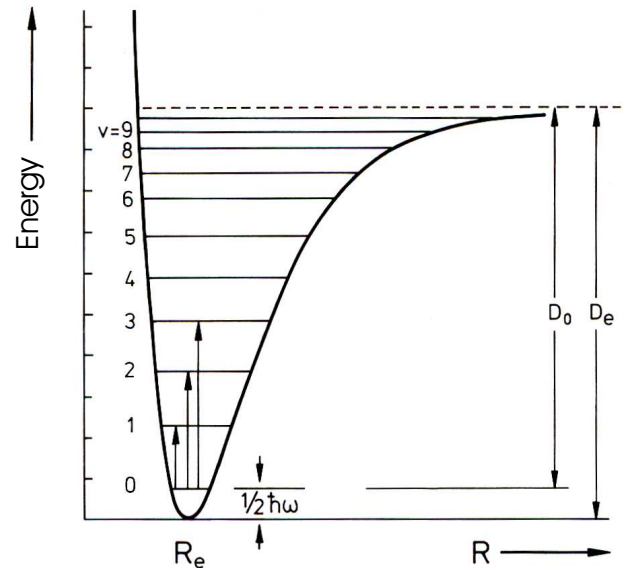


Fig. 2.3: Morse potential and vibrational energy levels of a diatomic molecule [23].

2.1.1 Rotational States of Diatomic Molecules

For the semi-classical calculation of the rotational energy levels of a diatomic molecule just the two nucleons rotating around their center of gravity need to be considered. In case of an inelastic rotator, the classical calculation [23] of the rotational energy leads to

$$E_{rot} = \frac{L^2}{2\theta} \quad (2.5)$$

where L denotes the angular momentum and θ is the moment of inertia around the rotational axis. In case of a diatomic molecule the rotational axis is always perpendicular to the molecular axis. If the angular momentum is substituted by its quantum mechanical expression $|L| = \hbar\sqrt{J(J+1)}$, equation (2.5) reads as

$$E_{rot} = \frac{\hbar^2}{2\theta} \cdot J(J+1) + \dots \quad , \quad J = 0, 1, 2, \dots \quad (2.6)$$

Together with the selection rules for optical transitions ($\Delta J = \pm 1$) these energy levels lead to equidistant lines in the wave number spectrum as is shown in Fig. 2.2. However, for real spectra, the distance between the spectral lines is getting smaller for higher quantum numbers J . This is due to the fact that, in reality, the nucleons are not fixed together but are also vibrating against each other. This changes the moment of inertia θ and therefore higher order correction terms have to be added to equation (2.6). Especially for higher quantum numbers J these corrections are not vanishing.

2.1.2 Vibrational States of Diatomic Molecules

The vibrational movements of the nucleons of a diatomic molecule can be considered in first approximation as harmonic oscillations along the molecular axis. However, this simple assumption is just a reasonable approximation for small oscillation amplitudes ($R - R_e$) around the distance of equilibrium R_e between the nuclei. A better approach to describe the effective binding force between the nuclei is the so called Morse potential shown in Fig. 2.3. Since the molecular binding, and therefore the equilibrium distance R_e , is also determined by the electronic orbitals, the effective potential will be different for different electronic states. The general form of the Morse potential is given by the empirical formula

$$V(R) = D_e [1 - e^{a(R-R_e)}]^2 \quad (2.7)$$

where D_e is the dissociation energy of the molecule. For small oscillation amplitudes ($R - R_e$) this potential simplifies to a simple harmonic potential. In this limit the factor a is determined through $a = \sqrt{\mu/2D_e} \cdot \omega_e$, where μ corresponds to the reduced mass of the nuclei and ω_e is the angular velocity of the harmonic oscillator. The solution of the Schrödinger equation with the Morse potential then yields to

$$E_{vib} = \underbrace{\hbar\omega_e(v + \frac{1}{2})}_{\text{harm. oscillator}} - x_e \hbar\omega_e(v + \frac{1}{2})^2 + \dots, \quad v = 0, 1, 2, \dots \quad (2.8)$$

which corresponds to the energy states of a harmonic oscillator plus higher order correction terms. The first correction term is multiplied with the so-called inharmonicity constant x_e , which typically is of the order 0.01 [23]. Usually, the first order correction already is sufficient for not too large values of v . These correction terms lead to decreasing energy gaps between the energy levels for increasing vibrational quantum numbers v until the energy reaches the dissociation threshold. The optical selection rule for pure vibrational transitions between these states is $\Delta v = \pm 1$, but, because of the inharmonic potential, even transitions between higher harmonic states with $\Delta v = \pm 2, \pm 3, \dots$ are allowed, although with much lower intensities. Since nitrogen is a homo-nuclear diatomic molecule, pure vibrational transitions do not change the molecular dipole-moment and therefore are optically forbidden.

Because the vibrational and the rotational molecular movements are coupled together, a change of the vibrational state is usually accompanied by a change of the rotational state. Therefore the observed vibrational spectral lines are broadened by a rotational substructure, which forms the so-called vibrational bands. In electronic-vibrational-rotational spectra these bands normally show sharp edges versus one side and are shaded versus the other side, as can be seen in Fig. 2.1. The explanation for this effect is given by the so-called P-, Q- and R-branches of the rotational transitions [9, 23]. The direction of shading is connected with the relative orientation of the nuclear Morse potentials of the initial and final electronic states. If a band is shaded versus shorter (violet) wavelength, the equilibrium distance R_e of the initial state is smaller than for the final state and vice versa. However, if R_e is roughly the same for both electronic states, it can happen that the shading changes the direction within the spectrum.

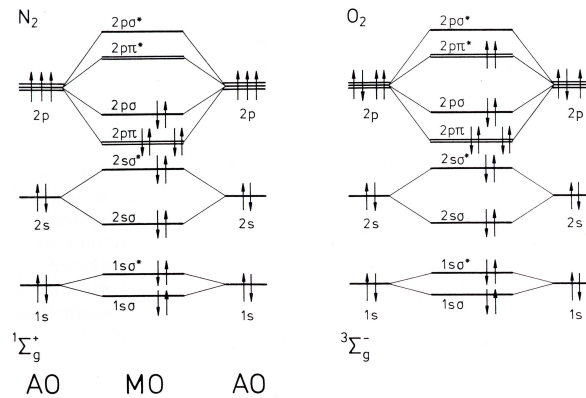


Fig. 2.4: Molecular orbitals of Nitrogen and Oxygen and their population by electrons in the ground state [23].

2.1.3 Electronic States of Diatomic Molecules

The most energetic molecular transitions are transitions between their different electronic states. There are two basic concepts for the solution of the electronic part of the molecular Schrödinger equation, namely the molecular orbital approximation and the Heitler-London approximation. In the molecular orbital approximation the multi-electron wave function is formed as a product of molecular orbitals. A molecular orbital represents a single electron solution of the electronic Schrödinger equation and is derived as a linear combination of the atomic orbitals of the two nuclei (LCAO method). The Heitler-London approximation directly uses a product of atomic orbitals as multi-electron wave function. Both methods do not account for the interaction between the single electrons themselves. Furthermore, the influence of molecular rotations and vibrations is assumed to be negligible, since the electrons follow the nuclear movements nearly instantly due to their small masses with respect to the nuclear masses (adiabatic approximation). It turns out that the molecular orbital approximation is better suited to describe ionic bindings, whereas the Heitler-London approximation yields better results for covalent bindings. More realistic solutions can therefore be obtained by a combination of both kinds of solutions. The following sections give a qualitative description of the resulting molecular orbitals and their quantum numbers.

Molecular Orbitals

Since diatomic molecules have a cylindrical symmetry around the internuclear axis, the effective coulomb field of the two nuclei is also following this symmetry. This forces the electronic angular momentum \mathbf{l} to permanent precessions around the molecular axis with its z-component

$$l_z = m_l \hbar \quad , \quad m_l = -l, -l + 1, \dots, l - 1, l \quad (2.9)$$

in axial direction. The energy of these states does not depend on the orientation of \mathbf{l} but on the absolute value of l_z only. An undisturbed electronic state with angular momentum l

therefore permanently splits into $(l + 1)$ different energy levels, which makes it necessary to introduce a new quantum number λ to characterize the resulting molecular energy states:

$$\lambda = |m_l| = 0, 1, 2, \dots, l \quad (2.10)$$

Similar to atomic orbitals, molecular orbitals with quantum numbers $\lambda = 0, 1, 2, \dots$ are identified with greek letters $\sigma, \pi, \delta, \dots$ and, because of the two directions of precession ($m_l = \pm\lambda$), all of the orbitals, beside the σ -orbitals, show a twofold degeneration. Taking into account also the two spin directions of the electrons, σ -orbitals can be occupied by two, all other orbitals by four electrons.

The linear combination of atomic orbitals leads to symmetric and antisymmetric solutions of the molecular Schrödinger equation. The parity of the resulting molecular wave functions is characterized by a “g”¹ for symmetric, or a “u”² for asymmetric functions in the subscript of the angular momentum symbol like i.e. σ_g, π_u . Depending on the nature of the atomic orbitals, these two solutions are representing either binding or anti-binding molecular orbitals. Anti-binding orbitals are additionally signed with a “*” in the superscript of the angular momentum symbol as for instance σ^* .

To distinguish between molecular orbitals with same quantum numbers λ , the main quantum number n and the symbols (s, p, d, ...) for the angular momentum of the original atomic orbitals are written in front of the symbol for the molecular orbital, following the notation $n l \lambda$. The electron configuration of the molecular ground state, similar to atoms, can be obtained by ordering the molecular orbitals by energy and filling the orbitals using Hund’s rule and the Pauli principle. Thus the electron configuration of the nitrogen molecule N_2 in the ground state turns out to be:

$$(1s\sigma_g)^2(1s\sigma_u^*)^2(2s\sigma_g)^2(2s\sigma_u^*)^2(2p\sigma_g)^2(2p\pi_u)^4$$

The electron population of the molecular orbitals of N_2 in the ground state and their origin from atomic orbitals is illustrated in Figure 2.4.

Molecular States

To describe the complete electronic state of a diatomic molecule, the coupling between the single electrons has to be taken into account. Since the coupling between the single angular momenta \mathbf{l}_i of each electron i is much smaller than their coupling to the axial field of the nuclei, the angular momenta \mathbf{l}_i are precessing nearly independently around the molecular axis. Thus the z-component L_z of the total angular momentum results to be

$$L_z = \sum_i l_z^i = \hbar \sum_i m_l^i \quad (2.11)$$

with the magnetic quantum number m_l^i of the i -th electron. Just the very outer electrons, the so called valence electrons, contribute to L_z , since the contributions of completely filled

¹g: gerade (even)

²u: ungerade (odd)

inner shells are cancelling out each other. Equation (2.11) can be rewritten in the following form:

$$L_z = \pm \Lambda \hbar \quad (2.12)$$

with the quantum number $\Lambda = |\sum_i m_l^i|$. Depending on the sign of the m_l^i one can obtain different values Λ for the same electron configuration. Similar to atomic multi-electron states, molecular states with $\Lambda = 0, 1, 2, \dots$ are labeled with upper case Greek letters $\Sigma, \Pi, \Delta, \dots$ and because of the two possible precession directions of the \mathbf{l}_i around the molecular axis, all of the molecular states with $\Lambda > 0$ show a twofold degeneration.

In contrast to the angular momenta, the spins \mathbf{s}_i of the single electrons are not affected much by the electric field of the atomic nuclei. Instead, they are adding up to a total spin vector $\mathbf{S} = \sum_i \mathbf{s}_i$, which is again precessing around the molecular axis. The precession of \mathbf{S} is caused by its coupling to the magnetic field along the molecular axis, which is induced for $\Lambda > 0$ by the movements of the electrons (LS-coupling). The z-component of the total spin therefore can have the values

$$S_z = \hbar \Sigma \quad , \quad \Sigma = -S, -S + 1, \dots, S - 1, S \quad (2.13)$$

with S and Σ the quantum numbers of total spin and its z-component respectively. The coupling between the total spin and the angular momentum leads to a splitting up of the energy levels for each value of Λ . The multiplicity of the splitting is given as $(2S + 1)$, which is the number of possible S_z values for a given S .

The last sections gave an overview over the meaning of the most important molecular quantum numbers. The spectroscopic classification of the molecular states follows the notation:

$${}^{2S+1}\Lambda_{g,u}^{\pm} \quad . \quad (2.14)$$

The multiplicity $(2S + 1)$ of the molecular state is written in the upper left corner of the symbol for the total z-component Λ of the angular momenta. If the molecular state is symmetric against the mirroring at any plain through the molecular axis, it is marked with a “+” in the upper right corner, otherwise with a “-”. The parity is labeled with a “g” or a “u” in the lower right corner of the angular momentum symbol. The parity of a multi-electron state of a homo-nuclear molecule is called “even” (g) or “odd” (u), if its electron configuration contains an even or odd number of electrons in molecular orbitals with odd parity.

2.1.4 Molecular Transitions and the Franck-Condon-Principle

Transitions between the different molecular states play the key role for the understanding of molecular spectra. Molecules get excited by the absorption of energy by means of optical absorption or energy transfer by other particles. An excited state will in general relax to lower energetic states after a typical time scale depending on the de-excitation process. The following table and the so-called Jablonski-Diagram in Fig. 2.5 give an overview over the most important molecular transitions and their characteristic time constants:

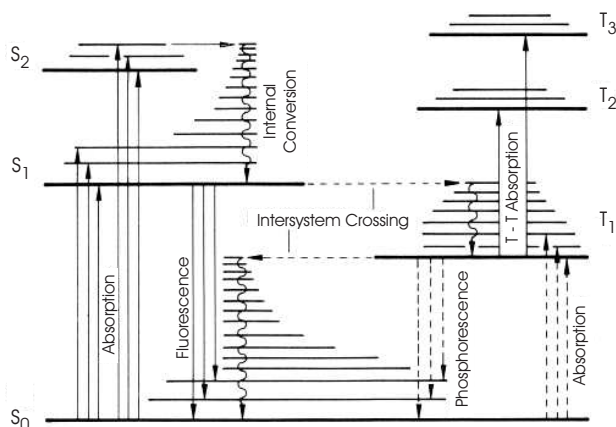


Fig. 2.5: Jablonski-Diagram with the most important radiative and radiationless processes between singlet (S) and triplet (T) states [23].

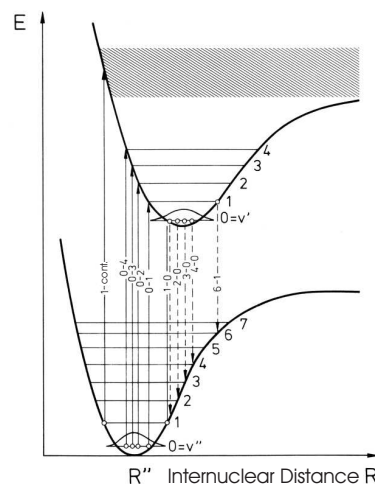


Fig. 2.6: Absorption and emission probabilities between two electronic-vibrational states with the Franck-Condon-Principle [23].

Process	Time [s]
Excitation (Absorption)	10^{-15}
Fluorescence	$10^{-9} - 10^{-7}$
Phosphorescence	$10^{-3} - 10^{+2}$
Internal Conversion	$10^{-14} - 10^{-11}$
Intersystem Crossing	-

Fluorescence denotes optical transitions between the vibrational levels of two electronic states. Also the phosphorescence leads to the emission of optical photons, but, compared to the fluorescence, the time constants are much larger. This is due to the fact that phosphorescence transitions occur from an electronic triplet state with spin quantum number $S = 1$ to a singlet state with $S = 0$, which is optically forbidden. Nevertheless, there is a small probability for such transitions due to the spin-orbit-coupling of the electrons [23], resulting in the observed long lifetimes. Radiationless transitions between singlet and triplet states are called intersystem crossing, whereas internal conversion denotes radiationless transitions between the vibrational levels of an electronic state. Radiationless transitions release their energy to other molecules in terms of rotations, vibrations or translations.

For the quantitative calculation of the transition probabilities of electronic-vibrational transitions, the very illustrative Franck-Condon-Principle plays an important role. As has already been mentioned, a change of the electronic state also influences the binding force between the two nucleons and therefore the internuclear distance in general will also be changed. This is illustrated in Fig. 2.6, where the nuclear Morse potentials for two different electronic states are sketched. For vibrational quantum numbers $v > 0$ the most probable internuclear

distance will be near the region, where the potential curve crosses the horizontal lines of the vibrational energy levels. For $v = 0$ the most probable distance will be the equilibrium position R_e of the electronic state. The Franck-Condon-Principle states that a transition between two electronic states occurs faster than the change of the internuclear distance. Therefore transitions are preferred, where the internuclear distances of initial and final electronic state are the same. This means that the transitions in Fig. 2.6 occur along vertical lines between the most probable nuclear distances of the two electronic states. In quantum mechanical notation this principle leads to the so-called R-Centroid-approximation for the calculation of the transition matrix elements. By means of the Born-Oppenheimer approximation, the matrix elements of the total transition moment between the initial molecular state $|\Psi'(\mathbf{r}, R)\rangle$ and the final state $\langle\Psi''(\mathbf{r}, R)|$, can be written as:

$$\langle\Psi''(\mathbf{r}, R)|\mathcal{M}(\mathbf{r})|\Psi'(\mathbf{r}, R)\rangle = \langle\chi''(R)\psi''(\mathbf{r}, R)|\mathcal{M}(\mathbf{r})|\psi'(\mathbf{r}, R)\chi'(R)\rangle \quad (2.15)$$

where $\psi(\mathbf{r}, R)$ and $\chi(R)$ denote the electronic and nuclear wave functions with electronic coordinates \mathbf{r} and the internuclear distance R . According to the Franck-Condon-principle, this expression can be separated for the electronic and vibrational parts, if the electronic wave functions are taken at the internuclear distance $R = R_{v',v''}$, where the product of the nuclear wave functions maximizes [9, 23]. The mathematical legitimation for this procedure is given by the R-Centroid-approximation [15, 20], which is an expansion of the pure electronic transition moment in a power series of R . The internuclear distance $R_{v',v''}$ for the transition $v' \leftrightarrow v''$ is the r-centroid of first order and corresponds to:

$$R_{v',v''} = \frac{\langle\chi''(R)|R|\chi'(R)\rangle}{\langle\chi''(R)|\chi'(R)\rangle} \quad (2.16)$$

With this approximation the total transition moment separates as follows:

$$\langle\Psi''(\mathbf{r}, R)|\mathcal{M}(\mathbf{r})|\Psi'(\mathbf{r}, R)\rangle \approx \langle\psi''(\mathbf{r}, R_{v',v''})|\mathcal{M}(\mathbf{r})|\psi'(\mathbf{r}, R_{v',v''})\rangle \cdot \langle\chi''(R)|\chi'(R)\rangle \quad (2.17)$$

The first part of this expression corresponds to the electronic transition moment at internuclear distance $R_{v',v''}$, whereas the second part is the overlap integral of the nuclear wave functions between the initial and final vibrational states. The square of this integral yields the so-called Franck-Condon-factor

$$q_{v',v''} = |\langle\chi''(R)|\chi'(R)\rangle|^2 \quad (2.18)$$

Therefore there are no strict selection rules for vibrational transitions within an electronic transition. The vibrational transition probability is just determined by the Franck-Condon-factors. Since the total transition probability or the Einstein-coefficient $A_{v',v''}$ is proportional to the square of the total transition moment, it follows that

$$A_{v',v''} \propto q_{v',v''} \cdot |\langle\psi''(\mathbf{r}, R_{v',v''})|\mathcal{M}(\mathbf{r})|\psi'(\mathbf{r}, R_{v',v''})\rangle|^2 \quad (2.19)$$

This expression corresponds to the total band strength of the electronic-vibrational transition, where the rotational sub-structure is not resolved. To obtain the transition probability

for a single electronic-vibrational-rotational transition, equation (2.19) has to be multiplied with a rotational weighting factor (Hönl-London-factor) similar to the Franck-Condon-factor [9]. A detailed list of Franck-Condon-factors and transition probabilities for spontaneous optical transition of many nitrogen and oxygen band systems can be found in [20].

Selection rules

A molecular transitions is allowed, if the corresponding transition matrix element is not vanishing ($\langle \Psi'' | \mathcal{M} | \Psi' \rangle \neq 0$). From this requirement selection rules can be derived [9]. The following selection rules for optical transitions are valid for homo-nuclear molecules, if the influence of spin-orbit-coupling is neglected:

- Angular momentum quantum numbers: $\Delta\Lambda = \Lambda' - \Lambda'' = 0, \pm 1$
- For Σ states ($\Lambda = 0$): $\Sigma^+ \leftrightarrow \Sigma^+$, $\Sigma^- \leftrightarrow \Sigma^-$
(Only transitions between Σ -states of same symmetry are allowed)
- Total Spin: $\Delta S = 0$
(Intersystem crossing is forbidden if spin-orbit-coupling is neglected)
- Rotational quantum numbers: $\Delta J = \begin{cases} \pm 1 & , \Lambda' = \Lambda'' = 0 \\ 0, \pm 1 & , \text{ otherwise} \end{cases}$
- Laport's rule: $g \leftrightarrow u$
(Only transitions between even and odd electronic states are allowed)

For vibrational transitions within an electronic transition there are no explicit selection rules. Instead, the probability for a vibrational transition is given by the Franck-Condon-factor (2.18), as was already mentioned earlier. If spin-orbit-coupling is taken into account, there are some deviations of these rules. Nevertheless, the transition probabilities for such transitions in general will be rather small, wherefore the most intensive transitions will occur according to the rules from above.

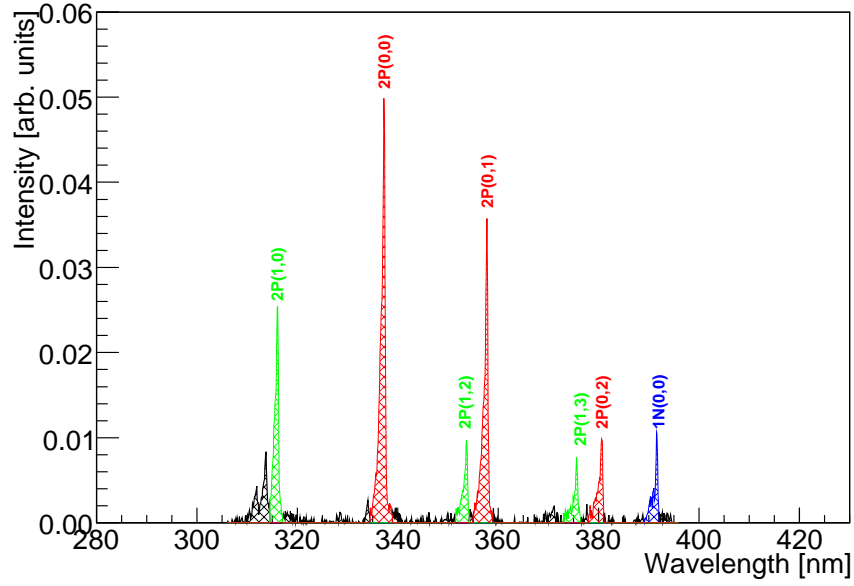


Fig. 2.7: Part of the nitrogen fluorescence spectrum in dry air at 1013 hPa. Measured by Ulrich et al. [44]

λ [nm]	System	v'	v''	$A_{v',v''}$ [s^{-1}]	λ [nm]	System	v'	v''	$A_{v',v''}$ [s^{-1}]
427.81	1N	0	1	$3.71 \times 10^{+6}$	*357.69	2P	0	1	$8.84 \times 10^{+6}$
423.65	1N	1	2	$4.28 \times 10^{+6}$	356.39	1N	2	1	$7.88 \times 10^{+6}$
420.05	2P	2	6	$1.57 \times 10^{+6}$	354.89	1N	3	2	$8.09 \times 10^{+6}$
419.91	1N	2	3	$3.47 \times 10^{+6}$	353.83	1N	4	3	$7.46 \times 10^{+6}$
416.68	1N	3	4	$2.32 \times 10^{+6}$	353.67	2P	1	2	$5.54 \times 10^{+6}$
414.18	2P	3	7	$2.01 \times 10^{+6}$	353.26	1N	5	4	$6.63 \times 10^{+6}$
409.48	2P	4	8	$2.09 \times 10^{+6}$	350.05	2P	2	3	$1.71 \times 10^{+6}$
405.94	2P	0	3	$1.10 \times 10^{+6}$	346.90	2P	3	4	$1.15 \times 10^{+5}$
399.84	2P	1	4	$2.43 \times 10^{+6}$	344.60	2P	4	5	$1.24 \times 10^{+5}$
394.30	2P	2	5	$3.14 \times 10^{+6}$	*337.13	2P	0	0	$1.31 \times 10^{+7}$
*391.44	1N	0	0	$1.14 \times 10^{+7}$	333.90	2P	1	1	$5.87 \times 10^{+5}$
389.46	2P	3	6	$3.00 \times 10^{+6}$	330.90	2P	2	2	$7.99 \times 10^{+5}$
388.43	1N	1	1	$4.03 \times 10^{+6}$	330.80	1N	2	0	$9.02 \times 10^{+5}$
385.79	1N	2	2	$9.27 \times 10^{+5}$	329.87	1N	3	1	$2.08 \times 10^{+6}$
385.79	2P	4	7	$2.33 \times 10^{+6}$	329.34	1N	4	2	$3.19 \times 10^{+6}$
*380.49	2P	0	2	$3.56 \times 10^{+6}$	328.53	2P	3	3	$2.85 \times 10^{+6}$
*375.54	2P	1	3	$4.93 \times 10^{+6}$	326.81	2P	4	4	$3.71 \times 10^{+6}$
371.05	2P	2	4	$4.04 \times 10^{+6}$	*315.93	2P	1	0	$1.19 \times 10^{+7}$
367.19	2P	3	5	$2.35 \times 10^{+6}$	*313.60	2P	2	1	$1.01 \times 10^{+7}$
364.17	2P	4	6	$9.98 \times 10^{+5}$	*311.67	2P	3	2	$5.94 \times 10^{+6}$
*358.21	1N	1	0	$5.76 \times 10^{+6}$	310.40	2P	4	3	$3.02 \times 10^{+6}$

Table 2.1: Nitrogen band heads [37] and transition probabilities $A_{v',v''}$ [20] of the 2P and 1N system between 300 nm and 430 nm. Most intensive bands are labeled with an *.

2.2 The Spectrum of Molecular Nitrogen

The nitrogen fluorescence spectrum between 300 nm and 420 nm mainly consists of transitions from the so-called second positive system (2P) of molecular nitrogen N_2 and the first negative system (1N) of ionized nitrogen molecules N_2^+ [14, 37].

$$\begin{aligned} 2P(v', v'') : & \quad C^3\Pi_u(v') \rightarrow B^3\Pi_g(v'') \\ 1N(v', v'') : & \quad B^2\Sigma_u^+(v') \rightarrow X^2\Sigma_g^+(v'') \quad . \end{aligned} \quad (2.20)$$

The notation “first negative” and “second positive” system indicates the place of emission of the appropriate band system in gas discharge tubes. The positively charged nitrogen molecules are attracted by the negatively charged cathode and therefore the 1N-emissions are emerging from near the cathode. The 2P-emissions of the neutral nitrogen molecules instead are observed closer to the positively charged cathode. The spectral intensity distribution of these two band systems is illustrated in Fig. 2.7. The most important band heads are listed in Table 2.1 together with their calculated transition probabilities from Gilmore et al. [20]. The ratios of the transition probabilities from the same vibrational state v' within a band system correspond to the expected relative intensities of the transition bands. Since vibrational states with $v' > 2$ are hardly observed under normal conditions, many of the listed bands are negligible for further discussion. Thus the most important transitions are labeled with a * in front of the wavelength. Beside the 1N and 2P band systems, there are a lot of other known nitrogen band systems, as is indicated in Fig. 2.8, but they are rather weak or do not contribute to this wavelength range.

2.3 Modelling Nitrogen Fluorescence in Air

In the last few sections the theoretical background for the understanding and the interpretation of homo-nuclear molecular spectra was given. The following section will introduce a model for the description of nitrogen fluorescence in air induced by electrons. Special attention was given to the development of an accurate and consistent model, which is easy to handle and with clear meanings of its different parameters. Therefore some of the “historic” definitions and parameter names may have a different meaning in this work or are substituted by other physical quantities. For example the traditional way of defining the fluorescence yield as photons per meter per electron seems not to be very useful [40]. More natural seems the definition of the fluorescence yield as photons per deposited energy since this quantity corresponds directly to the measured longitudinal shower profiles and does not depend on the momentum direction of the electrons. Furthermore, it can be used directly in simulation codes like CORSIKA³ [24] or GEANT4⁴ [3] where usually optical photon generation is done via energy deposit per material layer or per step length. Therefore the unit of the

³CORSIKA: COsmic Ray SIMulation for KAscade

⁴GEANT: GEometrie ANd Tracking

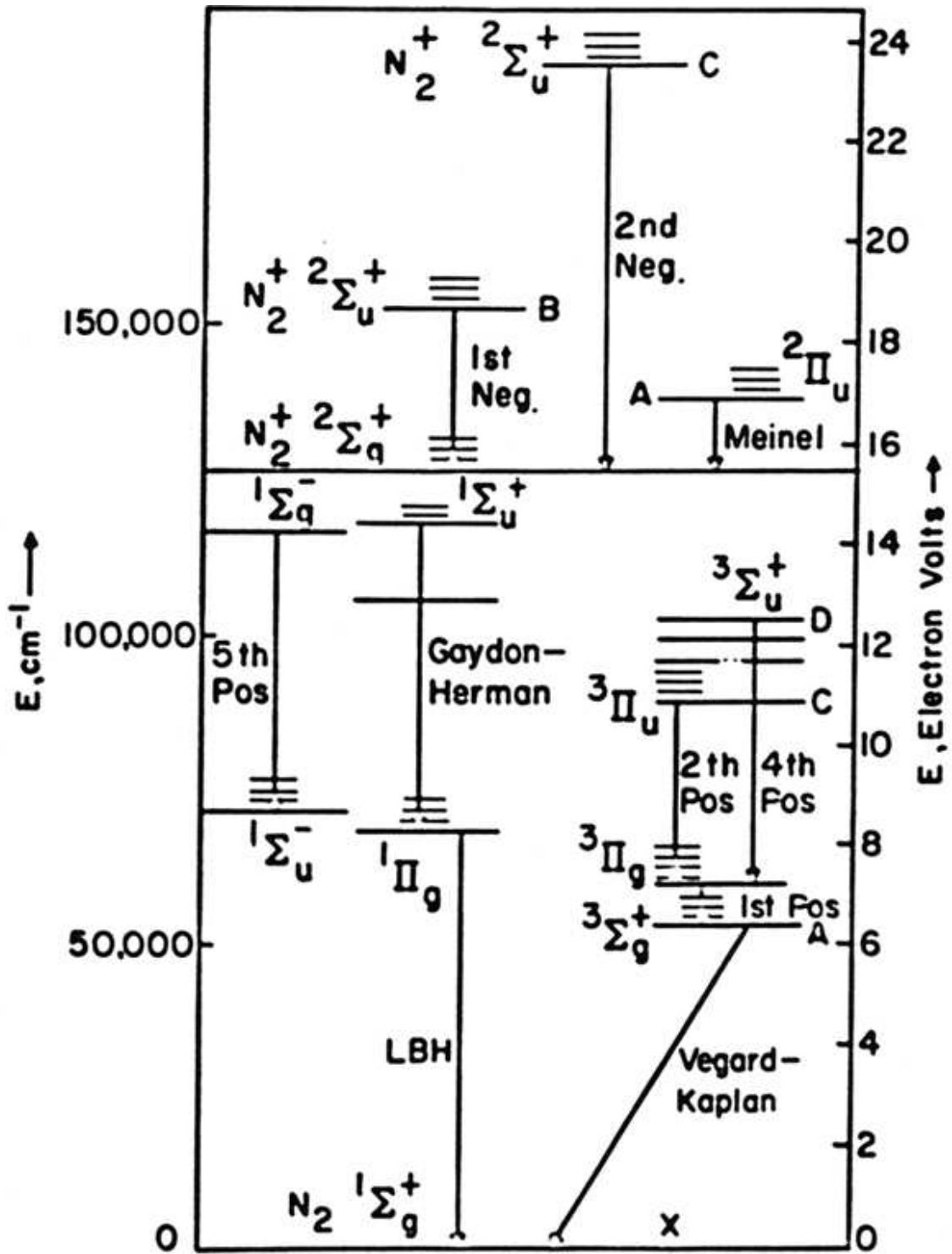


Fig. 2.8: Electronic band systems of molecular nitrogen [14].

fluorescence yield Y in this work is always defined as:

$$[Y(\lambda, p, T)] = \frac{\text{Photons}}{\text{keV}} \quad . \quad (2.21)$$

The old quantity of the fluorescence yield, in units of photons per meter, can be obtained just by multiplying with the Bethe-Bloch function [41] for ionization energy loss:

$$Y_{old}(\lambda, p, T) = Y(\lambda, p, T) \cdot \frac{dE}{dx} \quad . \quad (2.22)$$

The following considerations are based on the general assumption that the fluorescence process can be subdivided into independent processes of excitation and de-excitation of the different electronic-vibrational molecular states. The excitation in general depends on the energy of the excited electrons, whereas the de-excitation depends on the gas conditions such as temperature and pressure. Therefore the following separation ansatz can be made for the fluorescence yield of a single vibrational band:

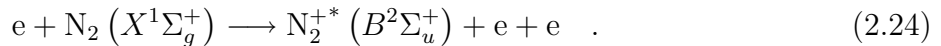
$$Y_{v' \rightarrow v''}(E, p, T) = Y_{v'}^*(E) \cdot \varepsilon_{v' \rightarrow v''}(p, T) \quad , \quad (2.23)$$

where $Y_{v'}^*(E)$ can be identified as excitation yield (number of excited molecules per deposited energy) of a certain electronic vibrational state v' and $\varepsilon_{v' \rightarrow v''}(p, T)$ is the fluorescence efficiency for the emission of an optical photon of wavelength $\lambda(v', v'')$ out of this state.

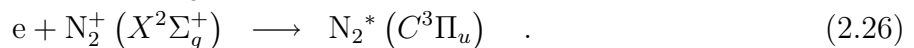
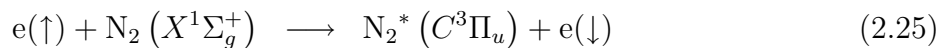
2.3.1 Excitation

As has already been pointed out in section 2.2, nearly all the fluorescence emissions in air between 300 nm and 400 nm are originating from transitions of the 2P and 1N systems of molecular nitrogen N_2 or molecular nitrogen ions N_2^+ . These two systems can get excited by various processes.

The excitation of the $B^2\Sigma_u^+$ initial state of the 1N system is caused by ionization with excitation by high energy electrons (or even other charged particles) according to:



On the other hand, the direct excitation of the $C^3\Pi_u$ initial state of the 2P system from the ground state $X^1\Sigma_g^+$ in general is forbidden, since the molecule would be required to change its spin quantum number. Nevertheless, these states can get excited by low energy electrons via electron exchange [14]. Another possibility is the recombination of molecular nitrogen ions:



Apart from these direct primary processes, there are a lot of secondary processes such as cascading from higher energetic states into the relevant states of the 1N and 2P system,

or their successive excitation by delta electrons released at the ionization of the nitrogen. Therefore it is convenient to summarize all of them into the so-called excitation yield $Y_{v'}^*(E)$. The excitation yield is defined as the number of excited molecules in the electronic-vibrational state v' per deposited energy. It may still depend on the energy E of the electrons, since the underlying excitation cross-sections do so as well. Nevertheless, the energy dependence is expected to be rather weak for energies much larger than the ionization potential of nitrogen, since high energy electrons will release their energy sequentially by various ionization and excitation processes. Furthermore, there might even be a slight pressure and temperature dependence of the excitation yield, if cascading effects (electronic and vibrational) depend on the interaction of the nitrogen with the ambient molecules. Temperature effects on the direct excitation from the ground states are expected to be negligible, since the molecules already at room temperature mainly stay in their vibrational ground state ($v = 0$) and the temperatures in higher altitudes of the atmosphere are much lower.

2.3.2 De-Excitation

A certain initial electronic-vibrational state v' will relax into any lower energetic state v'' after a typical mean decay time $\tau_{v',v''}$ according to the general decay law

$$\frac{dN_{v'}^*}{dt} = -\frac{1}{\tau_{v',v''}} \cdot N_{v'}^*(t) \quad (2.27)$$

if cascading from higher energetic states is neglected or is considered to have much smaller time constants than the mean lifetime of this state. $N_{v'}^*$ denotes the number of excited molecules in the states v' . The reciprocal decay time $\tau_{v',v''}^{-1}$ corresponds to the Einstein coefficient or transition probability $A_{v',v''}$ (see Table 2.1) of the electronic-vibrational transition $v' \rightarrow v''$. If there are more than one final states v'' , the total decay rate becomes:

$$\frac{dN_{v'}^*}{dt} = -\underbrace{\sum_{v''} \frac{1}{\tau_{v',v''}}}_{1/\tau_{v'}} \cdot N_{v'}^*(t) = -\sum_{v''} A_{v',v''} \cdot N_{v'}^*(t) \quad (2.28)$$

Therefore the mean lifetime $\tau_{v'}$ of the excited state v' results to be the inverse of the sum over all transition probabilities $A_{v',v''}$ and the effective observable lifetime of any transition $v' \rightarrow v''$ turns out to be equal to $\tau_{v'}$.

Not all the transitions are necessarily radiative transitions. Some of them transfer their energy into rotations, vibrations or translations of other molecules without emitting optical photons [23]. This so-called quenching effect introduces an additional radiationless deactivation term into equation (2.28), which depends on the pressure and the temperature of the gas. Therefore the inverse lifetime $1/\tau_{v'}$ can be rewritten as

$$\frac{1}{\tau_{v'}(p, T)} = \frac{1}{\tau_{0v'}} + \frac{1}{\tau_{cv'}(T, p)} \quad (2.29)$$

where $1/\tau_{0v'}$ is the sum over all constant transition probabilities and $1/\tau_{cv'}(p, T)$ is the total collisional deactivation rate which depends on the pressure and the temperature of the gas. For isolated molecules at $p \rightarrow 0$ the collision rate becomes zero and therefore $\tau_{v'}(0, 0) = \tau_{0v'}$.

Now, the fluorescence efficiency $\varepsilon_{v' \rightarrow v''}(p, T)$ from equation (2.23) for a certain optical transition can be defined as the ratio of the number of transitions $v' \rightarrow v''$ to the total number of transitions:

$$\varepsilon_{v' \rightarrow v''}(p, T) = \frac{\tau_{v',v''}^{-1} \cdot N^*}{\tau_{v'}^{-1}(p, T) \cdot N^*} = \frac{\tau_{v'}(p, T)}{\tau_{v',v''}} = \tau_{v'}(p, T) \cdot A_{v',v''} \quad (2.30)$$

From this follows that the intensity ratio between two transitions from the same initial state v' into the final states $v'' = a, b$ is constant, since:

$$\frac{\varepsilon_{v' \rightarrow a}(p, T)}{\varepsilon_{v' \rightarrow b}(p, T)} = \frac{A_{v',a}}{A_{v',b}} = \text{const.} \quad (2.31)$$

This means that the fluorescence spectrum can be subdivided into sub-spectra of different initial electronic-vibrational states. The total intensity of the sub spectra is varying differently with pressure and temperature of the gas or the energy of the excited electrons, but the intensity ratios of the transitions within a certain sub-spectrum are always the same. This is an important feature, which will be used for the data analysis later on.

2.3.3 Quenching

Assuming a deactivation cross-section σ for a certain kind of collisional deactivation, it is possible to calculate the corresponding deactivation rate R_c as

$$R_c = n \cdot \sigma(v_{rel}) \cdot v_{rel} \quad (2.32)$$

where n is the number density of the target molecules and v_{rel} is the relative velocity between the target molecule and the excited nitrogen molecule. Therefore in the following v_{rel} and v respectively may not be confused for the vibrational quantum numbers! In a gas of temperature T the molecules are moving according to the Maxwell-Boltzmann distribution of the velocities v :

$$f(\mathbf{v}) = \left(\frac{m}{2\pi kT} \right)^{\frac{3}{2}} \cdot e^{-\frac{m\mathbf{v}^2}{2kT}} \quad \Rightarrow \quad \langle v \rangle = \sqrt{\frac{8kT}{\pi m}} \quad (2.33)$$

The mean velocity $\langle v \rangle$ can be calculated as the Boltzmann-weighted integral over all velocities. The deactivation rate also has to be averaged over all relative velocities $\mathbf{v}_{rel} = \mathbf{v}_2 - \mathbf{v}_1$ and thus:

$$\langle R_c \rangle = n \cdot \int \int \sigma(v_{rel}) \cdot v_{rel} \cdot f_1(\mathbf{v}_1) f_2(\mathbf{v}_2) d^3v_1 d^3v_2 \quad (2.34)$$

In general σ may depend on the velocity of the colliding molecules and therefore on the temperature of the gas. Assuming σ to be constant, it can be moved out of the integral.

Afterwards, the integration can be performed by changing into the center of mass system of the colliding molecules. By doing so, the mean deactivation rate becomes:

$$\langle R_c \rangle = n \cdot \sigma \cdot \sqrt{\frac{8kT}{\pi m_1} \cdot \frac{m_1 + m_2}{m_2}} = n \cdot \sigma \cdot \langle v_1 \rangle \cdot \sqrt{\frac{m_1 + m_2}{m_2}} \quad (2.35)$$

which happens to be $\langle R_c \rangle = \sqrt{2}n\sigma\langle v \rangle$, if the colliding molecules are equal. Equation (2.35) models the deactivation rate for one pair of colliding molecules, e.g for pure nitrogen. Collisional deactivation rates usually are described by the so-called quenching rate constants q_i , in which all gas specific constants are merged together:

$$q_i = \sigma_{Ni} \cdot \sqrt{\frac{8kT}{\pi} \cdot \frac{m_N + m_i}{m_N m_i}} \quad (2.36)$$

In this expression, N stands for the nitrogen molecules and i denotes an arbitrary molecule, which leads to the collisional deactivation of the excited nitrogen. Since air is a mixture of different gases, the total deactivation rate $1/\tau_c$ is the sum over all contributing rates

$$\frac{1}{\tau_c} = \sum_i \langle R_i \rangle = \sum_i n_i q_i = \frac{p}{kT} \sum_i f_i q_i \quad , \quad (2.37)$$

where the concentrations $n_i = \frac{p_i}{kT}$ and the partial pressures are expressed by the proportions f_i to the gas according to $p_i = f_i \cdot p$. The quenching rate constants are no real constants since they still depend on the temperature. Therefore all the quenching rate constants Q_i , which will be quoted in this work, refer to a temperature of 20 °C. The relation to the temperature dependent q_i is given by

$$q_i = \sqrt{\frac{T}{293 \text{ K}}} \cdot Q_i \quad (2.38)$$

With this relation the final expression for the total quenching rate becomes

$$\frac{1}{\tau_c} = \frac{p}{kT} \sqrt{\frac{T}{293 \text{ K}}} \cdot \sum_i f_i Q_i \quad \propto \frac{p}{\sqrt{T}} \quad , \quad (2.39)$$

which is proportional to the pressure and to the inverse square root of the temperature if the collisional cross-sections are assumed to be constant. Since the measurements of the quenching rate constants usually are done at constant temperatures and with constant gas mixing ratios f_i , it is convenient to define a reference pressure $p'_{v'}$ to be the pressure at which the radiative transition rate $1/\tau_{0v'}$ equals the collisional deactivation rate $1/\tau_{cv'}$ and thus:

$$p'_{v'} = \frac{kT}{\tau_{0v'} \cdot \sqrt{\frac{T}{293 \text{ K}}} \cdot \sum_i f_i \cdot Q_{iv'}} \quad (2.40)$$

With this simplification equation (2.29) can be written as:

$$\frac{1}{\tau_{v'}(p, T)} = \frac{1}{\tau_{0v'}} \cdot \left(1 + \frac{p}{p'_{v'}(T)} \right) \quad (2.41)$$

Therefore the reciprocal observable lifetime $1/\tau_{v'}(p, T)$ has a linear dependence on the pressure $p'_{v'}$, if the temperature is constant. This is another useful property for the data analysis.

2.3.4 Total Fluorescence Yield

With the knowledge of the former sections, it now is possible to put everything together to a complete model of the fluorescence yield. For a single transition $v' \rightarrow v''$ between the vibrational states of an electronic band system S , the fluorescence yield can be expressed according to equations (2.23) and (2.30) as:

$$Y_{S(v',v'')}(E, p, T) = Y_{S(v')}^*(E) \cdot A_{S(v',v'')} \cdot \tau_{S(v')}(p, T) \quad (2.42)$$

Therefore the total fluorescence yield of all transitions from a vibrational state v' is the sum over all final vibrational states v'' :

$$Y_{S(v')}(E, p, T) = Y_{S(v')}^*(E) \cdot \tau_{S(v')}(p, T) \sum_{v''} A_{S(v',v'')} \quad (2.43)$$

Unfortunately, it is not possible to measure the radiative transition probabilities $A_{S(v',v'')}$ within this work. But, instead of measuring the absolute numbers, it is possible to measure the relative transition probabilities according to relation (2.31) as the intensity ratios of the different transition bands belonging to the same electronic vibrational state $S(v')$:

$$R_{S(v',v'')} := \frac{A_{S(v',v'')}}{A_{S(v',k)}} = \frac{N_{S(v',v'')}}{N_{S(v',k)}} \quad (2.44)$$

Normally, k is chosen to be the vibrational quantum number v'' of the most intensive transition of the corresponding electronic system S . Therefore in many cases k equals to zero, but in principle every transition $v' \rightarrow k$ can be chosen as reference. With the so defined ratios, the total fluorescence yield can be written as

$$Y_{v'}(E, p, T) = \underbrace{Y_{S(v')}^*(E) \cdot A_{S(v',k)} \cdot \tau_{0S(v')}}_{Y_{S(v',k)}^0(E)} \cdot \frac{\tau_{S(v')}(p, T)}{\tau_{0S(v')}} \cdot \left(1 + \sum_{v'' \neq k} R_{S(v',v'')} \right) \quad (2.45)$$

where $Y_{S(v',k)}^0(E) = Y_{S(v')}^*(E) \cdot A_{S(v',k)} \cdot \tau_{0S(v')}$ is the intrinsic fluorescence yield for the transition $S(v', v'')$ in the absence of collisional quenching. Even this is a measurable quantity and thus the equation above contains only quantities, which can be experimentally measured.

Air Fluorescence Yield

As can be seen in Fig. 2.7, the nitrogen fluorescence spectrum mainly consists of the three contributions 2P(0, v''), 2P(1, v'') and 1N(0,0) from the second positive and first negative system. Therefore it can be modelled as a superposition of three sub-spectra, where each of them has a different quenching behavior. In case of the 1N system, there just exists one important transition 1N(0,0) at 391.4 nm in the wavelength range between 300 nm and 420 nm. Therefore the total fluorescence yield can be expressed as the sum of three

contributions:

$$Y_{tot}(E, p, T) = \left[\sum_{v'=0,1} Y_{2P(v',0)}^0(E) \cdot \frac{\tau_{2P(v')}(p, T)}{\tau_{02P(v')}} \cdot \left(1 + \sum_{v'' \neq 0} R_{2P(v',v'')} \right) \right] + Y_{1N(0,0)}^0(E) \cdot \frac{\tau_{1N(0)}(p, T)}{\tau_{01N(0)}} \quad (2.46)$$

Since natural air consists of 78 % nitrogen, 21 % oxygen, and ~ 1 % argon and a variable amount of water vapor the effective lifetimes of the vibrational state v' within the electronic system $S = 2P, 1N$ calculates according to equations (2.29) and (2.39):

$$\frac{1}{\tau_{S(v')}} = \frac{1}{\tau_{0S(v')}} + \frac{p}{kT} \cdot \sqrt{\frac{T}{293 \text{ K}}} \cdot \left[\left(0.78 \cdot Q_{N_2}^{S(v')} + 0.21 \cdot Q_{O_2}^{S(v')} \right) \cdot \left(1 - \frac{p_{H_2O}}{p} \right) + \frac{p_{H_2O}}{p} \cdot Q_{H_2O}^{S(v')} \right] \quad (2.47)$$

The contribution of argon to the quenching is neglected in this expression, since its amount of about 1 % in air is rather small. The partial pressure p_{H_2O} of the water vapor can be derived from the relative humidity rH and the saturation pressure p_s at a certain temperature by means of the Magnus formula [33]:

$$p_{H_2O} = rH \cdot p_s \quad , \quad p_s = \begin{cases} 6.1078 \text{ hPa} \cdot e^{\frac{17.08085 \cdot T [^\circ C]}{T [^\circ C] + 234.175^\circ C}} & , \quad T > 0 \text{ } ^\circ C \\ 6.1078 \text{ hPa} \cdot e^{\frac{17.84362 \cdot T [^\circ C]}{T [^\circ C] + 245.425^\circ C}} & , \quad T < 0 \text{ } ^\circ C \end{cases} \quad (2.48)$$

Chapter 3

The AirLight Experiment

The AirLight experiment aims for a measurement of the fluorescence yield of electrons in nitrogen and in air within the atmospheric conditions as they appear in extensive air showers. The electrons used in the experiment are emitted from a ^{90}Sr -source with usable energies ranging from 250 keV to 2000 keV. This range covers roughly 12 % of the relevant energies in air showers [40]. The following sections describe the experimental setup and the data acquisition as well as the calibration in more detail.

3.1 Experimental Setup

The basic setup to measure the fluorescence light output of electrons in a gas is rather simple. It can be realized by putting photon detectors around an electron beam. To minimize systematic uncertainties, as few as possible windows, mirrors, or lenses should be used within the light path and, since the fluorescence light is emitted isotropically, the easiest way to achieve this is to put the photon detectors perpendicular around the beam looking directly onto it. The two fundamental parameters of this experimental geometry are:

- Length of the electron beam:
The electron beam length determines the minimum energy of the electrons, which can be used in analysis. Since the experiment is operated in thin target mode, the electrons are assumed to have constant energies along the whole beam length. This condition is roughly satisfied, if the energy loss along the beam is smaller than $\sim 5\%$ of the initial energy. For a desired energy threshold of ~ 500 keV at a pressure of ~ 1000 hPa, this requirement leads to a maximum beam length of 10 cm.
- Radial position of photon detectors:
The radial distance of the photon detectors to the beam axis influences the acceptance of the detectors. To maximize the acceptance, the beam length should fit into the whole field of view of the photon detectors. If the detectors are farther away, the acceptance gets worse. Nevertheless, the detector distance should be large enough to avoid too large incidence angles of the light. Large angles cause higher reflection losses at glass

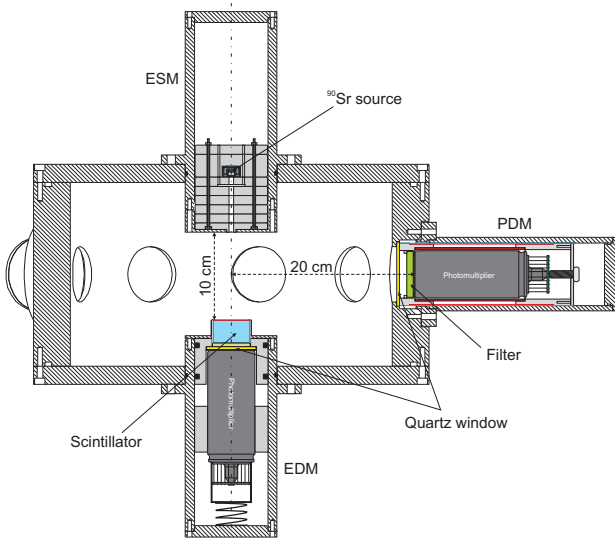


Fig. 3.1: Sketch of the AirLight chamber.

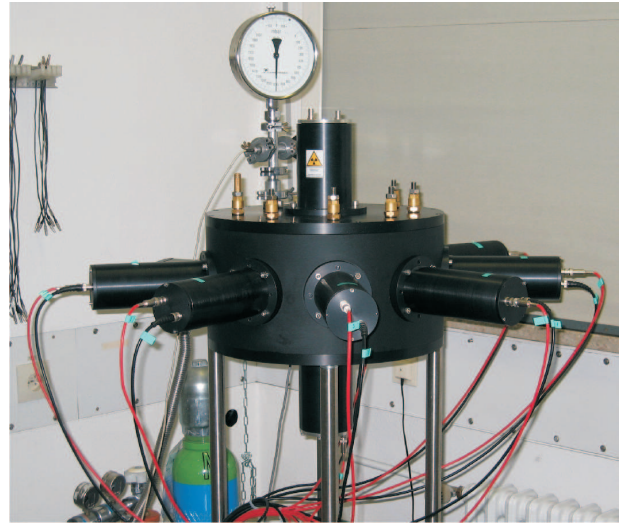


Fig. 3.2: Image of the AirLight chamber.

surfaces and are difficult to treat if interference filters are used. For the setup of the AirLight experiment, a radial distance of 20 cm was chosen for the photon detectors.

Once these two parameters are given, the rest of the experimental design derives from them. For the AirLight chamber, shown in Fig.3.1, a modular setup was chosen. It consists of the chamber body, seven photo detector modules (PDM), an electron detector module (EDM), and an electron source module (ESM). This makes it easy to exchange modules among each other or to substitute a module for another one, e.g. the electron source for a calibration lamp. The whole chamber is made of aluminum (AlMg_3), which is black anodised to prevent photons to scatter back off the chamber walls.

The chamber body has a cylindrical shape of 20 cm inner height and 17.5 cm inner radius. The side wall contains nine identical openings of 7 cm diameter every forty degrees. Seven of them are used to mount the PDMs. These openings are closed with quartz windows and are equipped with shutters at the inner side of the chamber, which can be opened or closed manually via sliding bars. Because the quartz windows are glued from outside into the openings, the chamber is not suited to measure at pressures higher than the ambient pressure. The remaining two openings are used for the connection of the gas system and several sensors to the chamber. In the bottom and in the top of the chamber body there are two CF100 openings of 10 cm diameter centered around the chamber axis. These two openings are needed to mount the ESM and the EDM respectively or to install calibration devices.

In the following sections the properties of the different modules attached to the chamber are discussed in more detail.

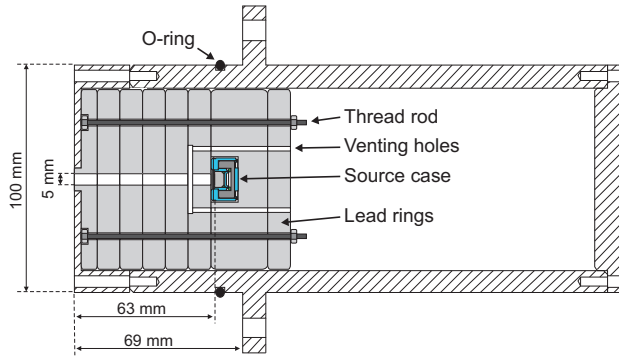


Fig. 3.3: Electron Source Module.

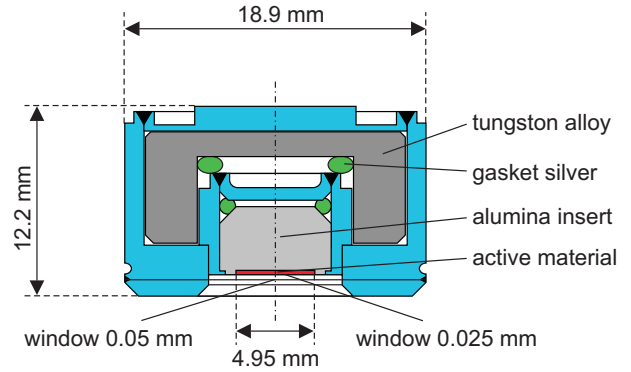
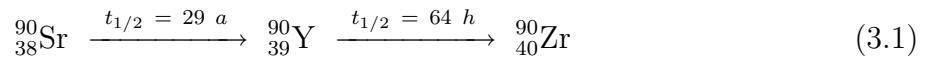


Fig. 3.4: Stainless steel case of the ^{90}Sr source.

3.1.1 Electron Source Module

The electron source is housed in the so-called electron source module (ESM) shown in Fig. 3.3. The source is embedded into a massive lead cylinder with an axial exit pipe of 5 mm width to collimate the electrons. The pipe consists of several lead rings of 1 cm thickness. This way it is easy to adjust the collimator length by just adding or removing some of the rings. The optimal length of the collimating pipe was found to be 6.3 cm.

The real source is a double encapsulated $^{90}\text{Sr}/^{90}\text{Y}$ beta emitter from AEA Technology. The structure of its stainless steel case is shown in Fig. 3.4. The radioactive material is embedded into a ceramic disc of 0.4 mm thickness and 4.95 mm diameter and has a nominal activity of 37 MBq. The total thickness of the two stainless steel exit windows sums up to 75 μm . The electrons emitted by this source are originating from the decay chain



which finally terminates in the stable isotope ${}_{40}^{90}\text{Zr}$ (zirconium). Because the half life of the strontium is much larger than the half life of the yttrium, the source can be considered in equilibrium and a decay of a strontium is “immediately” followed by a decay of its yttrium daughter. Therefore the energy spectrum of the electrons is an equally weighted superposition of the beta spectra of the strontium with an end point energy of 546 keV and of the yttrium with a maximum energy of 2280 keV. Due to the experimental energy threshold of 250 keV, most of the electrons used for the measurements are originating from the yttrium decay. The rates at the electron detector vary between ~ 10 kHz for 1000 hPa and ~ 20 kHz for very low pressures. Even the shape of the electron energy spectra is changing with pressure. The energy spectra are getting harder for higher pressure, since low energetic electrons are scattered away or will be stopped before they can reach the detector. A theoretical description of the primary beta spectrum is given in Section 4.2.

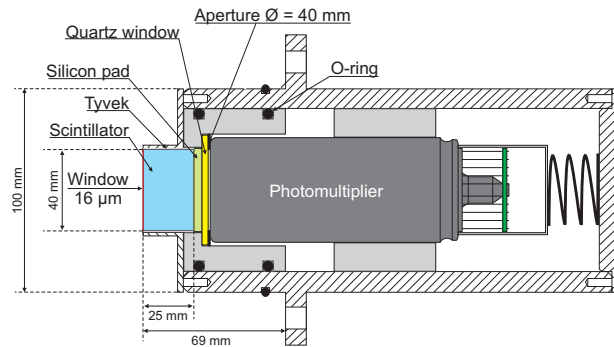


Fig. 3.5: Electron Detector Module

3.1.2 Electron Detector Module

The electron detector module (EDM) shown in Fig. 3.5 mainly consists of a BICRON plastic scintillator (BC-412), which is optically coupled to a photomultiplier (PMT). The scintillator is made of polyvinyltoluene (C_9H_{10}) with a rise time of 1 ns and a typical pulse width of 4.2 ns FWHM. To minimize background due to cosmic or ambient radiation its size was chosen as small as possible. Its cylindrical shape has a diameter of 4 cm and its height amounts to 2.5 cm. Electrons with energies up to 4 MeV will completely be stopped in this volume. The amount of induced scintillation light is proportional to the electron energy deposit in the scintillator and is independent from temperature between -60°C und $+20^{\circ}\text{C}$.

The scintillator is wrapped with several layers of Tyvek around its side to scatter back exiting light into its volume. It is encased by a 0.4 mm thick alumina cap with an entrance window of $16\ \mu\text{m}$ thickness made of polyethylene (PE). This foil has a reflecting surface at its inner side and is black painted at the other side. It was kindly donated by the TRICON GmbH. The scintillator is optically coupled to a quartz window with a 5 mm silicon pad. The quartz window separates the PMT from the inner volume of the chamber to avoid gas discharges at low pressures between the negative high voltage parts and the grounded surroundings. The two inch Photonis PMT XP2262 is the same as the one used for the photon detectors. It is operated at a voltage of 2000 V in pulsed mode. Its spectral characteristics are shown in Fig. 3.7. The typical energy resolution of the electron detector turned out to be about $10\% \cdot \sqrt{E/\text{MeV}}$. The calibration of the electron detector is described in Section 3.5.1.

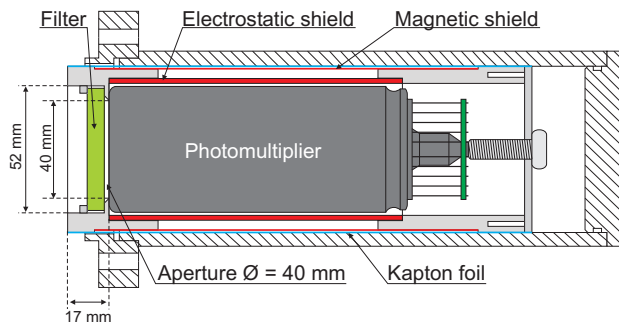


Fig. 3.6: Photon Detector Module.

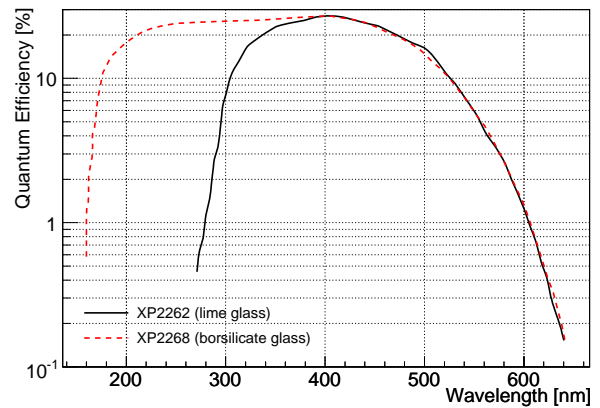


Fig. 3.7: Quantum efficiencies of the Photonis PMTs (Manufacturers values).

3.1.3 Photon Detector Module

The photon detector module (PDM) assembles the filter, the PMT as well as the shielding, as is shown in Fig. 3.6. Two kinds of two inch PMTs are used for the PDMs. For the wavelengths longer than 330 nm, Photonis XP2262 PMTs with a lime glass window and a bi-alkali photocathode are used. For the nitrogen bands around 316 nm a Photonis XP2268 PMT is better suited. The latter has the same inner structure, voltage divider, and photocathode as the XP2262, but, instead of the lime glass, a quartz glass window with an extended sensitivity to shorter wavelengths is used, as can be seen in Fig. 3.7. Both kinds of PMTs are operated in single photon counting mode at a negative high voltage of 2200 V. In negative high voltage mode, the photocathode is put on a negative potential and the electrons inside the PMT are attracted by the grounded anode. Since the whole chamber, including the different modules, is also put on ground potential, the electrons inside the dynode stages of the PMTs happen to be deviated towards the PMT walls and thus induce noise or lead to an unstable behavior of the PMT. To avoid such effects the PMT is surrounded by an electrostatic shield, which screens the PMT from the ground potential of the surroundings. The electrostatic shield consists of a brass tube with an aperture ring made of POM on its front and a PVC end ring on the back side. The brass tube is put on photocathode potential to shield the PMT inside the tube electrostatically from the ground potential on the other side. The brass tube is wrapped with Teflon and an additionally layer of Kapton for insulation. Finally, a sheet of mu-metal is wrapped around everything to provide a magnetic shielding against the geomagnetic field. The aperture ring at the front side limits the sensitive area of the photocathode to a diameter of 4 cm and is used to support the filter. Furthermore, it acts as a spacer to place the photocathode exactly at a distance of 20 cm to the chamber axis.

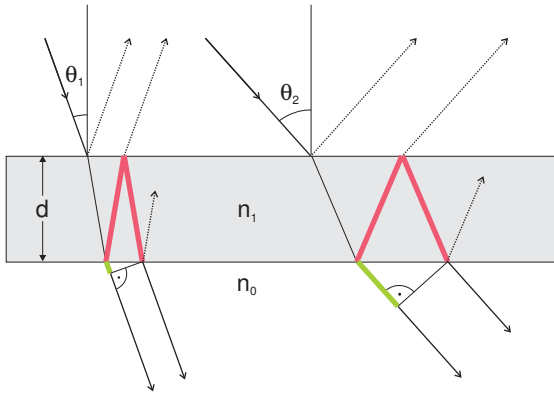


Fig. 3.8: Illustration of working principle of an interference filter. Only light with the right wavelength is able to pass the filter by constructive interference. The rest will be reflected back.

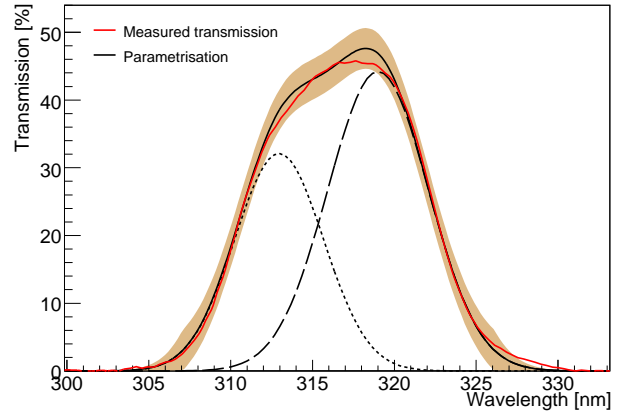


Fig. 3.9: Measured transmission curve of the filter “317a”, at 10° incident angle, superimposed with the corresponding parametrization as a sum of two Gaussian functions.

3.2 Filters

The PDMs are equipped with different filters to measure the light signals only in the desired wavelength region. For the measurements presented in this work one M-UG6 absorption filter and 6 interference filters, matched to the most intensive nitrogen bands, were chosen. The M-UG6 filter from Schott Glas is the same as the one is used in the fluorescence detectors of the Pierre Auger Observatory [2] and transmits the whole fluorescence spectrum between 300 nm and 410 nm.

The interference filters are used to measure single nitrogen transition bands and therefore need to have narrow transmission regions. Typical widths of the transmission bands are of the order of 12 nm FWHM. With normal absorption filters it is not possible to realize such narrow bands. Instead of absorbing the light in the filter material, interference filters are acting like Fabry-Perot interferometers. They consist of several thin layers with different indices of refraction. The light undergoes multiple reflections between the layers, as is illustrated in Fig. 3.8. Only light with the correct wavelength is able to pass the filter by constructive interference. All the rest will be reflected back. Because there always are higher orders of interference passing through the layers as well, the layers usually are superimposed on an absorption filter substrate, which makes a pre- or after-selection of the light.

A disadvantage of interference filters is that they change their transmittance spectrum with the incidence angle of the light, as is shown in Fig. 3.11. The higher the incidence angle the bigger is the shift of the central wavelength towards shorter wavelengths. Furthermore, the maximum transmission mostly is decreasing with larger angles. This happens because the light path between the different interference layers gets longer for larger incident angles, which changes the interference conditions. Therefore large incident angles should be avoided. The angular distribution of the incident photons in the AirLight chamber, shown in Fig. 3.10,

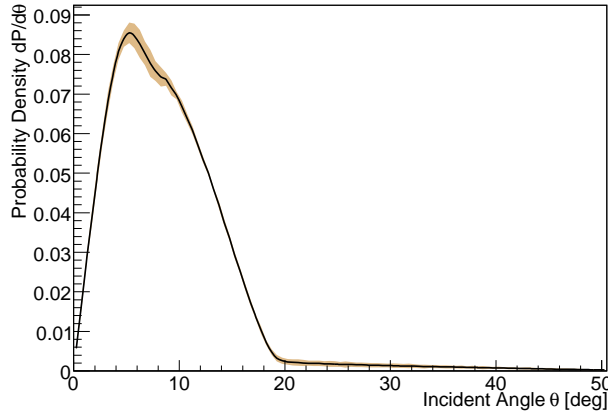


Fig. 3.10: Simulated photon angular distribution averaged over the whole pressure range. The tail above 20° is due to multiple scattering of the electrons.

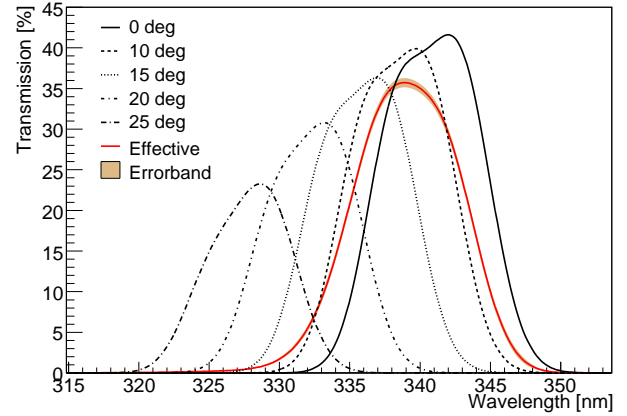


Fig. 3.11: Parametrized transmission curves of the filter “340a” for different incidence angles. The effective transmittance was obtained by averaging over the incident angles from Fig. 3.10.

has been obtained by means of Monte Carlo simulations described in Section 4.4. The error band on the angular distribution in Fig. 3.10 corresponds to the envelope of all angular distributions obtained for different pressures ranging from 20 hPa to 800 hPa. The tail above 20° is due to the multiple scattering of the electrons. However, $\sim 96\%$ of the incident angles always are below 20° .

To counteract the drop of the central wavelength for increasing incidence angles, the interference filters for the AirLight experiment have been chosen with a slightly longer central wavelength than it was desired. Furthermore, a parametrization of the filter transmittance has been developed in the diploma thesis of S. Klepser [29]. The parametrization describes the angular dependence of the interference filters as a superposition of two Gaussian functions, where the amplitudes, widths, and mean values differently depend on the incident angle. In this model, the filter transmittance is expressed by

$$T(\lambda, \theta) = T_1 \cdot e^{-\frac{4 \ln 2 (\lambda - \lambda_1)^2}{b_1^2}} + T_2 \cdot e^{-\frac{4 \ln 2 (\lambda - \lambda_2)^2}{b_2^2}}, \quad (3.2)$$

with the parameters:

$$\lambda_1 = p_1 \cdot \sqrt{1 - \frac{\sin^2 \theta}{p_2^2}} \quad \lambda_2 = p_9 \cdot \sqrt{1 - \frac{\sin^2 \theta}{p_{10}^2}} \quad (3.3)$$

$$b_1 = p_3 \theta^2 + p_4 \theta + p_5 \quad b_2 = p_{11} \theta^2 + p_{12} \theta + p_{13} \quad (3.4)$$

$$T_1 = p_6 \theta^2 + p_7 \theta + p_8 \quad T_2 = p_{14} \theta^2 + p_{15} \theta + p_{16} \quad (3.5)$$

The 16 parameters p_i were obtained through a fit of the model (3.2) to measured transmittance spectra at different incident angles between 0° and 20° degree with a step size of 5° . An example of such a fit is given in Fig. 3.9. The absolute systematic uncertainty of this

Filter Name	317a	340a	360a	380a	394a	430a
p1 [nm]	314.79	338.18	359.77	378.74	392.92	427.60
p2 [1]	1.61	1.54	1.53	1.44	1.75	1.99
p3 [$10^4 \cdot \text{nm}/\text{deg}^2$]	-45.37	-8.63	7.35	-13.06	35.33	0.20
p4 [$10^2 \cdot \text{nm}/\text{deg}$]	5.13	1.37	-0.09	0.69	-2.44	-0.53
p5 [nm]	6.32	4.81	5.81	5.00	5.87	4.16
p6 [$10^2 \cdot \%/ \text{deg}^2$]	-4.93	-3.96	-3.71	-6.83	-2.84	0.53
p7 [$10^1 \cdot \%/ \text{deg}$]	-0.28	2.59	2.71	8.77	-2.51	-3.33
p8 [%]	37.31	29.58	23.07	43.09	34.16	36.32
p9 [nm]	320.95	342.70	365.33	383.25	397.94	431.39
p10 [1]	1.58	1.51	1.50	1.43	1.60	1.98
p11 [$10^4 \cdot \text{nm}/\text{deg}^2$]	1.42	-0.22	-3.71	4.25	-0.91	-11.40
p12 [$10^3 \cdot \text{nm}/\text{deg}$]	3.79	-13.40	-12.40	0.39	-3.48	27.00
p13 [nm]	7.18	5.48	6.83	5.16	5.36	4.88
p14 [$10^2 \cdot \%/ \text{deg}^2$]	-3.87	-3.06	-4.22	-5.07	-8.52	-0.55
p15 [$10^1 \cdot \%/ \text{deg}$]	2.72	0.98	4.02	11.70	4.73	0.97
p16 [%]	45.34	38.14	36.28	39.58	45.86	45.43

Table 3.1: Properties of the filters used for this measurements.

parametrization turned out to be $\Delta T = 3.0 \%$, as is illustrated by the error band in Fig. 3.9. The parameters of each filter used for this work are listed in Table 3.1. Using the angular distribution $\frac{dP}{d\theta}$ from Fig. 3.10, it now is possible to calculate the effective filter transmittance by averaging over the incident angles:

$$T_{eff}(\lambda) = \int \frac{dP}{d\theta} \cdot T(\lambda, \theta) d\theta \quad \rightarrow \quad \sum_i T(\lambda, \theta_i) \cdot P_i \quad (3.6)$$

The integral can be solved in terms of a sum over all angle bins of the angular distribution, where the P_i correspond to the occurrence probability of the angles θ_i . The resulting effective transmission function in the case of the filter “340a” is shown in Fig. 3.11. The error band has been calculated by applying Gaussian error propagation:

$$\Delta T_{eff} = \sqrt{\sum_i (T(\lambda, \theta_i) \cdot \Delta P_i)^2 + (P_i \cdot \Delta T)^2} \quad , \quad \Delta T = 0.03 \quad (3.7)$$

This is possible, since the summation is done over a large range of incidence angles and the true values are assumed to vary around the averaged transmission and angular distribution functions. The effective transmission functions of the other filters have been determined in the same manner and are shown in Fig. 3.13 together with the various nitrogen transition bands, which are the subject of this work.

As has already been mentioned, interference filters reflect the light which is not passing through. This may have negative impact on the calculation of the acceptance of the photon

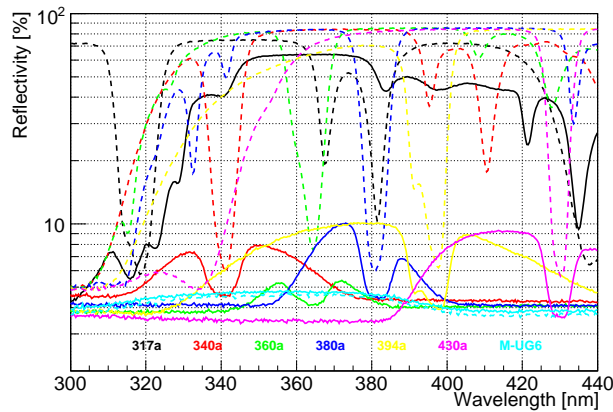


Fig. 3.12: Filter reflectivities at zero degree incidence angle. Less reflecting sides are represented by the solid lines and the dashed lines correspond to the highly reflecting sides.

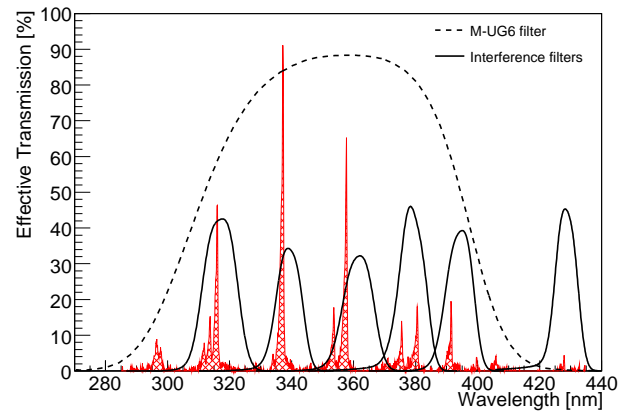


Fig. 3.13: Effective transmission curves of the AirLight filters superimposed with the nitrogen spectrum from [44].

detectors, since the reflected light can be detected by another photon detector. Fortunately, most of the interference filters used in this work are combined with normal absorption filters as carrier material for the interference layers. Therefore they have one highly reflecting side and one much less reflecting side as can be seen in Fig 3.12. The only exception is the filter “317a”, where both sides are highly reflecting. To minimize the backscattering of photons into the chamber, the highly reflecting sides of the filters are turned towards the photocathode of the PMT when installing them into the PDMs. This can be done, since the transmittance of the filters does not depend on their orientation.

3.3 Gas System and Sensors

The gas system shown in Fig. 3.14 is needed to evacuate the chamber and to refill it with different gases. The inner diameter of its supply lines (green lines) amounts to 4 mm and its return lines (red lines) to 16 mm. The larger cross section of the return lines is needed to evacuate the chamber in a shorter time and to benefit from the full power of the vacuum pump. The ventilation intake is useful to vent the whole return line after the chamber has been evacuated. This prevents the oil of the vacuum pump to get sucked inside the return lines, which in the worst case could also contaminate the vacuum chamber. Furthermore, the ventilation intake can be used to equalize the pressure with laboratory air, if the chamber has to be opened.

The Erlenmeyer flask, filled with purified water, allows to add a certain fraction of water vapor to the dry gas, coming out of the gas bottle. To do so, the chamber has to be evacuated completely. Afterwards, the flask has to be evacuated by opening valve n°2 until the water starts to boil. To counteract the cooling down of the water due to evaporation, the flask

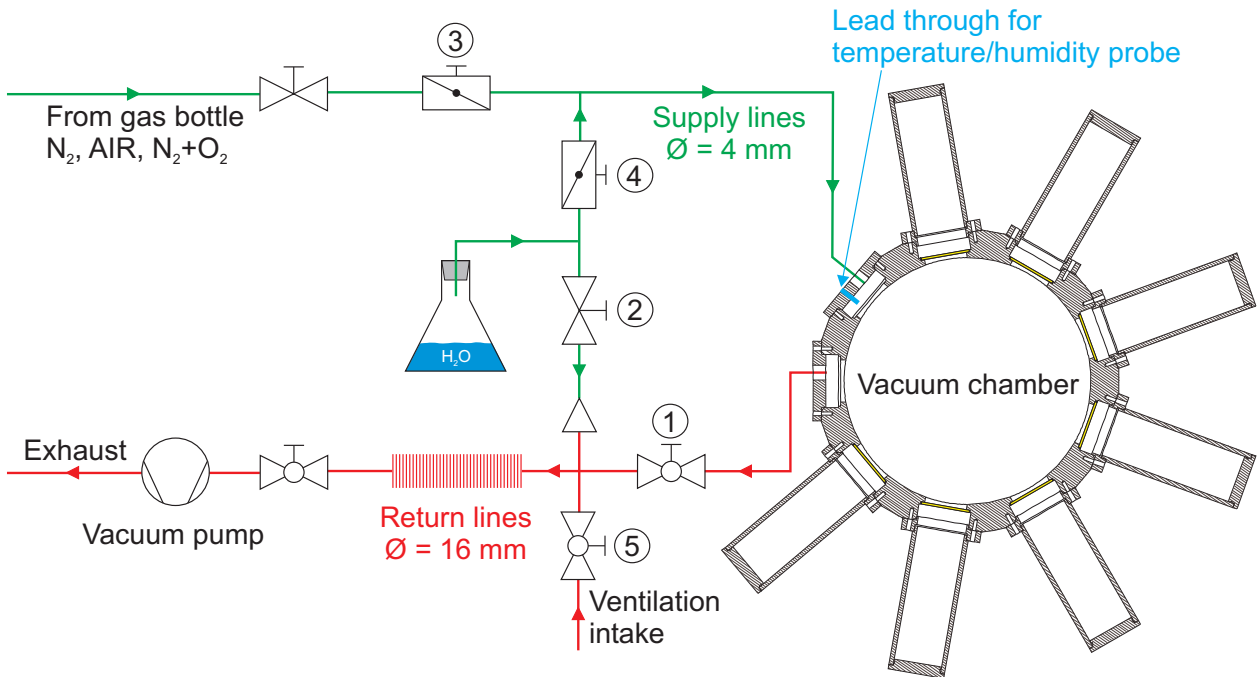


Fig. 3.14: Gas system of the AirLight experiment

can be heated by a heating coil, which is situated under the flask. The flask has to be well evacuated to remove all the rest atmosphere above the water. After having evacuated the flask and closing valve n°2, there should be a vapor pressure of about 23 hPa at room temperature inside. Now the water vapor can be filled into the evacuated chamber by opening valve n°4. Valves n°3 and n°4 are fine valves to adjust the gas flow into the chamber precisely.

To monitor the gas conditions inside the chamber, several probes have been installed. The temperature and the relative humidity are measured with a combined probe, which is installed near the gas inlet. The probe is an AHLBORN FH A646-E7C device and measures the temperature through a PT100 resistance and the dew point with a capacitive sensor. It is connected to an AHLBORN ALMEMO 2390-5 data logger, which directly calculates the relative humidity from the measured values. The absolute systematic uncertainty of the relative humidity amounts to 1.5 % rH in the range between 5 % to 98 % rH. The temperature measurement has a precision of 0.3 °C. The probe was calibrated by the factory relative to DKD¹-calibrated sensors.

The pressure sensor is placed at the top of the chamber and measures the pressure with a BALZERS piezo-electric device. It is connected to a BALZERS pressure-indicator, which can be calibrated with two adjusting screws. The first screw sets the zero offset and the second screw adjusts the calibration slope. To calibrate the device, the chamber has been evacuated completely and the zero pressure point has been adjusted with the first screw. Afterwards, the venting valve was opened to equalize the pressure inside the chamber with the ambient

¹Deutscher Kalibrierdienst (German calibration service)

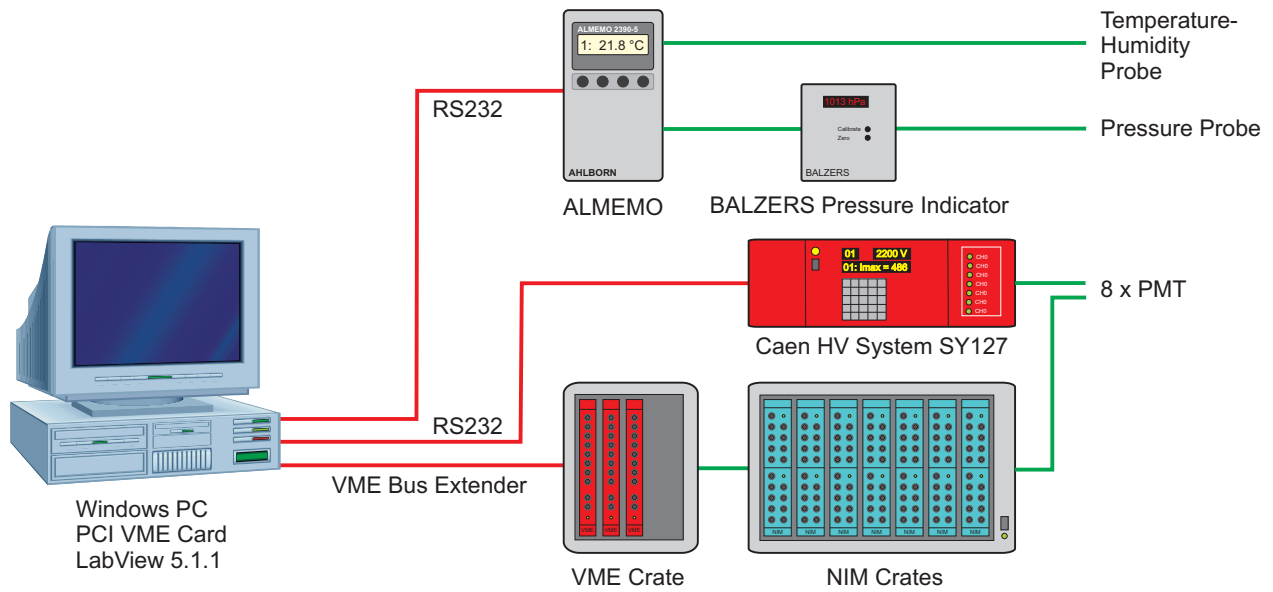


Fig. 3.15: Data Acquisition system of the AirLight experiment

pressure. Then the correct pressure value has been adjusted relatively to the known ambient pressure using the calibration screw. The BALZERS pressure-indicator provides an analog output signal between 0 and 10 volts. This output is connected to the ALMEMO data logger, which is able to convert the analog voltage value directly into the corresponding pressure value by multiplying it with 100 hPa/V. The systematic uncertainty of the zero adjustment is in the order on 1 hPa and of the calibration slope of about 0.3 %. Therefore the total systematic pressure error results to be $\Delta p = \sqrt{(1 \text{ hPa})^2 + (0.3 \% \cdot p)^2}$.

3.4 Data Acquisition

A sketch of the data acquisition system is shown in Fig. 3.15. It is controlled by a personal computer with the Microsoft Windows 2000 operating system. The experimental control is written in LabView 5.1.1 from National Instruments, which provides easy and fast access to the hardware devices. There are two kinds of quantities to be measured in the experiment. The experimental conditions are monitored by slow varying quantities such as temperature, pressure, relative humidity, high voltage, and current values. These quantities are read out through RS232 connections. The important experimental quantities of the individual events are the ADC, TDC, and Scaler values, which are accumulating with very high rates. These values are stored in the hardware buffers of the modules and are controlled and read out over a fast VME²-bus system. The measurement is performed as a coincidence measurement between the electron signals and the photon signals. In this way it is possible to minimize the background due to dark count rates of the PMTs or uncorrelated signals due to ambient

²VME: Versa Module Europa (IEEE 1014-1987)

or cosmic radiation. The selection of the coincident events is done by a fast NIM³-logic, which is described in the following section.

3.4.1 Coincidence Logic

A wiring scheme of the NIM-logic is illustrated in Fig. 3.16, where green connections symbolize analog signals and digital NIM pulses are exchanged along the red lines. A NIM pulse has a rectangular shape with an amplitude of -800 mV at 50 Ω impedance. The logic can be subdivided into a photon branch, composed by seven individual photon channels, and an electron branch. It selects coincident events between the electron signals and the photon signals. The coincidence condition is fulfilled, if a photon signal occurs within 120 ns after an electron signal has been detected.

First of all, the signals of the electron and photon branches have to be split up into two identical signals. One of them is passing through the NIM-logic, whereas the other one is passively delayed by coaxial cables and directly connected to the LRS⁴ 1182 ADC-module to measure its charge content. The splitting decreases the signal amplitudes by a factor of two. The signals of the photon branch correspond to single photoelectron signals, whereas the electron signals are multi photoelectron pulses with a large amplitude. Therefore the electron signal is attenuated before splitting to fit into the dynamic range of the ADC. After splitting, the photon signals pass through a constant fraction discriminator (CF4000), which generates a NIM-Pulse of 10 ns width, if the signal exceeds the trigger threshold of \sim -25 mV. The threshold for the electrons corresponds to \sim -40 mV and the generated pulse is 120 ns long. The CF4000 is used to improve the time resolution of the experiment. Normal leading edge discriminators trigger, if a signal exceeds a certain constant threshold level. If the signals are changing their amplitudes, this leads to different trigger times relative to the time of the maximum value. This can have negative effects on the time resolution of a measurement. Constant fraction discriminators overcome most of this problem by always triggering at a constant fraction of the maximum signal amplitude.

The NIM-pulses coming out of the CF4000 again have to pass through another leading edge discriminator (LRS 821). Now leading edge discriminators can be used without any effect on the time resolution, because the NIM-pulses have a well defined shape and amplitude. The second discriminator serves as coincidence unit for the photon signals. Its threshold is set to -400 mV (half NIM amplitude) and it transforms the incoming pulse into a 120 ns long NIM pulse, if the veto is not set. The veto is set or removed through the inverted 120 ns long output pulse of the second leading edge discriminator of the electron branch. This second discriminator for the electron signals inhibits itself for 300 ns after an electron signal has triggered to avoid multiple triggers, if there is more than one electron signal within 300 ns.

All channels of the photon branch are treated in the same way and are completely identical. After checking for coincidences with the second discriminator, the output pulses of all photon channels are merged together in the fan-in/out-module (LRS 429A). If an event consists of

³NIM: Nuclear Instrument Module

⁴LRS: Lecroy Research Systems

more than one coincident photon signals, the width of the output pulse of the LRS 429A in general will be larger than or equal to 120 ns.

The output pulses of the two discriminators, of the fan-in/out-module and of the second discriminator of the electron branch are routed on a Scaler-module (CAEN V260) to count the absolute numbers of free and coincident photon and electron signals.

The subsequent modules are needed to sample the time and pulse height distributions of the photon signals as well as the electron energy spectra. The data acquisition is able to automatically switch between two sampling modes, the coincident mode and the free electron mode. This way it is possible to either sample coincident events or free electron events. This is important, because the energy spectrum of the coincident electrons in general is not the same as the energy spectrum of the free electrons. The free energy spectrum plays an important role in the data analysis and the energy calibration, since it reflects the real energy distribution of the incoming electrons.

In normal coincident mode the ADC gate of 300 ns and the corresponding common stop signal for the TDC are generated after a coincident pulse comes out of the fan in/out module. The ADC gate is coupled with the analog photon signal, which is delayed by 45 ns relative to the leading edge of the ADC gate. The associated electron signal moves freely in an interval of 120 ns around the photon signal, as is illustrated in Fig. 3.17. The delay between the leading edge of the ADC-gate and the first incoming signal is guaranteed to be at least 30 ns. Furthermore, the distance between electron signal and the end of the ADC-gate is always larger than ~ 100 ns to ensure the whole signal tail to be measured.

After every tenth coincidence the rate divider RD2000 triggers the start signal of the gate generator LRS222, what switches the system into free electron mode. Therefore the next electron signal will pass through the whole logic, regardless whether it is coincident or not. The free electron events can be identified later by means of their time signature in the TDC spectrum. In this mode the electron signal has a constant delay of 172 ns relative to the leading edge of the ADC gate, as is shown in Fig. 3.18. After the free electron event has passed the logic, the system switches back to coincident mode.

Because the ADC needs 16 μ s to convert an incoming event, the OR-module LRS 622 inhibits itself for this time after a gate signal was generated. Furthermore, the ADC provides an CIP (Conversion In Progress) output signal whenever it is busy or not ready. This signal is merged together with the veto signal for the OR-module using the gate generator LRS 222. If the OR-module is inhibited, the whole sampling unit of ADC and TDC is blocked as well. In this way it is guaranteed that all the modules are ready when they receive a new signal. The final conversion of the events into digital values is done by the VME-based Scaler-, ADC-, and TDC-modules. The CAEN V260 scaler module is counting the incoming NIM-pulses. Its 16 channels are divided into 7 free and 7 coincident photon counters, as well as one free and coincident electron counter respectively. Each channel has a dynamic range of 24 bit with a guaranteed input frequency of 100 MHz. The scaler values are used to measure the absolute numbers of coincidences or electrons, since the sampling system is always losing some events during data conversion or read out of the module buffers.

The 8 channel Lecroy 1182 ADC measures and converts the charge content of the incoming

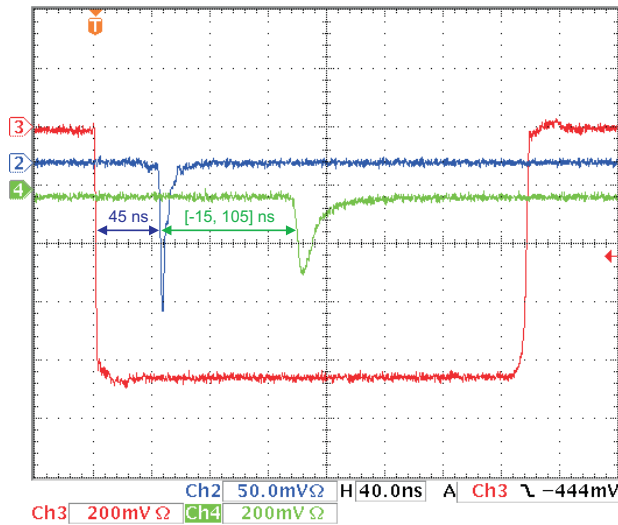


Fig. 3.17: ADC-gate with photon signal and electron signal in coincident mode.

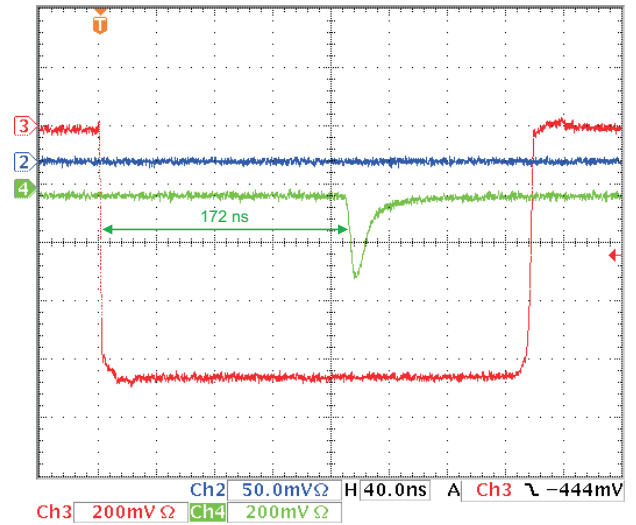


Fig. 3.18: ADC-gate with electron signal in free electron mode.

signals with a charge resolution of 50 fC/count and a dynamic range of 12 bit per channel. It is used to sample the pulse height distributions of the PMT signals and the electron spectrum respectively. As long as the gate is open, the ADC converts all the 8 signal channels and stores the converted events in a FIFO memory buffer. The buffer size corresponds to 16 events. If the buffer is full, the CIP signal will be set and therefore the whole sampling system is blocked for new events as long as the ADC buffer will be read out and reset.

The measurement of the time differences between electron and photon signal is done by the 8 channel CAEN V488 TDC-module. Its dynamic range amounts to 12 bit and its time range was set to 400 ns. The module is operated in common stop mode. The time measurement for a single channel will start as soon as the leading edge of a coincident NIM pulse will reach the TDC. The common stop signal for all channels is provided by the corresponding electron NIM pulse, which was delayed by 260 ns to arrive at the TDC later than the photon pulses. Before entering the TDC, the electron pulse is again checked for coincidence with the ADC gate using the AND-module LRS 465. Thus the TDC will be blocked by the CIP-veto as well, what guarantees the consistency between the ADC and TDC events. After a common stop signal has reached the TDC, it will convert the measured time differences into TDC-counts and store the values in the memory buffer. The maximum conversion time is 13 μ s, if all channels have valid entries. The minimum number of events, which can be stored in the buffer, is 56. Since the buffer size of the ADC is much lower, it has to get the highest priority for data readout.

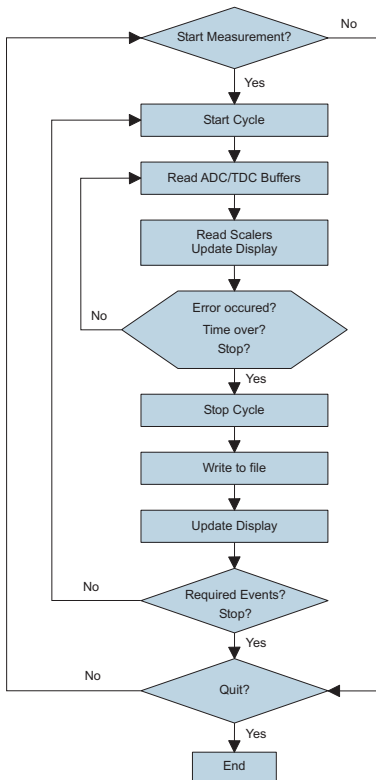


Fig. 3.19: Major processes of the data acquisition routine.

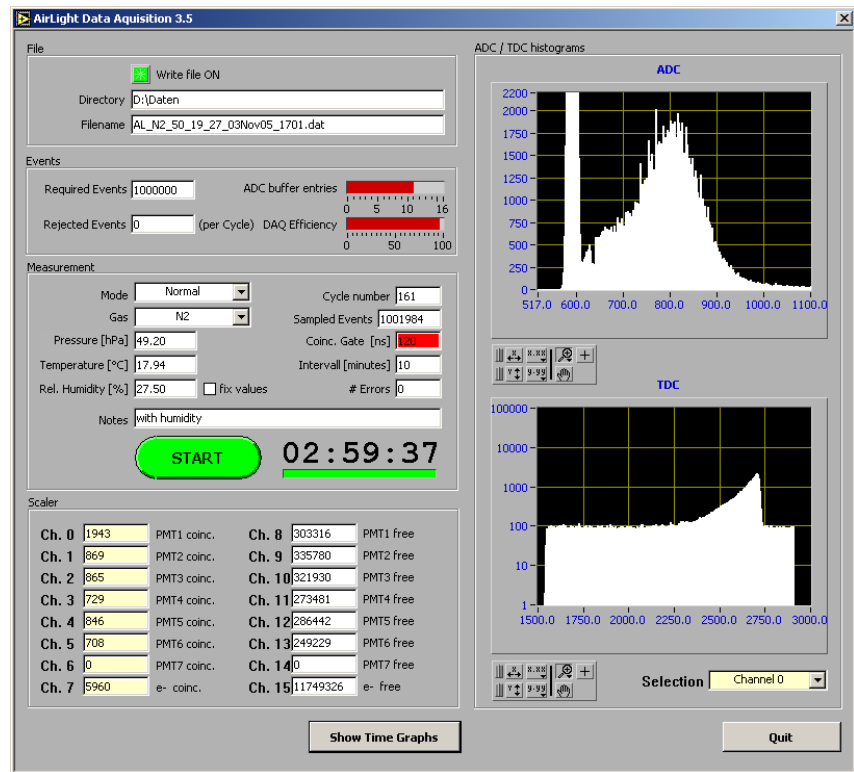


Fig. 3.20: Main display of the data acquisition, showing a photon pulse height distribution and the corresponding difference time spectrum for channel 0.

3.4.2 Experimental Control

The experiment is controlled by routines written in LabView 5.1.1 [46] and the general structure of the procedures is illustrated in Fig. 3.19. To collect sufficient statistics, a measurement has to run for typically 12 to 30 hours (depending on the kind of gas and the pressure). Therefore the stability of the detectors and the gas are very important and have to be monitored carefully. Possible crashes of a measurement due to electrical power breakdown or temporary errors during the data acquisition should not lead to a complete loss of already acquired data. Therefore a measurement run is subdivided into cycles of usually 10 minutes duration. Every cycle acts as an independent measurement. At the start of a cycle the current experimental conditions such as temperature, pressure, and relative humidity as well as the PMT voltages and currents are read into the cycle buffer. Furthermore, the ADC-, TDC-, and Scaler-modules are reset and the start time is retrieved. During the cycle the FIFO-buffer of the ADC is continuously watched in a loop. When the ADC buffer has reached its maximum number of 16 events, the ADC- and TDC-buffers are read out and their data is merged together. During merging the data is checked for the right ordering. If there are some obvious inconsistencies between the ADC and TDC events, all the 16 events are rejected. Additionally, every 500 ms the scaler values are read out and the main display

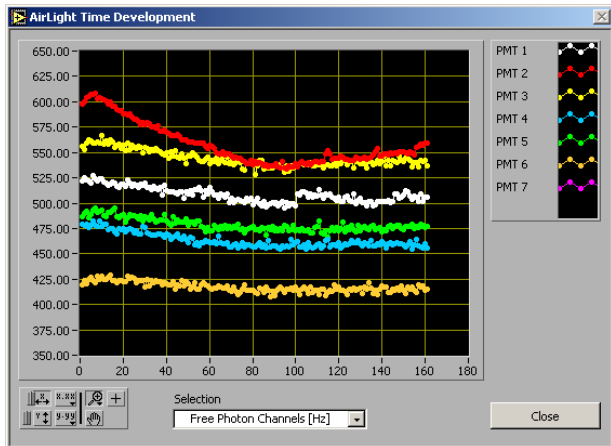


Fig. 3.21: Time development display to monitor the stability of the different observables during the run. In this example the free PMT rates are plotted versus the cycle number.

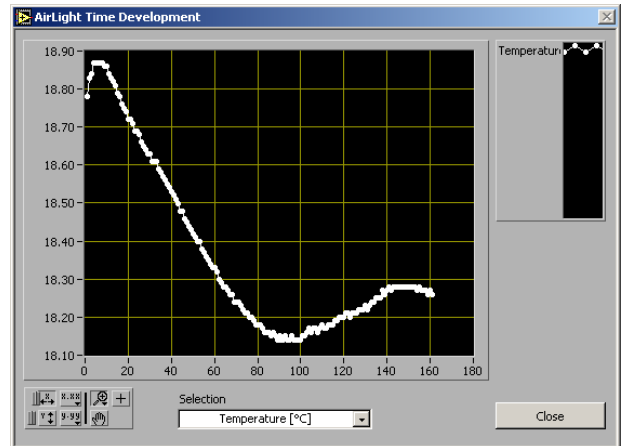


Fig. 3.22: Temperature variations during a run. Comparison with Fig. 3.21 gives an impression about the temperature sensitivity of the PMT rates.

is updated. After the cycle has been completed, the ADC-, TDC- and Scaler-modules are inhibited and the final scaler values as well as the stop time are written into the cycle buffer. If a non-critical error occurred, the error ID of the cycle gets a value other than zero. Afterwards, the cycle buffer is written into a file in ASCII-format. If the required number of events has not yet been reached, another cycle will be started. Otherwise the run will be stopped. A cycle always runs over its whole duration, even if the required number of events has already been reached. In case the run is stopped earlier, the last cycle will not be saved. This ensures the acquisition time to be equal in all cycles.

Main Display

On the main display shown in Fig. 3.20 the user can choose different settings and observe the status of the measurement. When a measurement is going to be started, the user has to enter the desired number of events he wants to capture (normally 1000000). Furthermore, the type of gas used for the measurement has to be specified. Temperature, pressure, and relative humidity of the gas are automatically determined but can also be entered manually, if the “fix values” check box is activated. Additionally, the cycle duration can be set in the “Interval”-field (default is 10 minutes). The measurement mode tells the program what kind of measurement is currently done. The “normal” mode corresponds to the standard fluorescence measurement. Other modes are energy calibration, time calibration and PMT calibration. The measurement mode mainly influences the name of the output file, which is automatically generated at the start of a run, if the “Write file” button is activated. On the lower left hand side of the main display the current scaler values are displayed. The left column shows the counters of the coincident events in each channel, and in the right column the corresponding free counts are listed. On the right hand side of the main display the

Channel	Assignment	ADC	TDC	Coin. Scaler	Free Scaler	Voltage	Current
0	M-UG6	ADC0	TDC0	SCL0	SCL8	V0	I0
1	317a	ADC1	TDC1	SCL1	SCL9	V1	I1
2	380a	ADC2	TDC2	SCL2	SCL10	V2	I2
3	360a	ADC3	TDC3	SCL3	SCL11	V3	I3
4	340a	ADC4	TDC4	SCL4	SCL12	V4	I4
5	394a	ADC5	TDC5	SCL5	SCL13	V5	I5
6	427a	ADC6	TDC6	SCL6	SCL14	V6	I6
7	Electrons	ADC7	TDC7	SCL7	SCL15	V7	I7

Table 3.2: Assignment of the ADC, TDC, Scaler and voltage/current values to the different channels.

3.4.3 Data Format

All data belonging to one run is stored in one ASCII-file. This ensures the readability of the data for everybody without any knowledge about the data format. The disadvantage is the rather large file size of about 60 MB for one million events. An example of a data file is shown in Fig. 3.23. At the beginning, the run header is stored with the initial information about the run. Afterwards, the cycle data is following. A cycle always starts at the “<CYCLCE START>” marker and ends with the “<CYCLE STOP>” marker. Each cycle has its own header containing the basic properties of the cycle. Then PMT-voltage and current values are stored in a row, followed by the row containing the 16 scaler values of the different channels. The first eight values correspond to the coincident scalers and the last ones to the free scalers. The rest of the cycle contains a table of the ADC and TDC values of each event. The assignment of all observables to the different channels is summarized in Table 3.2. This way all the information, which belongs to the measurement, is stored in one file. Each cycle is an independent sub-sample of the measurement. Therefore already stored data can be used for analysis, even if the measurement crashes at a certain point. Furthermore, it is possible to select the cycles for pressure, temperature, PMT-rates, or other criteria and discharge faulty cycles with error ID’s other than zero.

3.5 Calibration

Before the raw data is ready for analysis, the measured ADC and TDC values have to be converted into physical quantities. Furthermore, the relative calibration constants of the PMTs have to be determined, to enable the comparison of the fluorescence intensities measured by different channels. The corresponding calibration procedures will be described in the following sections.

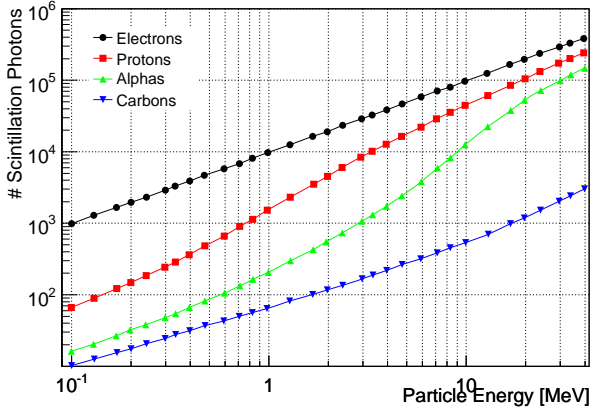


Fig. 3.24: Scintillation response curves for the BC-400 scintillator series (Manufacturers values).

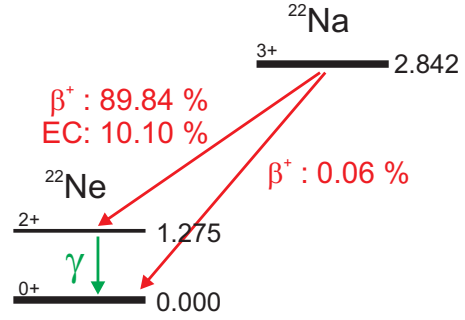


Fig. 3.25: Decay channels of ^{22}Na into ^{22}Ne , used for the energy calibration.

3.5.1 Energy Calibration

Ideally, the electrons are completely stopped in the scintillator and a constant fraction of their energy is transferred into scintillation photons. The number of produced photons is proportional to the electron energy deposit E_{dep} in the scintillator, as can be seen in Fig. 3.24. The relation between the number of scintillation photons and the energy deposit is given by the scintillation yield Y_{scint} of the scintillator material. A certain fraction ε_{det} (detection efficiency) of the scintillation photons is detected by the PMT. Each detected photon is inducing a photoelectron in the PMT photocathode, which subsequently will be multiplied by a constant factor G (gain) in the dynode stage of the PMT. Therefore the number of electrons N_e arriving at the PMT anode is proportional to the number of detected scintillation photons, which again is proportional to the energy deposit in the scintillator:

$$N_e = G \cdot \varepsilon_{det} \cdot Y_{scint} \cdot E_{dep} \quad (3.8)$$

The corresponding charge content to the anode signal, which is measured by the charge integrating ADC, results to be

$$Q = Q_{ped} + \int I_{anode}(t) dt = Q_{ped} + e \cdot N_e, \quad (3.9)$$

where e is the electron charge and Q_{ped} denotes the constant charge offset of the pedestal. Thus, there is again a linear relation between measured charge and the deposited energy. The energy resolution σ_E is related to the statistical error of the electron number N_e . Assuming this error to be Poissonian [30, 17], the energy resolution will be proportional to the square root of N_e and thus

$$\sigma_E \propto \sqrt{N_e} \propto \sqrt{E_{dep}} \quad (3.10)$$

The ADC is converting the measured charge contents of the PMT signals into ADC counts. One ADC count corresponds to 50 fC in the current setup. Since there is a linear relation be-

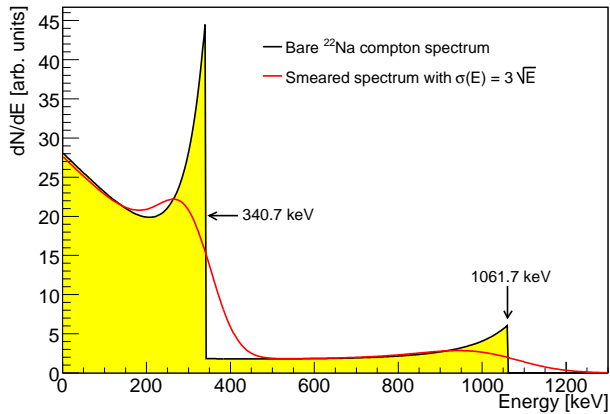


Fig. 3.26: Bare and smeared Compton spectrum of ^{22}Na .

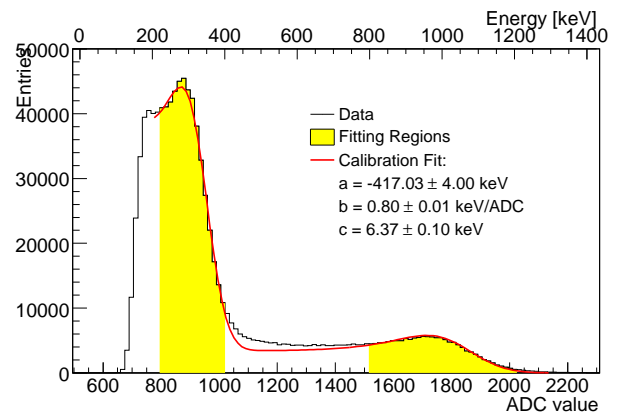


Fig. 3.27: Calibration fit to a measured ^{22}Na Compton spectrum.

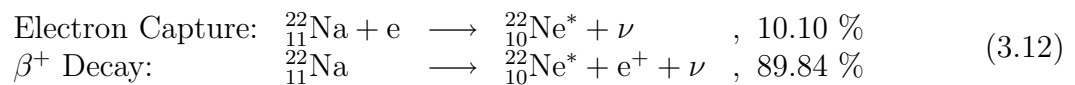
tween the measured charge and the deposited energy in the scintillator, the relation between the ADC value in channel 7 and the energy is of the following form:

$$E_{dep} = a + b \cdot ADC \quad , \quad \sigma_E = \sqrt{\sigma_{ped}^2 + c \cdot E_{dep}} \quad (3.11)$$

The fluctuations of the pedestal contribute as a constant offset σ_{ped} to the energy resolution and are in the order of 13 keV. The task of the energy calibration is to determine the constants a , b and c . In this work two different methods have been tested, as will be described in the following.

^{22}Na Method

The more conventional approach is the calibration by the measurement of a known energy spectrum, e.g. the compton spectrum of a ^{22}Na gamma emitter. Since ^{22}Na is an unstable isotope, it decays with a half life of 2.6 years to ^{22}Ne . There are mainly two relevant decay channels []:



Both of them result in the same excited nuclear state of ^{22}Ne , which subsequently relaxes by the emission of a 1274.5 keV gamma ray, as is illustrated in Fig. 3.25. The previously emitted positrons will annihilate immediately in the surrounding material, what leads to the emission of two 511 keV gammas. Therefore the ^{22}Na source can be considered as a pure gamma emitter with two mono-energetic lines in the energy spectrum. According to the branching ratios in (3.12), the relative intensities of the two lines should be 1.8 at 511 keV compared to 1.0 at 1274.5 keV. These gamma rays can be detected indirectly in the scintillation detector by means of secondary compton electrons. The energy spectrum of the compton scattered electrons can be derived classically by simple application of energy

and momentum conservation. The spectrum contains two compton edges at 340.67 keV and 1061.70 keV according to the two gamma energies, as is shown in Fig. 3.26. The energies at the edges correspond to the maximum energy transfer E_{max} to the electrons, when the gammas are scattered backwards:

$$E_{max} = \frac{2E_0\varepsilon^2}{1 + 2\varepsilon} \quad (3.13)$$

In this expression, ε corresponds to the ratio of the gamma energy to the electron mass $E_0 = 511$ keV. The shape of the compton spectrum can be expressed in terms of a differential cross-section for the energy transfer E to the electron:

$$\frac{d\sigma}{dE} \propto \frac{2E_0^3\varepsilon^4 - (4E_0^2\varepsilon^3 + 2E_0^2\varepsilon^2)E + (3E_0\varepsilon^2 + 2E_0\varepsilon + E_0)E^2 - \varepsilon E^3}{(E_0\varepsilon^2 - \varepsilon E)^2} \quad (3.14)$$

Since the kinetic energy E of the electrons cannot be larger than the maximum energy E_{max} , the cross section will vanish abruptly at this energy, what causes the sharp edge (compton edge) in the spectrum. Now the ^{22}Na spectrum can be described as a superposition of two compton spectra according to the two gamma energies:

$$\frac{dN}{dE} = w_1 \cdot \frac{d\sigma_1}{dE} + w_2 \cdot \frac{d\sigma_2}{dE} \quad (3.15)$$

The ratio between the weighting factors w_1 and w_2 has been found to be 3.2. The limited energy resolution of the detector can be taken into account, if the original energy spectrum is assumed to be smeared out by a gaussian function. Therefore the measured energy spectrum results to be a convolution between the bare spectrum (3.15) with a normalized Gaussian function $G(E, \sigma_E(E))$ with standard deviation $\sigma_E(E)$:

$$\frac{dN}{dE} = \int_0^{E_{max}^1} \frac{dN_1}{dE'} \cdot G(E - E', \sigma_E(E'))dE' + \int_0^{E_{max}^2} \frac{dN_2}{dE'} \cdot G(E - E', \sigma_E(E'))dE' \quad (3.16)$$

The integration of this expression can be done numerically. If the energy E is now substituted by the expression $E = a + b \cdot \text{ADC}$, function (3.16) can be applied to a measured ^{22}Na spectrum to figure out the calibration constants a , b and c , as it is done in Fig. 3.27. Apparently, the model for the energy spectrum does not fit perfectly to the measurement. This may be due to background events, which have not been subtracted. Nevertheless, the striking features of the spectrum, as the compton edges, are modelled well enough to extract the calibration constants with sufficient accuracy.

There are some basic problems with this calibration method. First of all, the ^{22}Na spectrum ends at roughly 1 MeV. The electrons which are going to be measured have energies up to 2.3 MeV. Therefore the ADC range between 1 MeV and 2 MeV is not covered by this method and the calibration has to be extrapolated over this range. Another problem arises due to experimental reasons. Since the electron source has to be substituted by the ^{22}Na source, the calibration can only be performed in between of the fluorescence measurements. Furthermore, the high voltage has to be switched off during the changing of the sources.

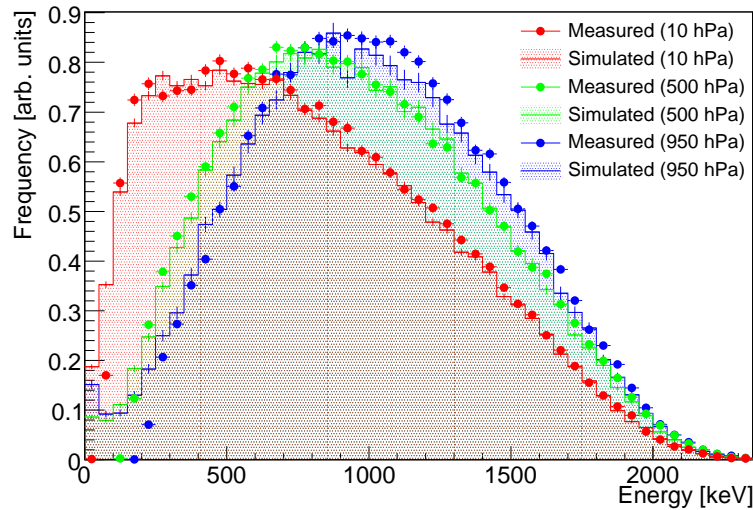


Fig. 3.28: Comparison between measured and simulated energy spectra at different pressures. The simulated spectra are matching nicely with the measured energy spectra.

Therefore the experimental conditions after reinstalling the electron source will probably not be the same as during the calibration. Since this calibration is rather cumbersome, it has just been applied every two or three weeks in between of a series of measurements. Therefore the calibration constants are required to be stable over the whole period of measurements, which is not very likely. All these problems can be solved by means of a Monte Carlo calibration.

Monte Carlo Method

The basic principle for the Monte Carlo calibration is the same as before. A known energy spectrum is required, which can be compared with a measured one. If the energy spectrum of the electron source would be known, the calibration could be done using this spectrum. The shape of the primary beta spectrum of the ^{90}Sr source can be calculated according to equation (4.2). However, this spectrum is strongly biased by energy losses due to scattering of the electrons in the source, the collimator and even in the gas inside the chamber. Therefore the energy spectrum changes its shape according to the pressure, as can be seen in Fig. 3.28. For high pressures the spectrum becomes harder than for low pressures, since high energetic electrons are less affected by the scattering. An analytical description of all these effects is hardly possible, but instead of that, an appropriate simulation can be applied, as is described in Section 4. Simulations have been done for all pressure values used for the measurements. To obtain correct results, the electrons have been generated isotropically in all directions within the source. Since the opening of the collimator is rather small, roughly 1000 electrons had to be generated to detect one electron in the scintillator. To collect sufficient statistics, 300×10^6 electrons have been generated per run, corresponding to roughly 10 s of real measurement and one week of simulation time. The output of the simulation reflects the electron energy deposit distribution in the scintillator in terms of a histogram $h(i)$ with a bin width of $\Delta E = 25$ keV. The energy E_i at the bin center calculates as $E_i = \Delta E \cdot (i + \frac{1}{2})$

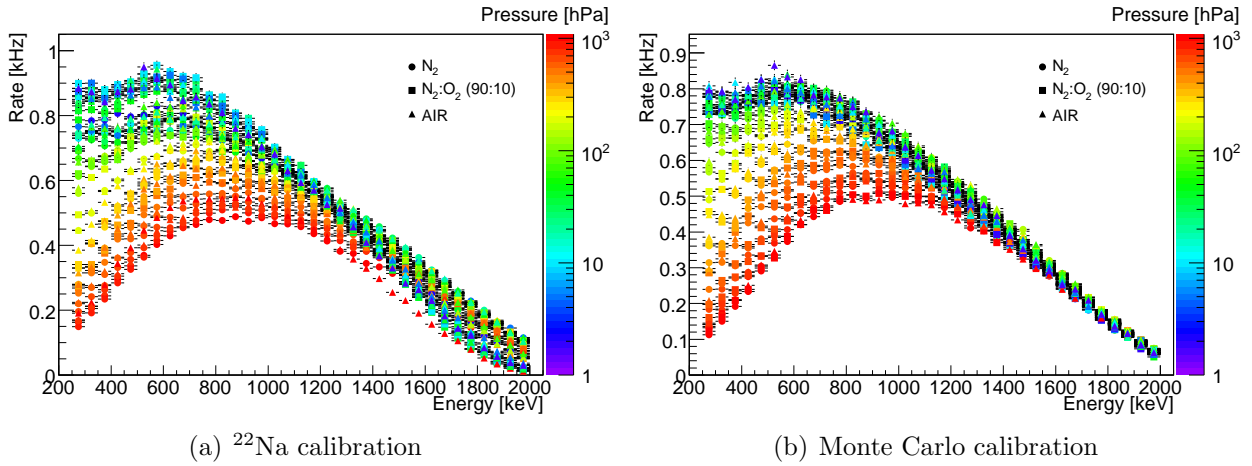


Fig. 3.29: Superimposed energy spectra for different pressures. The same data has been calibrated according to the two different calibration methods. The Monte Carlo method achieves a much better matching of the spectra at high energies and is stable against run-to-run variations.

with $i = 0, 1, \dots, i_{max}$. This energy distribution again has to be convoluted with a Gaussian function to take into account the limited energy resolution of the detector. Simultaneously, the convolution smoothes the histogram, which causes the resulting energy spectrum to have a continuous shape:

$$\frac{dN}{dE} = \sum_i \frac{h(i)}{\sqrt{2\pi}\sigma_E(E_i)} \cdot e^{-\frac{(E-E_i)^2}{2\sigma_E^2(E_i)}} \quad (3.17)$$

This spectrum now can be used in the same manner as the ^{22}Na spectrum to determine the calibration constants.

The big advantage of this method is the possibility to apply it individually to every measurement, since the free energy spectrum of the electrons is always measured simultaneously. This avoids systematic run-to-run errors due to unstable calibration constants, as can be seen in Fig. 3.29. Furthermore, the calibration naturally covers the whole energy range of the electrons, what makes it more reliable. Therefore the Monte-Carlo method has been chosen for the energy calibration of measurements, where the ^{90}Sr source is invoked. Nevertheless, the ^{22}Na method is useful, if an unknown energy spectrum, e.g the background in the electron detector, is going to be measured. Typical values for the calibration constants turned out to be in the order of

$$a = -406 \text{ keV} \quad , \quad b = 0.80 \frac{\text{keV}}{\text{ADC}} \quad (3.18)$$

The energy resolution has been found to be

$$c = 9.9 \text{ keV} \quad \Rightarrow \quad \frac{\sigma_E}{E} \sim 10 \% \cdot \sqrt{\frac{1000 \text{ keV}}{E}} \quad (3.19)$$

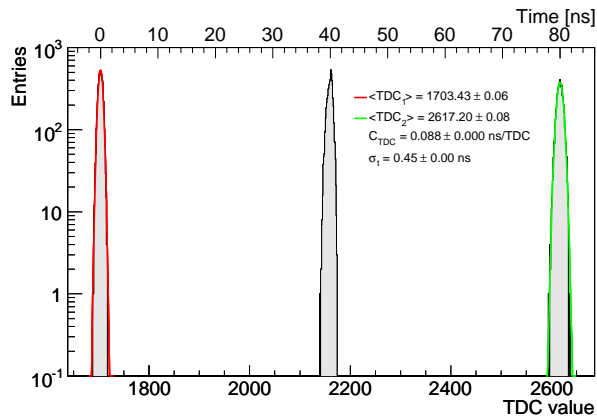


Fig. 3.30: The time calibration has been performed by means of equidistant artificial pulses at a distance of 40 ns.

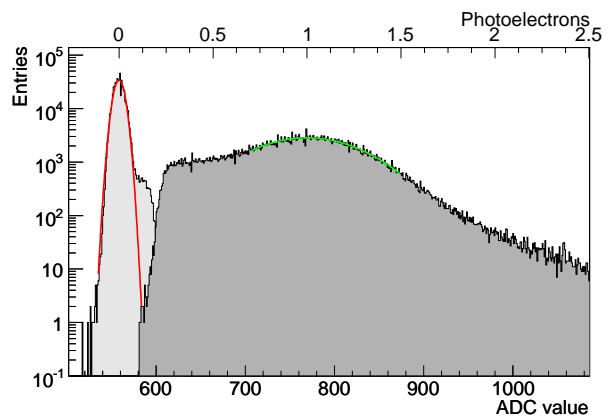


Fig. 3.31: Typical pulse height distribution of the PMTs in the photon detectors. Gaussian fits were performed to determine the photoelectron scale.

3.5.2 Time Calibration

The time calibration is a very simple operation. The TDC is measuring the time differences between the start NIM pulses of the different photon channels and the common stop NIM pulse of the electron channel. Afterwards, the time values are converted into TDC values depending on the time range of the TDC, which was set to 400 ns. Therefore the corresponding bin width follows to be 0.104 ns per TDC. In principle, this already is the desired calibration constant. Nevertheless, it is worthwhile to check these values independently. The calibration measurement was done with a so-called “flight-time generator”, which provides a start pulse and, subsequently, equidistant time pulses every 40 ns. These pulses were used to trigger the discriminators of the NIM-logic. The recorded time spectrum is shown in Fig. 3.30. A gaussian fit to the right and the left pulse delivers the corresponding TDC values. The calibration constant now can be calculated according to

$$C_{TDC} = \frac{80 \text{ ns}}{\text{TDC}_2 - \text{TDC}_1} = 0.088 \frac{\text{ns}}{\text{TDC}} \quad (3.20)$$

This value is just in rough agreement with the bin width derived from the time range settings. The standard deviations of about 0.45 ns are an estimate of the time resolution of this photon channel. Nevertheless, the time resolution in a fluorescence measurement in general will be larger, because the shape of the photon and electron pulses is not rectangular, as it was the case for the NIM pulses during the calibration.

During data conversion the timescale of the TDC-values has to be inverted, because the TDC is operated in common stop mode. Since the absolute time scale plays no role for the analysis, the first time bin of the coincidence interval is moved to zero per definition. In doing so, the time scale is well defined for all measurements. Since the hardware coincidence interval has a fixed width of ~ 120 ns, the time entries should not exceed 120 ns, if the time calibration and data conversion has been done correctly.

3.5.3 Photoelectron Conversion

Similar to the conversion of TDC to time, or ADC to energy values, the ADC values of the photon channels (channels 0 - 6) are converted to photoelectrons. This has the advantage of being independent from variations of the pedestal position or the gain of the PMTs between different measurements. If the single photoelectron spectrum is assumed to have a characteristic shape for every PMT, this shape should be roughly the same for all measurements. The conversion to photoelectrons is done by fitting two gaussian functions to the pedestal and the single photoelectron peak, as is shown in Fig. 3.31. The mean value of the pedestal corresponds to zero photoelectrons (0 pe), whereas the mean value of the single photoelectron peak is defined as one photoelectron (1 pe). This procedure is done individually for every measurement and every photon channel. Afterwards, cuts on the number of photoelectrons can be applied very easily. For the following analysis a photoelectron range between 0.5 pe and 2 pe has been chosen for all data samples. This range is also used for the relative calibration of the PMTs and the background measurements described in the subsequent sections.

3.5.4 Relative Calibration of the Photomultipliers

The relative calibration of the photon channels against each other is very important for the spectral analysis of the different nitrogen bands. Therefore the detection efficiencies ε_{det} of each channel have to be determined. The relation between the total number of emitted photons and the number of detected photons is given by

$$N_{det} = N \cdot \underbrace{\varepsilon_{cut} \cdot \varepsilon_{\Omega} \cdot \int_{\lambda} \varepsilon_{QE}(\lambda) \cdot T(\lambda) \cdot \frac{d\hat{N}}{d\lambda} d\lambda}_{\varepsilon_{det}} \quad (3.21)$$

where $\frac{d\hat{N}}{d\lambda}$ is the normalized spectral distribution and N is the number of photons in the chamber. $T(\lambda)$ denotes the total transmission factor through quartz window and filters (weighted by the incidence angles) and ε_{QE} corresponds to the quantum efficiency of the PMT. Furthermore, the geometrical factor (acceptance) is described by ε_{Ω} , and ε_{cut} is the fraction of photon events surviving the cut on the photoelectron number as described above. Most of these quantities are known, except of the cut efficiency ε_{cut} and the quantum efficiency ε_{QE} . The cut efficiency just is a constant factor, which should not change as long as the pulse height distribution of the PMT is stable and the cut always is the same. The wavelength dependence of the quantum efficiency actually is completely unknown, since the PMTs are not absolutely calibrated.

Nevertheless, average values of the quantum efficiency $\varepsilon_{QE}^0(\lambda)$ are given in the manufacturers data of the PMTs and are shown in Fig. 3.7. Using these values, the quantum efficiency of an individual PMT can approximately be described as $\varepsilon_{QE}(\lambda) = f \cdot \varepsilon_{QE}^0(\lambda)$. Since f is a

constant factor, it can be moved out of the integral and thus equation (3.21) transforms to

$$N_{det} = N \cdot \varepsilon_{cut} \cdot \varepsilon_{\Omega} \cdot f \cdot \underbrace{\int_{\lambda} \varepsilon_{QE}^0(\lambda) \cdot T(\lambda) \cdot \frac{d\hat{N}}{d\lambda} d\lambda}_{\varepsilon_s} \quad (3.22)$$

It follows for each channel i , that the ratio between the detected number of photons N_{det}^i and the spectral efficiency ε_s^i is proportional to the total number of photons N in the chamber according to:

$$\frac{N_{det}^i}{\varepsilon_s^i} = N \cdot \varepsilon_{\Omega}^i \cdot \varepsilon_{cut}^i \cdot f_i = N \cdot \varepsilon_{\Omega}^i \cdot \hat{f}_i \quad (3.23)$$

A new calibration factor $\hat{f}_i = \varepsilon_{cut}^i \cdot f_i$ can be defined, which is the only unknown channel specific constant, since ε_{Ω}^i can be calculated from simulations. Thus, if the spectrum and the total number of photons in the chamber is known, it is possible to determine the calibration factors \hat{f}_i absolutely. If just the photon spectrum is known, it at least is possible to perform a relative calibration, since the relation between the calibration factors does not depend on the absolute numbers:

$$\hat{f}_i = \frac{N_{det}^i}{N_{det}^k} \cdot \frac{\varepsilon_s^k \cdot \varepsilon_{\Omega}^k}{\varepsilon_s^i \cdot \varepsilon_{\Omega}^i} \cdot \hat{f}_k = \frac{N_{det}^i}{N_{det}^k} \cdot \frac{\varepsilon_s^k}{\varepsilon_s^i} \cdot \hat{f}_k \quad (3.24)$$

If the photons are emitted symmetrically to the chamber axis, all photon detectors receive the same fraction of photons and thus the acceptances ε_{Ω} cancel. Therefore an ideal calibration light source has to be aligned on the chamber axis and has to have a stable and symmetric emission characteristic.

Calibration Procedure

The calibration of the PMTs has been done without filters. The reason is the big difference of counting rates between the channel with the M-UG6 filter and the other channels with the interference filters. Furthermore, the angular dependence of the interference filters would require the exact knowledge of the photon angular distribution to be able to calculate the effective transmission function $T(\lambda)$. Another important reason is the rather large systematic parametrization error of 3 % of the interference filters, described in Section 3.2, which would propagate to the calibration factors. Without the filters, the transmission factor $T(\lambda)$ just accounts for the quartz window, which is the same for all channels.

As photon source, a DH-2000 Deuterium Tungsten Halogen light source from Ocean Optics has been used, which provides a stable and continuous spectrum between 215 nm and 2000 nm. The light is guided through a fiber optic cable into a cylindrical diffusor placed in the chamber center, as is shown in Fig. 3.32. The diffusor mainly consists of a cavity of sintered teflon, where the light undergoes multiple reflections as in an Ulbricht sphere. As a consequence the angular distribution of the photons should nearly become isotropic. A small fraction of photons is able to penetrate the teflon and to escape through the exit slit of 3 mm height. Since the whole diffusor is axially symmetric and the light is entering the

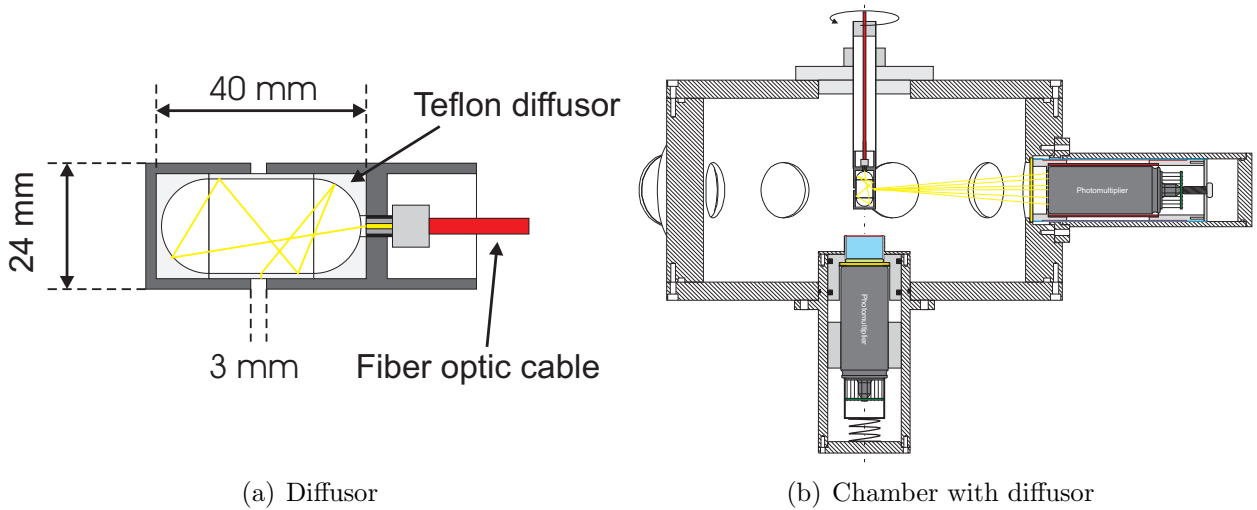


Fig. 3.32: Calibration light source with diffuser, as it is placed in the chamber center. The light source was turned by 40° steps during a calibration run.

diffusor along the axis, the angular distribution of the emitted photons should also follow this symmetry. Therefore the acceptances ε_Ω^i cancel in equation (3.24). Before entering the diffusor, the photons have to pass a M-UG6 filter to select only photons in the wavelength range between 300 nm and 420 nm. The spectral distribution of the photons can be figured out by the inversion of the optical light path. To do so the whole diffusor, including the fiber optic cable, was put in front of the deuterium light source. Afterwards, the spectrum of the light coming out of the fiber optic cable, was measured with a spectrometer and was finally weighted by the transmission function of the M-UG6 filter. The resulting spectrum is shown in Fig. 3.33. This spectrum has been used to evaluate the Integrals I_i of the different photon channels. Because all channels, beside channel 1, are equipped with the same kind of PMTs and no filters are used, the integrals of these channels happen to be identical.

The calibration measurement was done by comparing the absolute count rates (scaler 8 - 14) of the photon detectors. The count rates are incorporating all PMT signals, which exceed the trigger threshold of the constant fraction discriminators. However, the calibration factors need to be determined within the same photoelectron range between 0.5 pe and 2.0 pe, as is used for the fluorescence measurements. Therefore the pulse height distributions of the PMT signals have to be known to calculate the count rates of signals surviving the photoelectron cut. With the current data acquisition system the sampling of the pulse height distributions can only be done in coincidence mode. Since the deuterium source is a continuous light source, there is no trigger provided, which can be used to enable the data sampling. Therefore the sampling has been done using accidental coincidences between the photon detector signals and an artificial electron trigger coming from a pulse generator with a frequency of 1000 Hz. The intensity of the light source was chosen in such a way that it generates as much statistics as possible, but on the other hand, still reproduces a single photoelectron distribution of the PMTs signals.

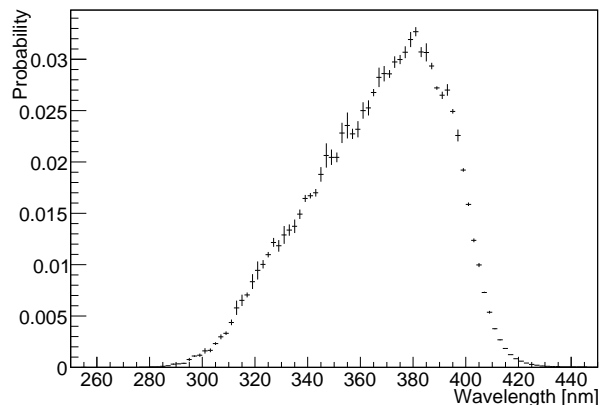


Fig. 3.33: Spectral distribution of the photons emerging from the diffusor.

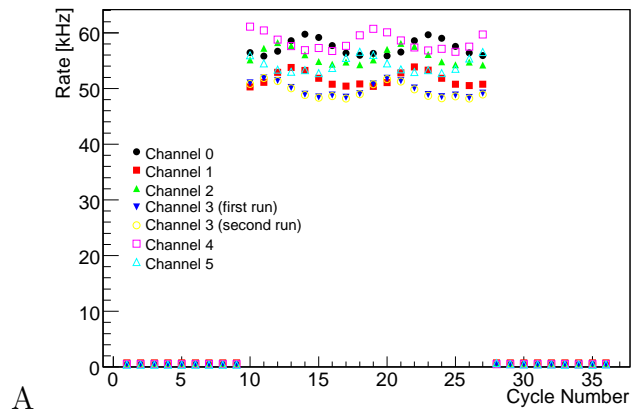


Fig. 3.34: Count rates of the photon detectors during a calibration run. The periodic variations are due to asymmetries of the diffusor. Cycles from 1 to 9 and 28 to 36 correspond to dark noise measurements.

Since it is not possible to construct the diffusor completely symmetric, there will be small intensity variations depending on the orientation of the diffusor to the PMTs. The angular distance between the PMTs amounts to 40 degree. Therefore a calibration measurement was subdivided into 2×9 single measurements of one minute duration. After each single measurement, the diffusor was turned for 40 degree towards the next PMT and then the subsequent measurement was started. The periodic variation between the count rates at the different diffusor orientations are shown in Fig. 3.34. Since all photon detectors have been exposed to all diffusor orientations for the same time, the sum of the count rates in each channel should be the same, if the detection efficiencies were equal. Therefore the summation of the count rates over all single measurements compensates for the deviations from the axial symmetry. Before and after the calibration measurements, the noise rate was measured by removing the fiber optic cable from the light source. The noise turned out to be of the order of 500 Hz and corresponds to the data points in Fig. 3.34 with cycle numbers from 1 to 9 and 28 to 36 respectively. To avoid biased results due to reflections at the quartz- or PMT windows, the calibration measurement was split into two runs, where just half of the shutters in front of the PMTs were opened. The first run was done for the channels 0 to 3 and the subsequent run from channel 3 to 6. Channel 3 has always been opened and thus is connecting the two measurements. Therefore the relative calibration constants have been determined with respect to channel 3.

Finally, the calibration constants in Table 3.3 have been derived according to equation (3.24), where the calibration constant \hat{f}_R of the reference channel 3 is defined to be equal to unity. Thus, the other calibration constants simply follow from

$$\hat{f}_i = \frac{N_{det}^i}{N_{det}^R} \cdot \frac{\varepsilon_s^R}{\varepsilon_s^i} \quad , \quad \hat{f}_R \equiv 1 \quad (3.25)$$

Date	Channel 0	Channel 1	Channel 2	Channel 3	Channel 4	Channel 5
08/01	1.13 ± 0.03	0.97 ± 0.03	1.10 ± 0.03	1.00 ± 0.00	1.17 ± 0.04	1.08 ± 0.03
08/24	1.14 ± 0.03	0.97 ± 0.03	1.12 ± 0.03	1.00 ± 0.00	1.16 ± 0.04	1.07 ± 0.03
09/23	1.13 ± 0.03	0.97 ± 0.03	1.12 ± 0.03	1.00 ± 0.00	1.17 ± 0.04	1.07 ± 0.03
10/27	1.14 ± 0.03	0.97 ± 0.03	1.12 ± 0.03	1.00 ± 0.00	1.16 ± 0.04	1.08 ± 0.03

Table 3.3: Relative calibration constants \hat{f}_i for a photoelectron range between 0.5 pe and 2 pe with respect to channel 3 (systematic errors are included). The stability is excellent over the whole period of measurements. Channel 6 is missing, since it was broken during the measurements.

The errors of this expression are obtained by Gaussian error propagation:

$$\frac{\Delta \hat{f}_i}{\hat{f}_i} = \sqrt{\left(\frac{\Delta N_{det}^i}{N_{det}^i}\right)^2 + \left(\frac{\Delta \varepsilon_s^i}{\varepsilon_s^i}\right)^2 + \left(\frac{\Delta N_{det}^R}{N_{det}^R}\right)^2 + \left(\frac{\Delta \varepsilon_s^R}{\varepsilon_s^R}\right)^2 + \left(\frac{\Delta \varepsilon_{cut}^i}{\varepsilon_{cut}^i}\right)^2 + \left(\frac{\Delta \varepsilon_{cut}^R}{\varepsilon_{cut}^R}\right)^2} \quad (3.26)$$

The last two relative errors under the square root account for statistical run-to-run variations of the cut efficiencies, which have been estimated to $\sim 2\%$ by the comparison of the single electron spectra of all performed measurements, as is shown in Fig. 5.1. The errors of the detected number of photons N_{det} are of statistical nature. The spectral efficiencies ε_s^i are evaluated numerically by the summation over the bins of the wavelength distribution shown in Fig. 3.33 according to:

$$\varepsilon_s^i = \sum_j \varepsilon_{QE}^0(\lambda_j) \cdot T(\lambda_j) \cdot P_j \quad (3.27)$$

where P_j is the probability for the photon wavelength to emerge from the wavelength bin j . The error of these integrals again is evaluated using Gaussian error propagation, since the summation is done over a large wavelength range and the real values of the quantum efficiency and the quartz glass transmission are assumed to scatter around their averaged value. The width of the scatter band of the quantum efficiency around its average value is assumed to be in the order of absolutely 1%, whereas the error of the quartz window transmission has been neglected.

As has already been mentioned, all the filters have to be removed for the calibration procedure. This is a very time consuming operation, because the PMTs have to stabilize afterwards for several hours before the measurement can be started. Therefore the calibrations have been performed just before and after a series of measurements every three of four weeks. Nevertheless, the calibration constants turned out to be very stable over the whole period of measurements as can be seen in Table 3.3.

The restriction of the relative calibration to a photoelectron range between 0.5 pe and 2 pe leads to a systematic underestimation of the measured signal as long as the calibration is not done in an absolute manner. Nevertheless, it is possible to quote an estimate for the absolute calibration. Events above 2 pe are considered to be mostly background or noise, but the signal content below 0.5 pe can not be neglected. Roughly 12% of the events (with respect to the

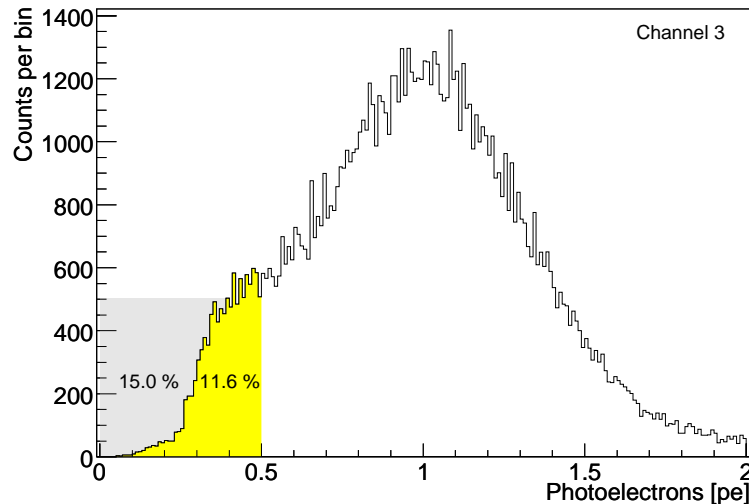


Fig. 3.35: Illustration for the absolute estimation of the calibration constant

events within the photoelectron range) are in between the discriminator threshold and 0.5 pe, as is illustrated in Fig. 3.35 by the yellow region. This fraction should be roughly the same during all measurements as long as the discriminator threshold is stable. The fraction of events between the pedestal at 0 pe and the discriminator threshold is completely unknown but can be estimated by the gray shaded region in Fig. 3.35, which amounts to 15 % of the detected events. Therefore the absolute number of events N can be estimated as

$$N = (1 + 12 \% + 7.5 \% \pm 7.5 \%) \cdot n = (1.195 \pm 0.075) \cdot n \quad (3.28)$$

where n denotes the measured events between 0.5 pe and 2 pe. If the absolute normalization uncertainty of the quantum efficiency ε_{QE} is assumed to be in the order of 10 %, an absolute calibration factor

$$C_{\text{abs}} = (1 \pm 0.1) \cdot \frac{N}{n} = 1.195 \pm 0.141 \quad , \quad \frac{\Delta C_{\text{abs}}}{C_{\text{abs}}} = 12\% \quad (3.29)$$

can be obtained by which the final results have to be scaled in order to get the absolute numbers.

3.6 Background Measurements

Background events can have a negative impact on the data analysis as long as their origin is not well understood. To figure out the background sources and intensities, appropriate measurements have been performed. It turned out that the background in all kinds of detectors is rather small. Nevertheless, especially for low pressure measurements, the background in the photon detectors is not negligible as will be shown in the next section.

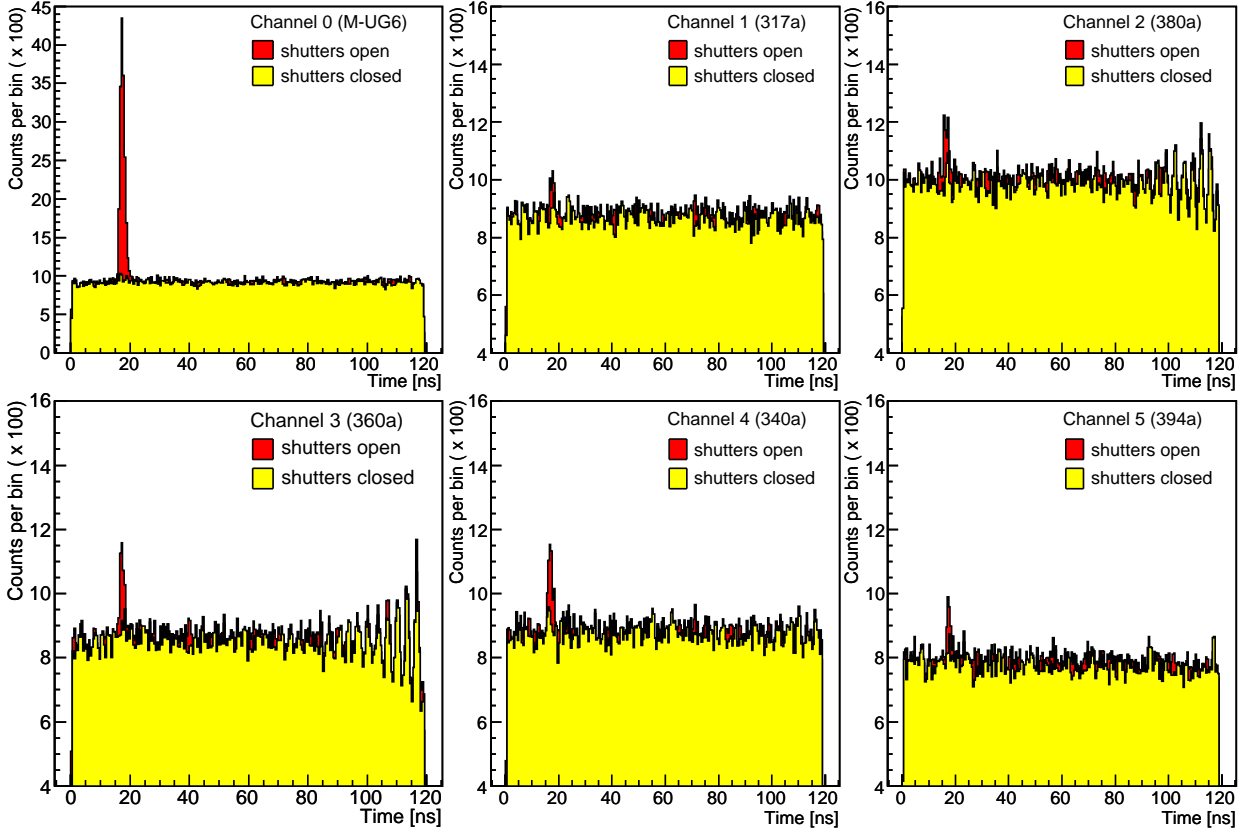


Fig. 3.36: Background time spectra measured with opened (red) and closed (yellow) shutters for energies between 250 keV and 2000 keV, normalized to the same number of 4.9×10^9 electrons. The periodic fluctuations in channels 2 and 3 between 100 ns and 120 ns are due to TDC deficiencies. These regions are not considered in the data analysis.

3.6.1 Background in the Photon Detectors

Background in the photon detectors can be either correlated or uncorrelated in time with an electron signal in the scintillator. Uncorrelated background, or noise, are accidental coincidences mainly originating from thermal emission of electrons in the photocathode or dynodes of the PMTs, but may also be induced by ambient or cosmic radiation. This background does not cause a lot of problems as long as the real signal is much stronger. Since it generates a flat distribution in the time spectra, it can easily be measured and subtracted from the total number of coincidences. The total number of uncorrelated background events N_B can also be calculated, if the total background rate R_B is known according to

$$N_B = R_B \cdot \Delta T \cdot N_e \quad (3.30)$$

where $\Delta T = 120$ ns is the width of the coincidence interval and N_e is the number of electron triggers. The background rate R_B can be estimated by the free rate of the PMT signals, if the signal rate is not too strong.

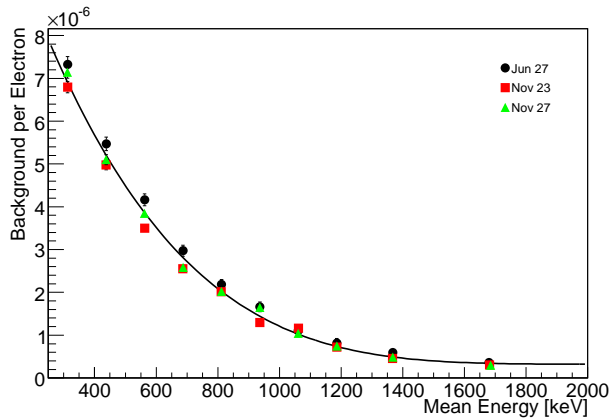


Fig. 3.37: Energy dependence of the background intensity in channel 0.

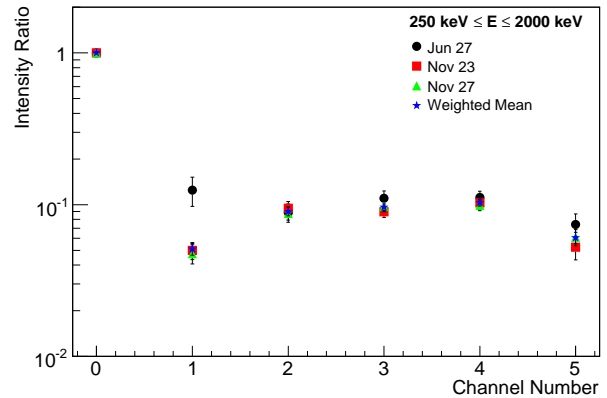


Fig. 3.38: Background intensity ratios relative to channel 0.

Background, which is time correlated with the electron signals, is much more problematic, because it can be mistaken for real fluorescence signals. This background needs to be modelled or parameterized to subtract it from the data. Possible sources of correlated background may be Bremsstrahlung or optical photons induced by electrons, which afterwards have been detected in the scintillator. Furthermore, cosmic air showers or muons may induce simultaneous signals in the electron and photon detectors. To figure out the intensity of such background, measurements have been performed in a completely evacuated chamber. Since the typical background rates of about 1 Hz per channel are rather small, a single measurement of two million background coincidences lasted over four days. The vacuum pump was always working during this time to minimize light emissions from residual gases inside the chamber. The measured time spectra for each channel are shown in Fig. 3.36. As can be seen immediately, most of the background was collected by channel 0, which is equipped with the M-UG6 filter. The background in the other channels with the interference filters is much weaker. This leads to the assumption that the background is mostly caused by optical photons, since background due to gamma radiation or air showers would be of the same order in all detectors. This assumption has been verified by an additional measurement with closed shutters corresponding to the yellow histograms in Fig. 3.36.

The first guess about the origin of the optical background photons was that they could be scintillation light from the electron detector, which was able to penetrate the thin foil covering the scintillator. If this was the case, the background should scale with the energy deposited in the scintillator and therefore with the energy of the electrons. To check this, the data of channel 0 has been analyzed in several energy intervals between 250 keV and 2000 keV and compared to each other. Gaussian fits have been applied to determine the intensity, width, and the mean time of the background peak, even if the background seems to have a slightly exponential behavior in time. Nevertheless, the decay constant is very short and thus a Gaussian shape should work sufficiently. The short lifetimes of the background signals additionally exclude residual nitrogen fluorescence as background source, since nitrogen lifetimes at low pressures are much larger. The result of this study could not confirm the

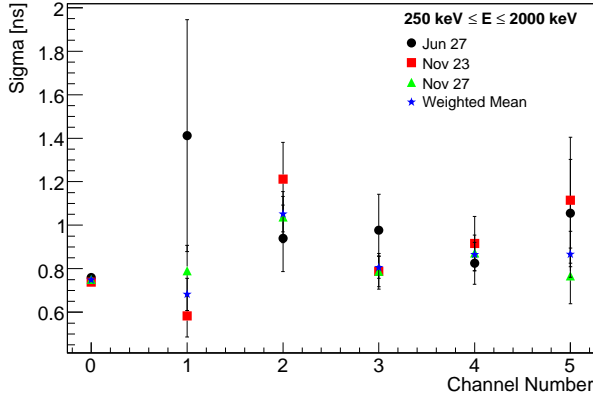


Fig. 3.39: Width of the background peaks in terms of one gaussian standard deviation.

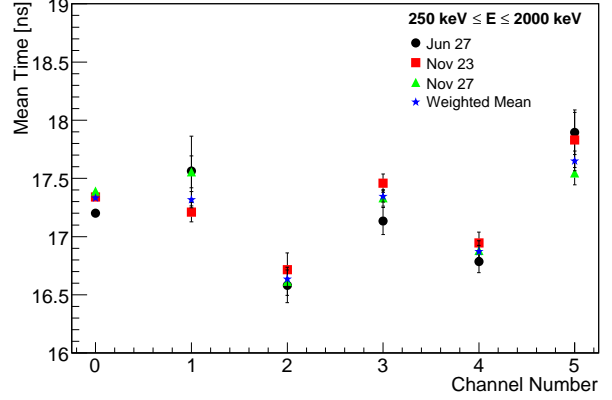


Fig. 3.40: Mean time of the background peaks.

background intensity to scale with the energy. Instead of this, the background is increasing with decreasing electron energies, as is shown in Fig. 3.37 for three independent measurements. Since it was not possible to identify the real nature of the background, its energy dependence was parameterized and fitted by the empirical formula

$$\varepsilon_B^0(E) = \frac{N_B}{N_e} = p_0 + p_1 \cdot (2000 \text{ keV} - E)^2 + p_2 \cdot (2000 \text{ keV} - E)^4 \quad (3.31)$$

where the three parameters p_i turned out to be:

$$p_0 = 3.22 \times 10^{-7} \quad , \quad p_1 = 1.15 \times 10^{-13} \quad , \quad p_2 = 7.72 \times 10^{-19} \quad (3.32)$$

Unfortunately, this kind of background analysis cannot be done with the other channels because their background signal is too weak. However, if the intensity difference between the channels is just caused by the different transmission factors of the channels, the energy dependence (3.31) should hold for every channel. In this case, the background efficiency for all channels can be described by:

$$\varepsilon_B^i(E) = R_i \cdot \varepsilon_B^0(E) \quad , \quad i = 0, \dots, 5 \quad (3.33)$$

The intensity ratios R_i of the channels i with respect to channel 0 again have been determined through gaussian fits to the background peaks using the full energy range between 250 keV and 2000 keV. Furthermore, these fits delivered the values for the width σ_i of the background signals in terms of one standard deviation and their mean times t_0^i , which should not depend on the energy. The values of three independent measurements shown in Fig. 3.38, Fig. 3.39 and Fig. 3.40 have been averaged and are summarized in table 3.4. Using these constants, the background per time interval can be evaluated according to:

$$\frac{dN_B}{dt} = \frac{R_i}{\sqrt{2\pi}\sigma_i} \cdot e^{-(t-t_0^i)^2/2\sigma_i^2} \cdot \int_E \varepsilon_B^0(E) \cdot \frac{dN_e}{dE} dE \quad (3.34)$$

Ch.	Int. Ratio [%]	t_0 [ns]	σ [ns]
0	100 ± 0.00	17.33 ± 0.01	0.75 ± 0.01
1	5.10 ± 0.46	17.32 ± 0.07	0.68 ± 0.07
2	9.03 ± 0.59	16.63 ± 0.08	1.05 ± 0.08
3	9.61 ± 0.50	17.35 ± 0.05	0.81 ± 0.05
4	10.3 ± 0.50	16.87 ± 0.05	0.87 ± 0.06
5	6.06 ± 0.53	17.65 ± 0.08	0.87 ± 0.11

Table 3.4: Constants for the background parametrization function.

However, the background intensity is rather weak and thus just plays a role for low pressure measurements below ~ 50 hPa, where the fluorescence signal is weak and additionally distributed over a broad time interval due to its large lifetimes.

3.6.2 Background in the Electron Detector

For the measurement of the background in the electron detector the ^{90}Sr source has been removed. A free background energy spectrum has been captured over a period of four days, as is shown in Fig. 3.41. The energy scale was obtained by means of the ^{22}Na method, since in this case the Monte Carlo calibration is not applicable. Most of the background happens to appear below 1200 keV. The overall background rate turned out to be 3.3 Hz and was stable over the whole run. Since the typical electron rates during the fluorescence measurements are always higher than 10 kHz, the fraction of background triggers is below 0.3 %. Therefore the background in the electron detector has been neglected in the following.

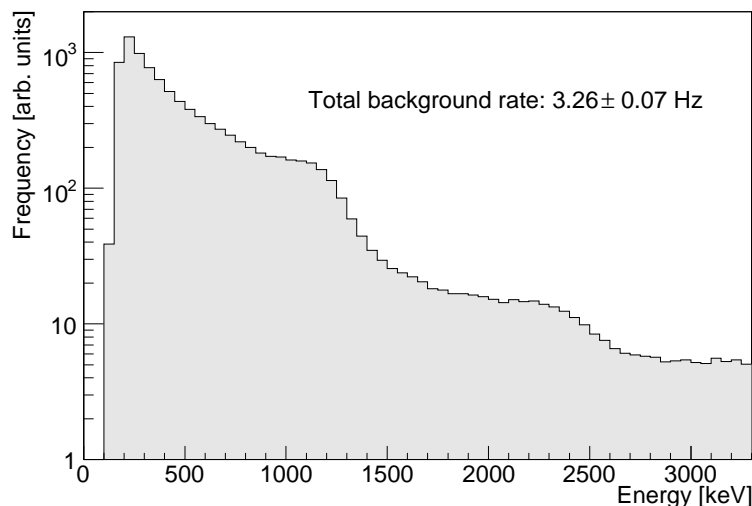


Fig. 3.41: Background energy spectrum

Chapter 4

GEANT4 Simulations

Parallel to construction, measurement and data analysis, a complete GEANT4 simulation of the experiment was developed. The simulation mainly fulfills three tasks:

- Determination of the geometrical factors (acceptance) and angular distributions.
- Understanding of the measured energy spectra.
- Determination of the energy deposit.

As has already been mentioned in Section 3.2, the angular distribution is important for the calculation of the effective transmissions of the interference filters. Furthermore, the energy deposit in the chamber is needed for the calculation of the fluorescence yield in terms of photons per deposited energy. Since the GEANT4-package is a well known and established simulation tool in high energy physics, the following sections will just give a short introduction into the structure of the simulation code, focusing on the most important features. Afterwards, the results of several simulations will be discussed.

4.1 Program Structure

The simulation of the AirLight experiment is based on the GEANT4¹ version 7.1 [3]. The GEANT4-package is a framework of C++ classes with which the user can set up an individual simulation program. The basic structure of the simulation code is always the same. The entire simulation is controlled by the so-called “G4RunManager”. The run manager class is the backbone of the simulation program. It stores all the information about the geometry and the physical interactions and manages the generation and tracking of the single particles, as is illustrated in Fig. 4.1. Information about the geometry as well as the physical interactions have to be provided by the user. This is done by several user classes which have to be derived from the corresponding base classes provided by GEANT4. The most important classes which have to be modified by the user are the “G4VUserDetectorConstruction”,

¹GEANT: GEometry ANd Tracking

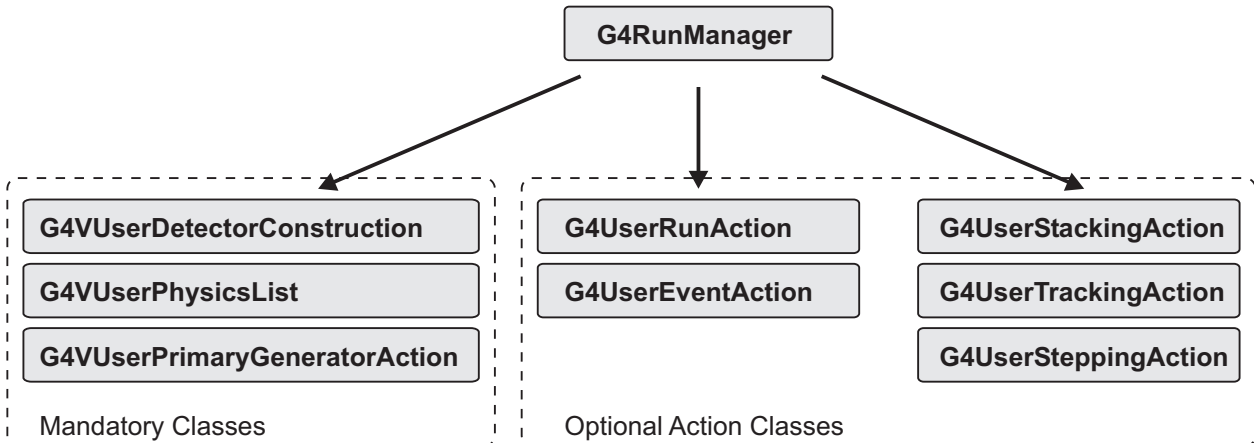


Fig. 4.1: Basic Structure of a GEANT4 based simulation program. The `G4RunManager` class stores the references to the several mandatory or optional user classes, in which the user can define the properties and the behavior of the simulation program.

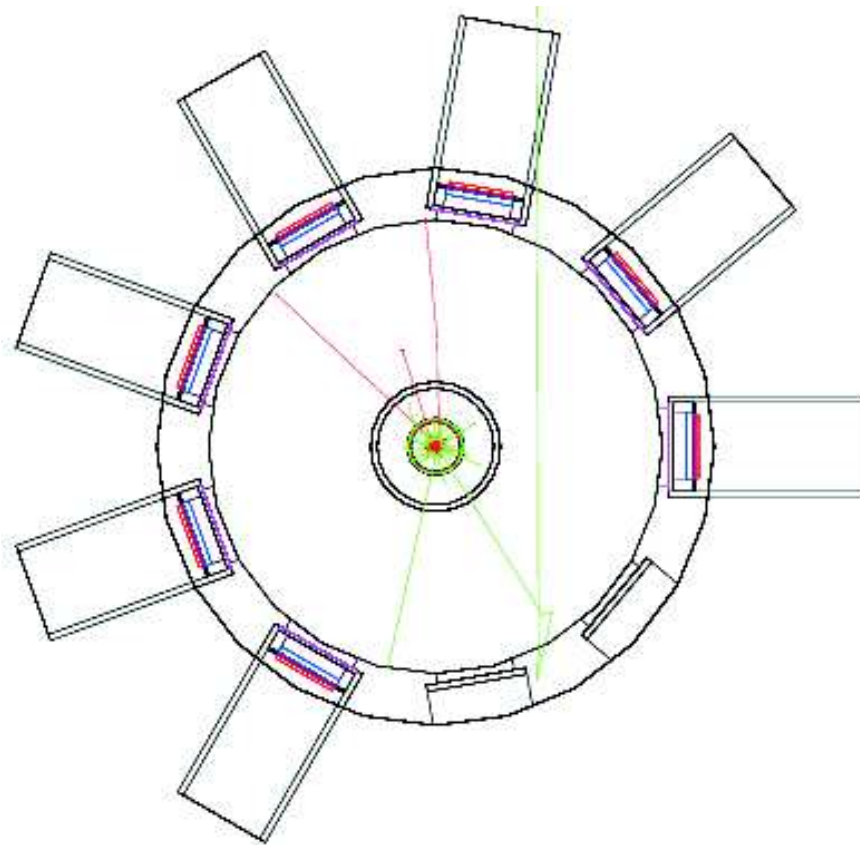
“`G4VUserPhysicsList`” and the “`G4VUserPrimaryParticleAction`” class. These mandatory classes define the detector geometry and the types of particle interactions as well as the generation of the primary particles. Furthermore, there are several optional “UserAction” classes, which are invoked before and after each particle step, track, event, or run. These classes are useful to perform arbitrary operations, as for instance particle counting, checking for boundary crossings, killing of uninteresting particles, or to store the simulation data to a file after a run has been completed.

4.1.1 Detector Construction

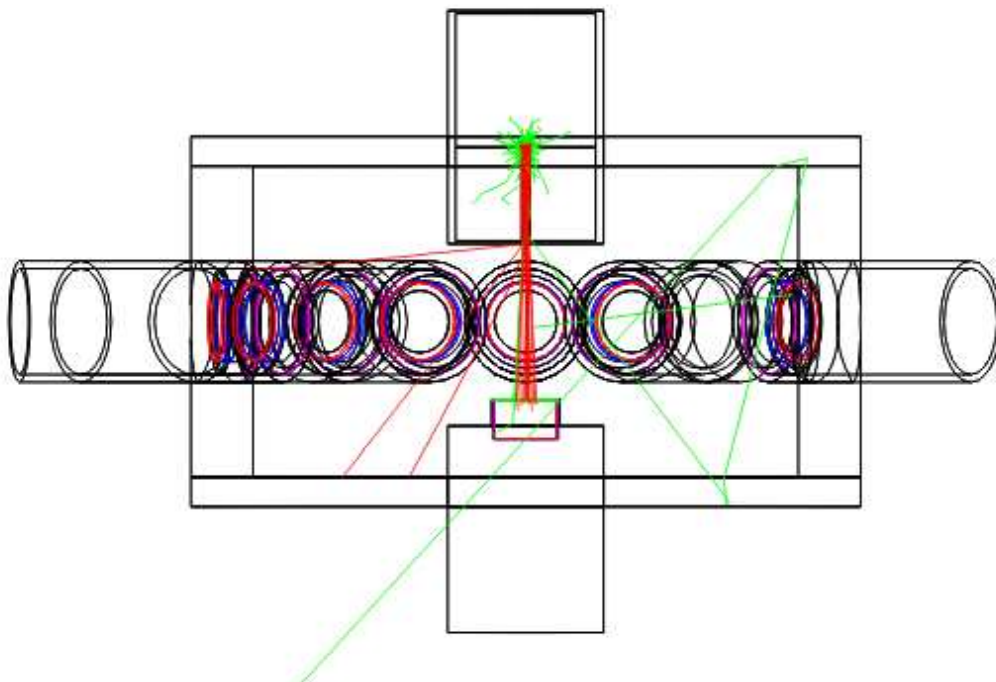
The geometry and the different materials of the detector are defined in the “DetectorConstruction” class. The modular structure of the real AirLight chamber has been adopted by the object orientated programming as well. Thus, the chamber is assembled by a cylindrical body with several apertures to mount the different photo detector-, electron detector-, and electron source modules as described in Section 3.1. These modules again are self-contained objects, which are attached at the corresponding position to the object of the chamber body. A visualization of the complete geometry is shown in Fig. 4.2. The quartz windows, filters, or the reflectivity of the photocathode can be enabled or disabled interactively, e.g. to study the effect of reflections at these surfaces.

4.1.2 Physics List

In the “PhysicsList” class, all particles used in the simulation have to be registered and the corresponding interactions have to be specified. Since in the AirLight experiment the maximum electron energy of 2.3 MeV is considerably low, just electrons, gamma particles, and optical photons together with their electromagnetic interactions have been taken into



(a) Top view of the AirLight chamber



(b) Side view of the AirLight chamber

Fig. 4.2: Detector geometry for the simulation of the AirLight chamber. The red trajectories correspond to electrons, whereas green tracks symbolize neutral particles, in this case optical photons or gamma particles.

account. More precisely, the following interaction processes have been applied for the simulation:

Electromagnetic processes:

- G4MultipleScattering
- G4LowEnergyIonisation
- G4LowEnergyBremsstrahlung
- G4ePlusAnnihilation
- G4LowEnergyPhotoElectric
- G4LowEnergyCompton
- G4LowEnergyGammaConversion
- G4LowEnergyRayleigh

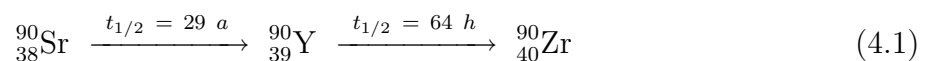
Optical processes:

- G4OpticalBoundary
- G4Scintillation (fluorescence)
- G4Cerenkov

The first four electromagnetic processes apply for electrons (and positrons), whereas the last four processes act on gamma particles. Reflections or refractions of optical photons at boundaries are treated by the G4OpticalBoundary process. Optical absorption or Rayleigh scattering can be neglected in the chamber. The scintillation as well as the Cerenkov process are the only processes inducing optical photons. However, the emission of Cerenkov photons in the nitrogen gas is negligible at these energies. GEANT4 provides several electromagnetic interaction models. In this work the low energy extension of the electromagnetic package has been used, which covers an energy range between 250 eV and 100 GeV. Some of these processes can be tuned by parameters. For instance, the step length of the first step into a new volume at boundary crossing is restricted by the so-called “facrange” parameter of the multiple scattering model. This parameter usually has a default value of 0.2, what means that the first step into a new volume is limited to 20 % of the normal step length, if there would be no boundary crossing. This restriction enables low energy electrons to scatter back into the previous volume, which otherwise could get stuck within the new volume [1]. The default value of 0.2 is a compromise between physical accuracy and computing time. Nevertheless, the backscattering fraction of electrons turned out not to be sufficiently modelled by this value to correctly reproduce the measured electron energy spectra of the AirLight experiment. Therefore the “facrange” parameter has been set to 0.01, which now yields more reliable results for the energy spectra.

4.2 Electron Energy Spectrum

As has already been mentioned in Section 3.1.1, the electrons used in the AirLight experiment are originating from the ^{90}Sr source with an activity of ~ 37 MBq. They emerge from a twofold beta decay according to the decay chain



which finally terminates in the stable isotope ${}_{40}^{90}\text{Zr}$, as is also illustrated in Fig. 4.3. Since the half live of the strontium is much larger than the half life of the yttrium, the source

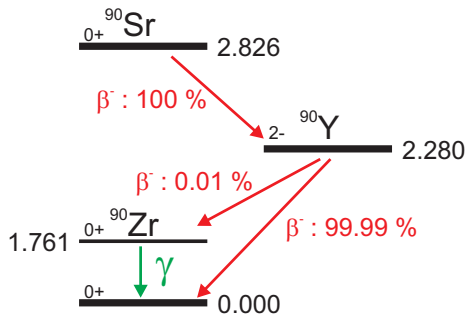


Fig. 4.3: Scheme of the ^{90}Sr decay.

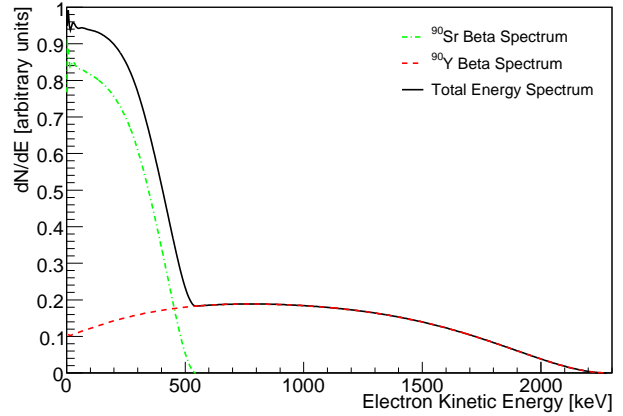


Fig. 4.4: Primary electron spectrum of the electron source as an equally weighted superposition of the ^{90}Sr and the ^{90}Y beta spectra.

can be considered in equilibrium, what means that the rate of strontium decays is equal to the decay rate of their yttrium daughters. Therefore the primary electron energy spectrum is an equally weighted superposition of the strontium and yttrium beta spectra. The end point energy of the strontium decay amounts to 546 keV, whereas the end point energy of the yttrium has a much larger value of 2280 keV. Since the experimental energy threshold is about 200 keV, most of electrons used for the measurements originate from the yttrium decay. The theoretical shape of a beta spectrum is generally given by the formula [8]

$$\frac{dN}{d\varepsilon} \propto \eta \cdot \varepsilon \cdot (\varepsilon_0 - \varepsilon)^2 \cdot F(Z, \eta) \cdot C(Z, \eta) \quad , \quad (4.2)$$

where the total energy ε and the momentum η are defined as

$$\varepsilon = \frac{E_{kin} + m_0c^2}{m_0c^2} \quad , \quad \eta = \sqrt{\varepsilon^2 - 1} \quad (4.3)$$

The first part of equation (4.2) accounts for the statistical distribution of the electron energies, as follows from the partitioning of the electron and neutrino momenta within the fermionic state space, where ε_0 denotes the end point energy of the underlying decay. This statistical factor accounts for all kind of beta decays.

In the electrostatic nuclear potential of the daughter nucleus, the emitted electrons may be slowed down or even accelerated. This effect of the nuclear potential on the primary energy distribution of the electrons is described by the so-called Fermi-function $F(Z, \eta)$. The Fermi-function depends on the momentum of the electrons and the atomic number Z of the daughter nucleus. The corresponding values are listed in tables, as for instance [7].

There are different kinds of beta decays, which are classified into allowed and several forbidden nuclear transitions. For allowed transitions the spin change between the initial and final nuclear state is $\Delta J = 0, 1$ and their parities are the same [8]. Forbidden transitions violate this rule. This leads to an additional change of the spectral shape of the beta spectrum,

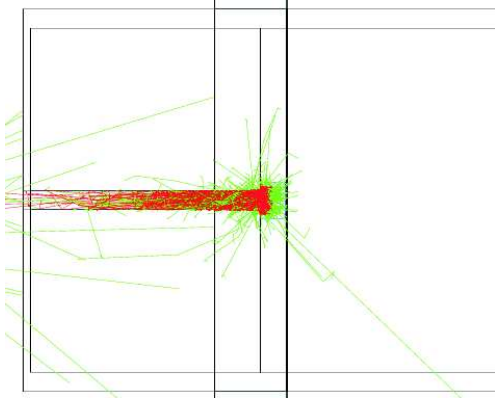


Fig. 4.5: Example for the electron scattering in the source and the collimator. Red tracks are electrons, whereas green tracks denote Bremsstrahlung photons.

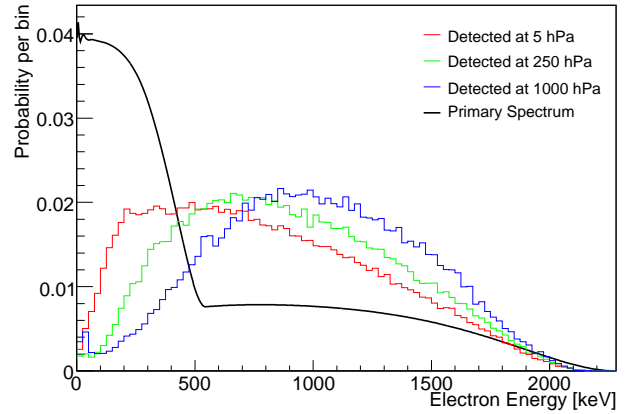


Fig. 4.6: Simulated energy distributions in the scintillator compared to the primary energy distribution in the active material of the source

which is described by the so-called shape factor $C(Z, \eta)$. For allowed transitions this factor equals to one, except for some small deviations. The decays of ^{90}Sr and ^{90}Y are both “first forbidden unique transitions”. For these kinds of transitions the shape factor is given by the relation [8, 7]

$$C(Z, \varepsilon) \propto (\varepsilon_0 - \varepsilon)^2 + \lambda_2(\eta) \cdot \eta^2 \quad , \quad (4.4)$$

where λ_2 is the so-called Coulomb-function, which usually depends on the momentum η . For strontium and yttrium decays it has a value of $\lambda_2 \approx 0.91$, however, for the calculation of the electron energy spectrum tabulated values from [7] have been used.

Since a strontium decay is directly followed by a decay of its yttrium daughter, the final electron energy spectrum is the equally weighted sum of the strontium and the yttrium beta spectrum. The resulting total energy spectrum, which has been used for the generation of the primary electrons in the simulations, is shown in Fig. 4.4.

4.2.1 Detected Energy Spectrum

According to the primary energy distribution derived above, the electrons are homogeneously generated in the volume of the active material, which is situated in the source case shown in Fig. 3.4. Since no precise information of the manufacturer could be obtained, the active material has been assumed to be of porous ceramics (Al_2O_3) with a density of 0.55 g/cm^3 . The density of the active material has been tuned in a way to obtain the best agreement with the measured energy spectra. Only a small fraction of electrons is able to pass the lead collimator without being stopped or scattered at the collimator walls. Therefore it is absolutely essential to generate the electrons isotropically in all directions within the active material, since the electron backscattering has a great influence on the final energy distribution. In this context it was also necessary to choose the smaller value of 0.01 for the “facrange” parameter described in Section 4.1.2. Apart from the surrounding materials, the

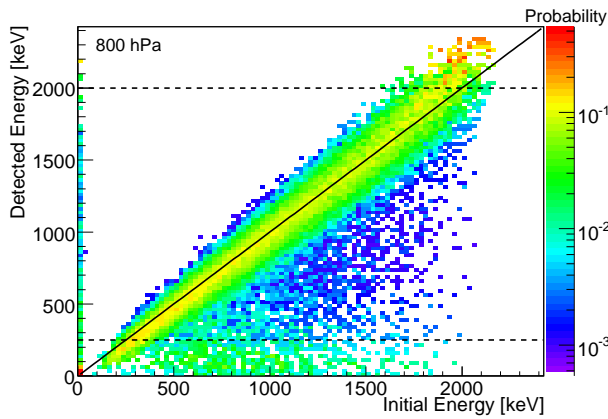


Fig. 4.7: Migration matrix, containing the probabilities for an electron with initial energy E_i to be detected with an final energy E_f .

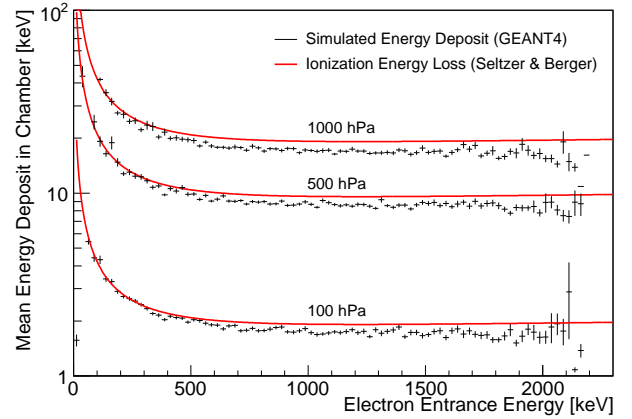
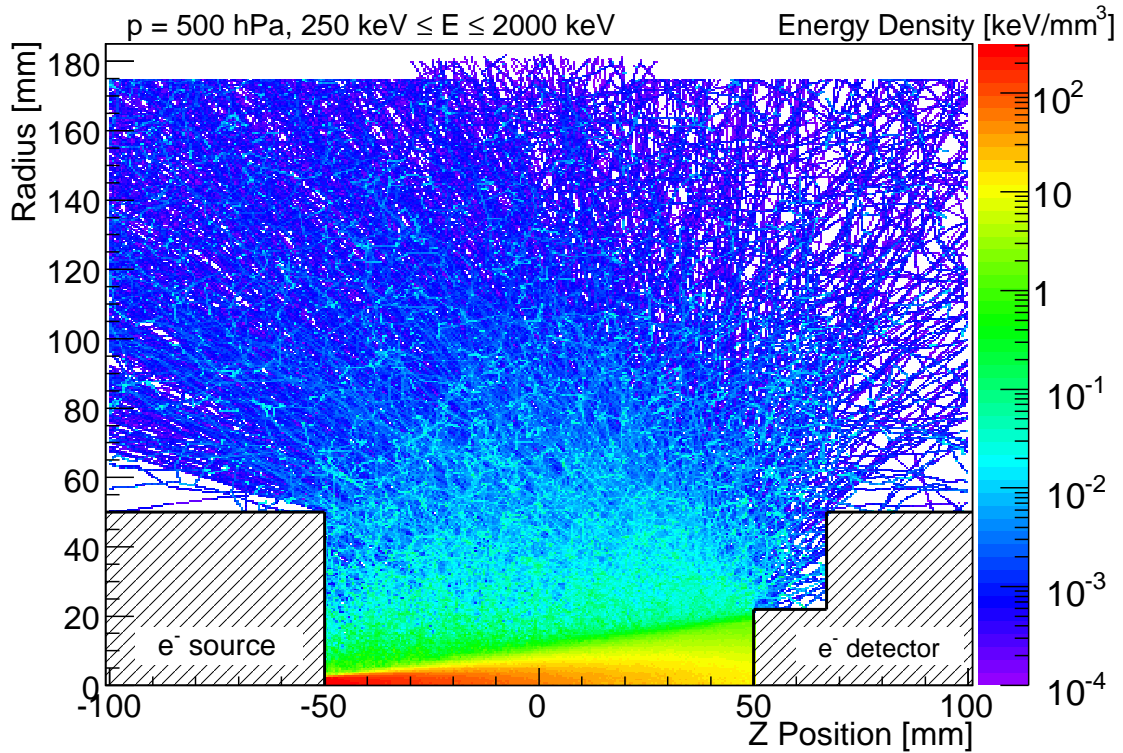


Fig. 4.8: Simulated energy deposit profiles over the entrance energy, compared to Seltzer and Berger parametrization.

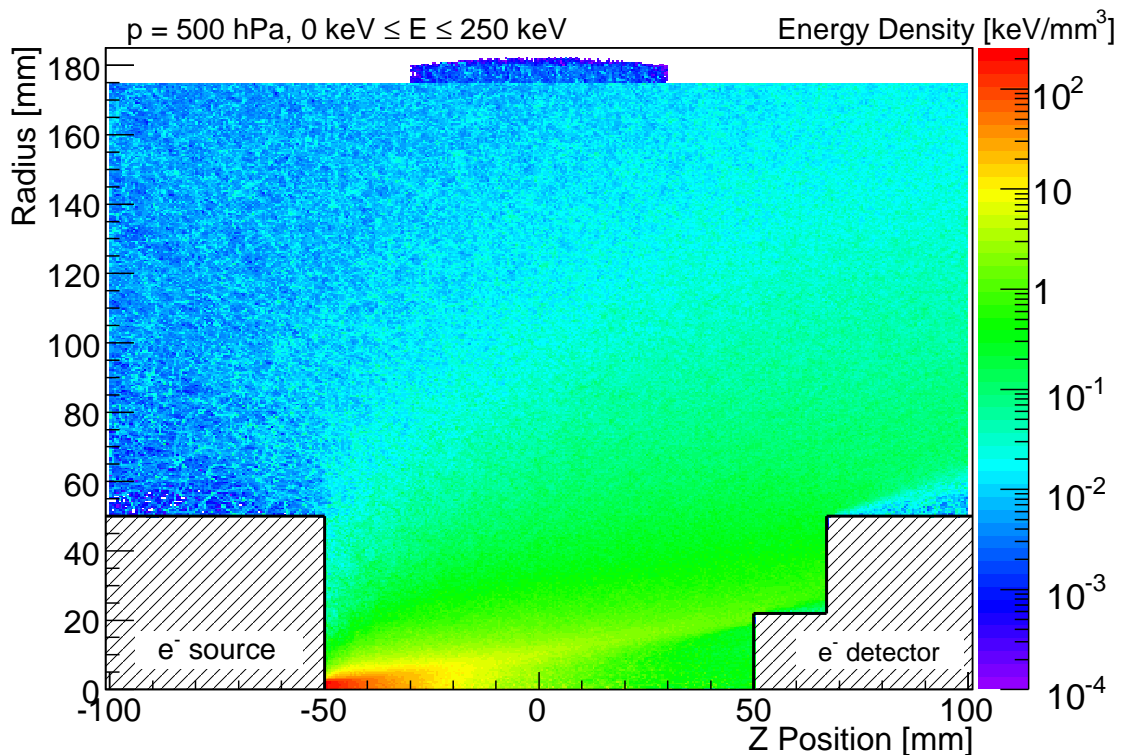
measured electron energy distribution is also affected by energy losses and multiple scattering in the gas within the chamber. Therefore the final energy distribution is changing its shape according to the gas pressure. Examples for the resulting energy distributions are shown in Fig. 4.6 for various pressures. Since the experimental energy threshold is at around 200 keV, only electrons with energies larger than 150 keV have been generated in the simulations to save computing time. The energy of the electrons is determined in the volume of the scintillator as a sum over the single ionization energy losses at each electron step. This way, the simulated energy spectra correctly account for electrons, which are not completely stopped in the scintillator or loose their energy by radiative processes. In the simulation, the scintillator has a perfect energy resolution. To be compared with measurements, the simulated energy spectra need to be smeared out with the corresponding energy resolution of the measured data. In order to obtain the initial energy distributions of the electrons entering the gas volume, the simulation provides a migration matrix, as is shown in red Fig. 4.7, to transform the measured energy distributions to the initial ones. The migration matrix contains the probabilities of an electron emerging from the initial energy bin i to be detected in the final energy bin f . This way also secondary electrons are treated correctly.

4.3 Energy Deposit in Chamber

The energy deposit in the gas volume of the AirLight chamber is a key quantity for the determination of the fluorescence yield. In small volumes, as it is the case for the AirLight chamber, the energy deposit is not necessarily equal to the ionization energy loss, as follows from the Bethe-Bloch formula, since secondary delta electrons may carry away part of the energy. Furthermore, secondary electrons emerging from collisions of the primary electrons with the collimator walls, or electrons repulsing out of the scintillator, may even increase the



(a) Energy densities for detected electron energies between 250 keV and 2000 keV



(b) Energy densities for detected electron energies lower than 250 keV. These electrons are either not detected or not considered in the data analysis.

Fig. 4.9: Spatial distributions of the deposited energy density inside the AirLight chamber at a pressure of 500 hPa.

energy deposit. Therefore the energy deposit in the gas volume is expected to deviate from the continuous ionization energy loss, as is given by the Bethe-Bloch formula. Energy losses due to Bremsstrahlung in the gas do not play a role at these energies.

To figure out such effects, the deposited energy in the whole chamber volume was determined as the sum over the locally deposited continuous energy loss of each electron step in an event, regardless whether the electron was the primary or a secondary electron. As can be seen in Fig. 4.8, the energy deposit for entrance energies larger than 300 keV turned out to be 8 - 10 % smaller than the ionization energy losses given by the Seltzer and Berger description [41]. For smaller energies it seems to follow the continuous energy losses.

The energy deposit profiles shown in Fig. 4.8 describe the mean energy deposit in the gas volume per detected electron. The emission of fluorescence light is assumed to be proportional to the deposited energy in the gas, and thus the spatial distribution of the total energy deposit corresponds to the points of origin of the fluorescence photons. Therefore the simulation additionally is providing four dimensional energy deposit maps. One dimension is the detected energy in the scintillator and the other two dimensions are the z position along the chamber axis and the radial distance to the axis. Finally, the fourth dimension corresponds to the deposited energy per mm^3 . In this way the deposited energy density can be displayed for different energy ranges of the detected electrons, as it is done in Fig. 4.9 for a nitrogen pressure of 500 hPa. Fig. 4.9 (a) shows the energy density distributions of electrons, which have been detected with energies between 250 keV and 2000 keV. Apparently, most of the energy is deposited around the chamber axis. However, some of the secondary electrons are scattered away from the axis and deposit their energy somewhere in the chamber volume. If such electrons are absorbed by the chamber walls, their energy gets lost, what leads to a smaller amount of deposited energy in the gas than one would expect from the Bethe-Bloch formula. The energy deposit density for electrons with energies below 250 keV is illustrated in Fig. 4.9 (b). These energies correspond to electrons, which in reality are either not detected or not considered in the data analysis. As can be seen, the electrons are much more scattered away from the chamber axis and fill the complete chamber volume. Most of their energy gets lost directly after entering the chamber volume. It turned out that the energy deposit distributions for energies between 250 keV and 2000 keV are rather similar over the whole pressure range. The influence on the angular distributions of the fluorescence photons is discussed in the following section.

4.4 Photon Angular Distribution

As has already been mentioned in Section 3.2, angular distribution of the photons on the photocathode is important for the calculation of the effective transmissions of the interference filters. Furthermore, the acceptance of the photon detectors needs to be determined for the reconstruction of the total number of photons in the chamber. In order to figure out these quantities, a detailed simulation study has been performed. Assuming the number of emitted photons to be proportional to the local energy deposit, they have been isotropically generated in the whole gas volume according to the energy deposit maps from the previous studies,

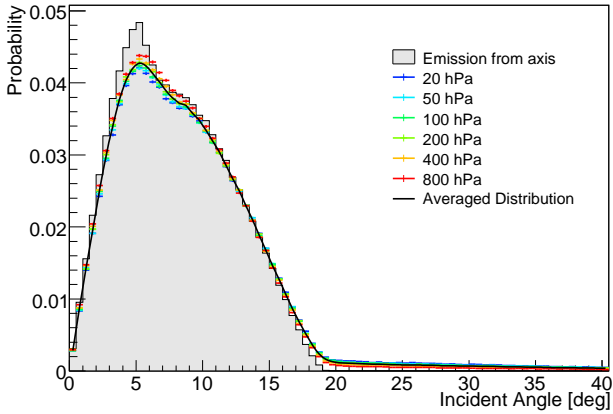


Fig. 4.10: Simulated photon angular distributions on the photocathode of a photon detector for various pressures. The gray shaded histogram represents the idealized angular distribution of photons originating from the chamber axis.

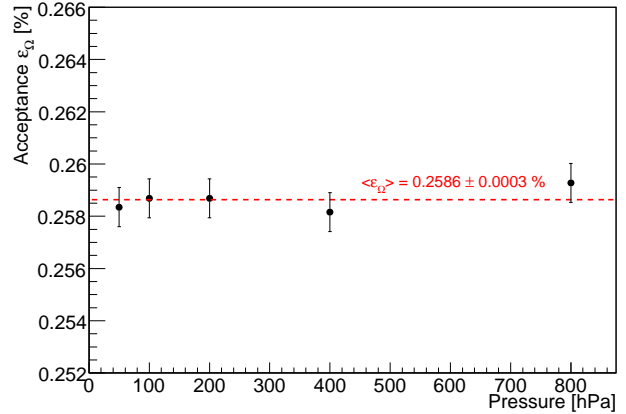


Fig. 4.11: Pressure dependence of the acceptance ε_{Ω} of a single photon detector.

shown in Fig. 4.9. This method saves a lot of computing time, since the time consuming end-to-end simulation of the electrons just has to be done once for each pressure value. Furthermore, it allows to cut on the energy of the detected electrons, to generate the optical photons just for energies, which are considered in the data analysis. Several simulations have been done over the whole pressure range for energies of the detected electrons ranging from 250 keV to 2000 keV. The resulting angular distributions are shown in Fig. 4.10. As can be seen, the shape of the angular distributions turned out to be rather stable over the whole pressure range. Therefore an averaged angular distribution has been derived for the calculation of the effective filter transmittances, which is represented by the solid black line in Fig. 4.10. The gray shaded histogram represents the angular distribution for an idealized, one-dimensional electron beam along the chamber axis. Compared to this distribution, the realistic distributions show a tail above 20° , which originates from photons emerging from off-axis regions due to the secondary production and the multiple scattering of the electrons. The tail ends at roughly 64° and the contribution of photons with angles larger than 20° is less than 5 %. Parallel to the angular distributions, the acceptance ε_{Ω} has been determined as the ratio of the number of generated photons in the whole gas volume to the number of photons reaching the photocathode of a single photon detector. In this case as well, the energy of the detected electrons has been restricted to an energy interval between 250 keV and 2000 keV. As can be seen in Fig. 4.11, the acceptance appears to be very stable over the whole pressure range with a mean value of $\langle \varepsilon_{\Omega} \rangle = 0.2586 \pm 0.0003 \%$. With the knowledge of the ε_{Ω} and the angular distributions of the photons, the analysis of the fluorescence measurements can be done as will be explained in the following chapter.

Chapter 5

Measurement and Data Analysis

This chapter deals with the analysis of the fluorescence measurements performed with the AirLight chamber. In previous works, the single nitrogen transitions often have been analyzed apart from each other, even if there are obvious relationships between them. This may cause inconsistencies in the results. For instance, the reference pressures p' , which will be introduced later on, tend to adopt different values, depending whether they are determined using the intensities or the lifetimes of the associated transitions. Furthermore, the lifetimes and quenching constants of transitions emerging from the same vibrational state are identical and should not produce different values for each transition. Since in this work the measurement is done with narrow band filters, it happens that some of the transitions are overlapping within the same filter range. To make quantitative statements about the single transitions, it is necessary to separate the different contributions from each other. For this purpose, a sophisticated χ^2 minimization, which accounts for all relations between the different transitions, has been developed and applied to the complete dataset. This naturally ensures the consistency of the results.

5.1 Datasets Used

The data used for the following analysis were taken between August and November 2005. Originally, the experiment was designed for seven individual photon channels at different wavelength ranges. Unfortunately, the PMT of channel 6 broke down during the measurements. This channel was supposed to measure the 1N(0,1) transition at 427.81 nm, which fortunately plays no role for air shower measurements, since it usually does not match with the wavelength range of the fluorescence telescopes. To avoid an interruption of the ongoing measurements, the decision was taken not to repair this channel. Therefore only the remaining six channels are considered in the following analysis.

Several series of measurements have been made for pure nitrogen (N₂ 5.0), artificial dry air (78.1 % Vol. N₂, 20.9 % Vol. O₂, 1.0 % Vol. Ar), and a mixture of nitrogen and oxygen (90.0 % Vol. N₂, 10.0 % Vol. O₂). Additionally, the effect of water vapor has been studied at various mixtures of water vapor with nitrogen or air. Each series of measurements contains

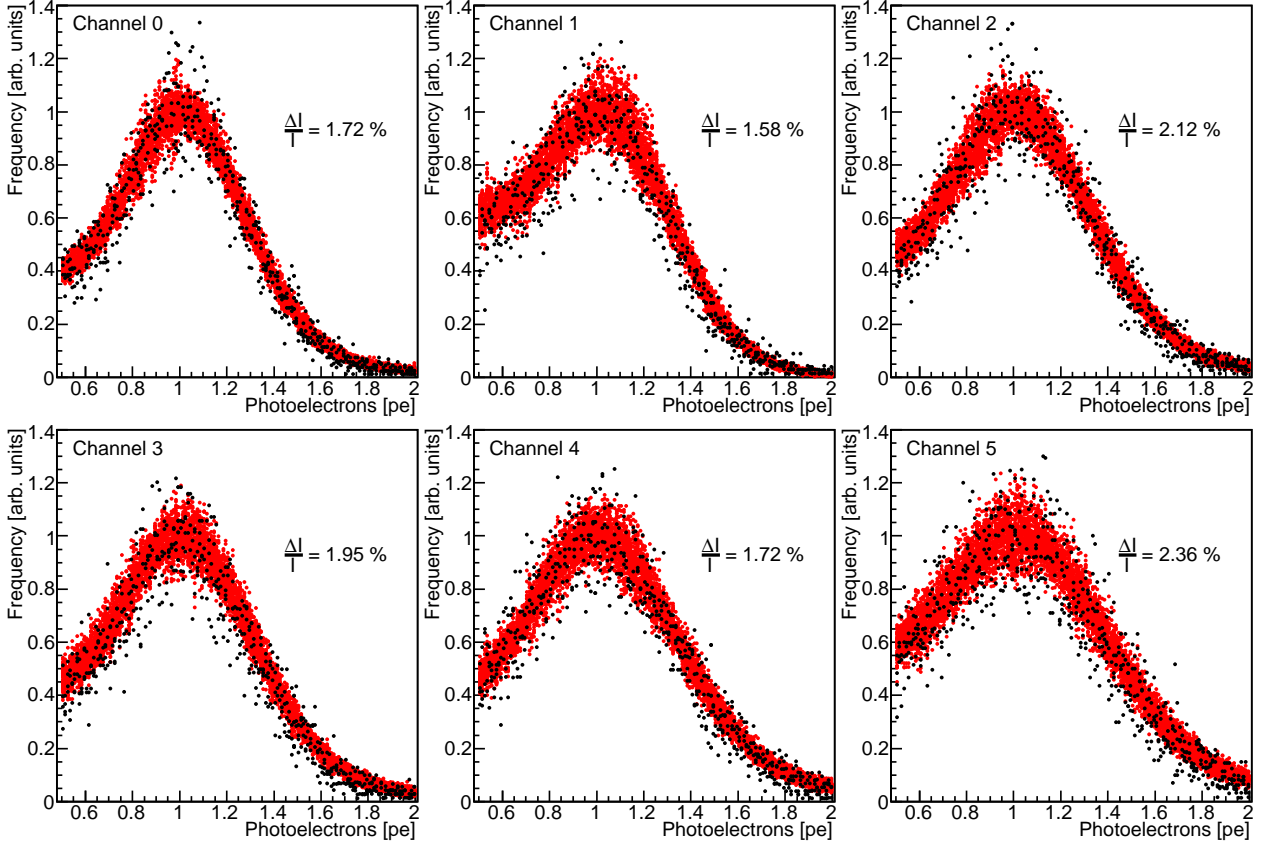


Fig. 5.1: Overlaid single photoelectron distributions of all measurements normalized to one at 1 pe. Distributions of the relative calibration measurements from Section 3.5.4 are overlaid in black. The fluctuations $\Delta I/I$ of the red integrals are in the order of 2 % and are a measure for the stability of the photoelectron distributions.

between 12 and 18 runs at different pressures ranging from 2 hPa to 990 hPa. The measurements have been done at ambient temperatures between 15 °C and 23 °C, depending on the weather conditions outside the laboratory. The required number of coincidences per run amounts to one million events. Depending on the gas and the pressure, a measurement lasted between 12 and 30 hours. Before each series of measurements, calibration measurements have been performed, as is explained in Section 3.5.

From the calibrated data of a single run distributions of the difference times between the photon and the electron triggers, as well as the single photoelectron spectra of each channel, can be extracted. Furthermore, a free electron energy spectrum in common for all channels is provided by the data. Absolute values of the free and coincident count rates of each channel are given by the scaler values and are important to figure out dead time of the different channels. To minimize background and to focus the analysis just on regions with sufficient statistics, cuts have been applied to the energy and the photoelectron numbers. The maximum usable energy range was chosen to be between 250 keV and 2000 keV. For all studies, the photoelectron number has been limited to values between 0.5 pe and 2 pe. As has already

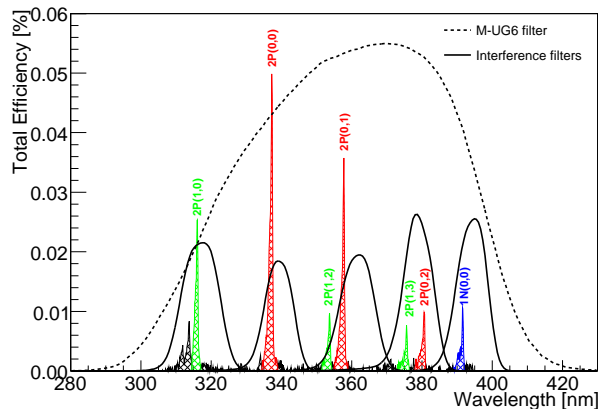


Fig. 5.2: The most intensive transitions in the nitrogen spectrum [44] emerge from just three electronic-vibrational states, marked by the different colors. The detection efficiencies of the different filter channels are superimposed.

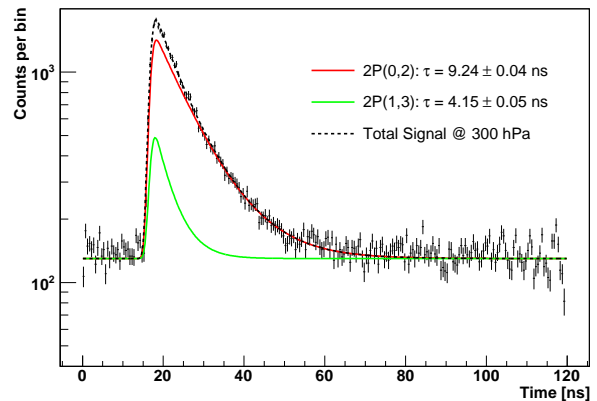


Fig. 5.3: Example of a time spectrum in channel 3 equipped with filter “380a”. The total signal appears to be the superposition of the 2P(0,2) and the 2P(1,3) transition.

been mentioned previously, the stability of the photoelectron distributions in the photon detectors is very important for the correct application of the calibration constants, which have been determined within the same photoelectron range. To demonstrate their stability, the photoelectron distributions of all measurements used in this analysis are overlaid in Fig. 5.1. The distributions have been normalized to one at 1 pe. The corresponding distributions of the calibration runs are overlaid in black. The integrals over these distributions correspond to the number of events surviving the cut on the photoelectron number. The fluctuations of these integrals are in the order of 2 % and can be used to estimate the systematic uncertainty connected with the photoelectron cut.

5.2 Analysis Procedure

A single measurement with the current filter batch contains information of at least 8 different nitrogen transition bands. Apart from the 2P(0,0), transition all the other transitions are mixed together in the other filter channels, as can be seen in Fig. 5.2. Transitions coming from the same electronic-vibrational state are drawn with the same color. Thus, the main task of the analysis procedure is to separate the different contributions within the filter channels. One possibility to do this is by means of their different lifetimes. At least for high pressures, the lifetimes should differ due to the different influence of collisional quenching. Therefore the separation can be done in principle by fitting a multi-exponential function to the time spectra, as is shown in Fig. 5.3. In case of a single channel with more than one, for instance n , contributions this does not help much because of the lack of knowledge about the other $n - 1$ contributions. This problem is similar to the attempt to solve an equation system with

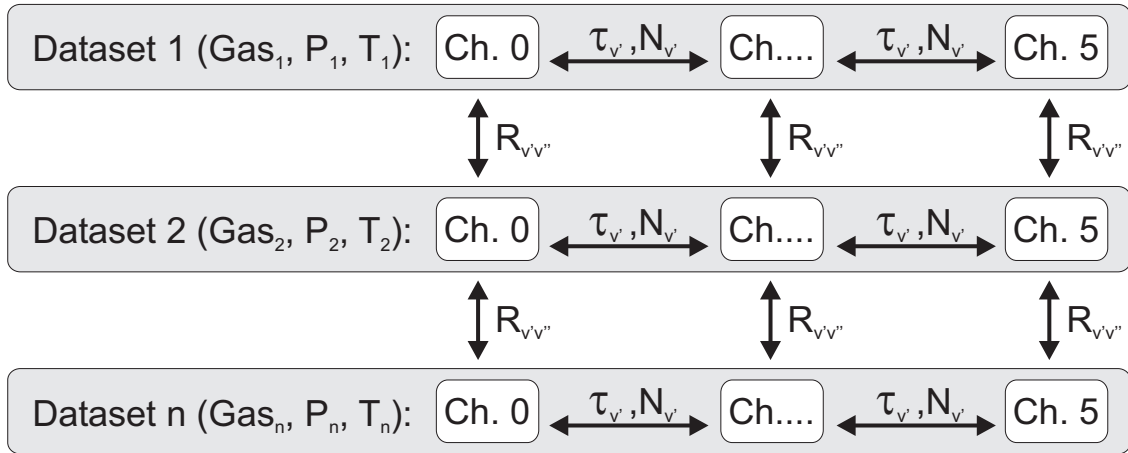


Fig. 5.4: Sketch of the simultaneous minimization of all datasets. Different channels in a dataset are connected through the lifetimes $\tau_{v'}$ and the intensities $N_{v'}$ of the main contributions. Connections between the datasets are given by the intensity ratios $R_{v'v''}$.

n parameters with just one equation. Therefore the other channels have to be considered as well. Since this is a simultaneous measurement, the intensities and lifetimes of the transitions in the different channels are correlated to each other. The single $2P(0,0)$ transition of the 337 nm band in channel 4 happens to be of great importance for this purpose. In principle there are slight contributions of other bands to this channel but, because of the very high intensity of the $2P(0,0)$ transition, they are assumed to be negligible. With the help of the $2P(0,0)$ transition, the lifetimes of the $2P(0, v'' = 1, 2, \dots)$ contributions in the other channels are immediately determined.

Besides the correlation of the lifetimes, there is an additional relation between the intensities of transitions emerging from the same electronic-vibrational state. According to equation (2.31), their intensity ratios are given by the ratio of their Einstein-coefficients. Since these ratios are constant, they have to be the same for all measurements, regardless of the composition or the pressure of the nitrogen-mixture.

With the aid of these general relations, it is now possible to separate for transitions coming from the same electronic-vibrational state the different contributions from each other. The relation between the lifetimes connects the different channels within one measurement (dataset) “horizontally” with each other, whereas different measurements, regardless of the gas composition and the pressure, are connected “vertically” through the constraint of the constant intensity ratios, as is shown in Fig. 5.4. This is done technically by a combined minimization of all datasets, where the following parameters are varied or fixed depending on the purpose of the underlying analysis:

- Intensities of the main contribution of each electronic-vibrational band system.
- Intensity ratios $R_{S(v',v'')}$ of transitions within the same electronic-vibrational band system.

- Lifetimes $\tau_{S(v')}$ of the contributing electronic vibrational levels.

This is the most general approach for the fitting procedure and ensures consistent results for all contributing vibrational bands. It can still be specialized, if additional assumptions about the excitation or the quenching are considered within the fit, e.g. the linear pressure dependence of the reciprocal lifetimes or the assumed proportionality of the intensities to the deposited energy. All these additional relations lead to further vertical connections between the different datasets in Fig. 5.4. On the other hand, one has to be aware of forcing the data to the model, if the minimization function is constraint by too many assumptions which also may be wrong.

5.2.1 Time Distributions

One of the main ingredients for the general minimization function, which will be introduced in the subsequent section, is the functional form of the measured time distribution of a single transition. According to the decay law (2.27), the number of emitted photons in the time interval $[t, t + dt]$ for $t \geq 0$, is given by a simple exponential function

$$\frac{dN}{dt} = \frac{N}{\tau} \cdot e^{-\frac{t-t_0}{\tau}} \quad , \quad t > t_0 \quad , \quad (5.1)$$

where t_0 is an arbitrary choice for the time origin, indicating the moment of excitation. This function has to be convoluted with the response function $R(t)$ of the detecting system to take into account its limited time resolution:

$$f(t) = \frac{dN}{dt}(t) \otimes R(t) = \int_0^\infty \frac{dN}{dt'}(t') \cdot R(t-t') dt' \quad . \quad (5.2)$$

Since independent sources contribute to the overall time resolution, as e.g. the discriminators, gate generators and the TDC, the response function is assumed to be a normalized Gaussian function, where the standard deviation σ is a measure for the time resolution of the detector. With this approach equation (5.2) reads:

$$f(t) = \frac{N}{\tau} \frac{1}{\sqrt{2\pi}\sigma} \cdot \int_{t_0}^\infty e^{-\frac{t'-t_0}{\tau}} \cdot e^{-\frac{(t-t')^2}{2\sigma^2}} dt' \quad (5.3)$$

This expression transforms into

$$f(t) = \frac{N}{\tau} \frac{1}{\sqrt{2\pi}\sigma} \cdot e^{-\frac{t_0}{\tau}} \cdot e^{-\frac{t^2}{2\sigma^2}} \cdot \int_{t_0}^\infty e^{-\frac{-2(t-\frac{\sigma^2}{\tau})t'-t'^2}{2\sigma^2}} dt' \quad (5.4)$$

and the exponent of the integrand can be quadratically extended:

$$\begin{aligned}
f(t) &= \frac{N}{\tau} \frac{1}{\sqrt{2\pi}\sigma} \cdot e^{\frac{t_0}{\tau}} \cdot e^{-\frac{t^2}{2\sigma^2}} \cdot \int_{t_0}^{\infty} e^{-\frac{(t-\frac{\sigma^2}{\tau})^2 - 2(t-\frac{\sigma^2}{\tau})t' - t'^2 - (t-\frac{\sigma^2}{\tau})^2}{2\sigma^2}} dt' \\
&= \frac{N}{\tau} \frac{1}{\sqrt{2\pi}\sigma} \cdot e^{\frac{t_0}{\tau}} \cdot e^{-\frac{t^2}{2\sigma^2}} \cdot e^{\frac{(t-\frac{\sigma^2}{\tau})^2}{2\sigma^2}} \cdot \int_{t_0}^{\infty} e^{-\frac{[(t-\frac{\sigma^2}{\tau})-t']^2}{2\sigma^2}} dt' \\
&= \frac{N}{\tau} \cdot e^{-\frac{t-t_0}{\tau}} \cdot e^{\frac{\sigma^2}{2\tau^2}} \cdot \underbrace{\frac{1}{\sqrt{2\pi}\sigma} \int_{t_0}^{\infty} e^{-\frac{[(t-\frac{\sigma^2}{\tau})-t']^2}{2\sigma^2}} dt'}_{\text{Integrated Gauss function}} \quad (5.5)
\end{aligned}$$

The last term of the latter equation is an integrated Gaussian function with mean value $\mu = t - \frac{\sigma^2}{\tau}$ and can be evaluated by means of the complementary error function “erfc” [38]:

$$\text{erfc}(x) = \frac{2}{\sqrt{\pi}} \cdot \int_x^{\infty} e^{-u^2} du \quad , \quad (5.6)$$

in which $\text{erfc}(-\infty) = 2$, $\text{erfc}(0) = 1$ and $\text{erfc}(\infty) = 0$. Thus, the solution for the measured time distribution of a single transition becomes

$$f(t) = \frac{1}{2} \frac{N}{\tau} \cdot e^{-\frac{t-t_0}{\tau}} \cdot e^{\frac{\sigma^2}{2\tau^2}} \cdot \text{erfc} \left(\frac{t_0 - t - \frac{\sigma^2}{\tau}}{\sqrt{2}\sigma} \right) \equiv f(t, t_0, N, \tau, \sigma) \quad (5.7)$$

where N equals to the integral of this function from $t = -\infty$ to $t = +\infty$ and thus corresponds to the total number of emitted photons by an excited state with lifetime τ . The time resolution of the detector system in terms of one standard deviation is given by σ . As expected, for $\sigma \rightarrow 0$ and $t > t_0$, equation (5.7) becomes the original exponential function (5.1) again. Instead of this differential expression, the minimization procedure makes use of the integrated form of equation (5.7), since the shape of the time spectra, especially for very small lifetimes τ , cannot always be considered to be linear over the bin width. The integral of this function has been obtained by partial integration of equation (5.3) and rearrangements similar to those from above. The resulting function thus turns out to be

$$F(t_1, t_2, t_0, N, \tau, \sigma) = \tau \cdot [f(t_1) - f(t_2)] + \frac{N}{2} \cdot \left[\text{erfc} \left(\frac{t_1 - t_0}{\sqrt{2}\sigma} \right) - \text{erfc} \left(\frac{t_2 - t_0}{\sqrt{2}\sigma} \right) \right] \quad , \quad (5.8)$$

where t_1 and t_2 are the limits of the integration interval. For $t_1 \rightarrow -\infty$ and $t_2 \rightarrow +\infty$ equation (5.8) just results in the total number N of emitted photons.

5.2.2 General Minimization Function

As has already been pointed out at the beginning of this section, the determination of the different parameters of interest is done by simultaneous fits of all measurements. Practically,

this can be done in terms of a χ^2 -minimization. The general form of the minimization function is given by [11]:

$$\chi^2 = \sum_i \left(\frac{y_i - f(x_i, \mathbf{a})}{\sigma_{y_i}} \right)^2 \quad (5.9)$$

where y_i is a single data point at x_i with (statistical) error σ_{y_i} and $f(x_i, \mathbf{a})$ is the model expectation \hat{y}_i at x_i . The parameter vector \mathbf{a} contains all the parameters on which the model function depends. If the deviations between the model and the data were always smaller than the error on the data points $|y_i - f(x_i, \mathbf{a})| < \sigma_{y_i}$, then χ^2 would be smaller than the number of data points. The smaller the χ^2 the better the model fits to the data. Therefore the optimal set of parameters \mathbf{a} can be found by minimizing χ^2 over the whole parameter space of \mathbf{a} . Thus, an equation system of the form $\frac{\partial \chi^2}{\partial a_k} = 0$ for every parameter a_k has to be solved. For linear problems this can be done analytically, but for more complicated ones it is typically done numerically. In this work the MINUIT minimization program [26] was used, which is included in the ROOT framework [13].

According to this method, the minimization function for the following analysis can be constructed as a sum over all datasets d , photon detector channels c , and time bins b of these channels:

$$\chi^2 = \sum_d \sum_c \sum_b \left[\frac{y_{dcb} - (N_{dc} + B_{dcb} + S_{dcb})}{\sigma_{y_{dcb}}} \right]^2 \quad (5.10)$$

In this expression, y_{dcb} denotes the bin content with statistical Poissonian error $\sigma_{y_{dcb}} = \sqrt{y_{dcb}}$ and N_{dc} corresponds to the constant noise per bin of channel c . Furthermore, the background and the fluorescence signal of bin b are given by B_{dcb} and S_{dcb} respectively. The fluorescence signal S_{dcb} again is a sum over all transitions contributing to this channel:

$$S_{dcb} = \varepsilon_{DAQ}^{dc} \cdot \sum_s \sum_{v''} \varepsilon_{det}^{csv''} \cdot F(t_1, t_2, t_0^{dc}, \underbrace{R_{sv''} \cdot N_{ds}}_{N_{dsv''}}, \tau_{ds}, \sigma_{dc}) \quad (5.11)$$

The summation is done over all transition systems s and final vibrational levels v'' . A transition system consists of all transitions emerging from the same vibrational level v' within a certain band system, e.g. 2P(0, v''), 2P(1, v'') or 1N(0, v''). The signal per bin of a single transition is given by $F(t_1, t_2, t_0^{dc}, N_{dsv''}, \tau_{ds}, \sigma_{dc})$, where t_0^{dc} and σ_{dc} correspond to the time origin and the time resolution of the underlying channel, and τ_{ds} denotes the lifetime of the transition system. The total number of emitted photons into this band corresponds to $N_{dsv''} = R_{sv''} \cdot N_{ds}$, where $R_{sv''}$ is the intensity ratio of the transition (s, v'') with respect to the main transition of the underlying transition system s . The function $F(t_1, t_2, \dots)$ is the integral (5.8) of equation (5.7) in the time interval $[t_1, t_2]$, where $t_1 = t_{dcb} - 0.5\Delta t$ and $t_2 = t_1 + \Delta t$ with respect to the time t_{dcb} at the bin center. This way, the limited bin width Δt of typically 0.5 ns is correctly taken into account. This may play a role for narrow signal peaks at very short lifetimes, where signal variations over the bin width deviate from a linear behavior. To obtain the number of detected photons, the total intensity still needs to be multiplied by the effective detection efficiency $\varepsilon_{det}^{csv''}$ for the transition (s, v'') in channel c ,

which will be calculated in Section 5.2.4. Finally, the dead time of the experiment is taken into account by a subsequent multiplication with the data acquisition efficiency ε_{DAQ}^{dc} .

The background in each channel has been parameterized in Section 3.6.1 and is assumed to have a Gaussian time distribution. As it has been done for the signal, the differential background distribution (3.34) has to be integrated over the bin width $\Delta t_{dcb} = t_2 - t_1$. This can be achieved by means of the erfc-function (5.6) and thus the background contribution to a bin becomes

$$B_{dcb} = \frac{1}{2} \cdot \varepsilon_{DAQ}^{dc} \cdot R_B^c \cdot \left[\operatorname{erfc} \left(\frac{t_1 - t_B^{dc}}{\sqrt{2}\sigma_B^c} \right) - \operatorname{erfc} \left(\frac{t_2 - t_B^{dc}}{\sqrt{2}\sigma_B^c} \right) \right] \cdot \int_E \varepsilon_B^0(E) \cdot \frac{dN_e}{dE} dE \quad (5.12)$$

In this case, R_B^c stands for the intensity ratio of the background in channel c with respect to channel 0, whereas t_B^{dc} and σ_B^c denote the mean time and the width of the background peak. Also the background has to be multiplied with the data acquisition efficiency ε_{DAQ}^{dc} to take into account the dead time of the experiment. The last integral over the electron energies is in common for the complete dataset d and is evaluated before the minimization is started.

5.2.3 Data Acquisition Efficiency

The data acquisition efficiency ε_{DAQ} is a measure for the dead time of the measurements and denotes the fraction of the acquired number of events to the total number of detected events. At 100 % acquisition efficiency all the detected events would also have been captured by the data acquisition. The data acquisition efficiency of a certain channel can be calculated as the fraction of the number of sampled coincidences n_{coin} , in the absence of any cut, to the total number of coincidences N_{coin} given by the corresponding scaler values:

$$\varepsilon_{DAQ} = \frac{n_{coin}}{N_{coin}} \quad , \quad \sigma_{\varepsilon_{DAQ}} = \sqrt{\frac{(1 - \varepsilon_{DAQ}) \cdot \varepsilon_{DAQ}}{N_{coin}}} \quad (5.13)$$

Since a measurement is subdivided into many independent cycles of a 10 minutes duration, as explained in Section 3.4.2, the data acquisition efficiency is evaluated individually for every cycle and channel, as can be seen in Fig. 5.5. In this way the binomial character of the errors is directly obtained from the fluctuations of the data points. The relative error of the mean data acquisition efficiency amounts to ~ 0.2 %. The data acquisition efficiency depends opposite to the total coincidence rate, since the data acquisition system has just a limited acquisition capability. For small coincidence rates ε_{DAQ} approaches 100 %, whereas it goes to zero for infinitely high rates. Typical values during the fluorescence measurements were ranging from 90 % to 97 %, depending on the air mixture and the pressure, as is shown in Fig. 5.6. For pure nitrogen the signal rates typically are the highest and thus ε_{DAQ} has the smallest value with respect to the other gas mixtures. Furthermore, ε_{DAQ} is increasing for very low pressures and again for high pressures. At very low pressures the signal rates are small because of the small amount of nitrogen inside the chamber. At high pressures one would naively expect a steady decrease of ε_{DAQ} , but due to the stronger influence of

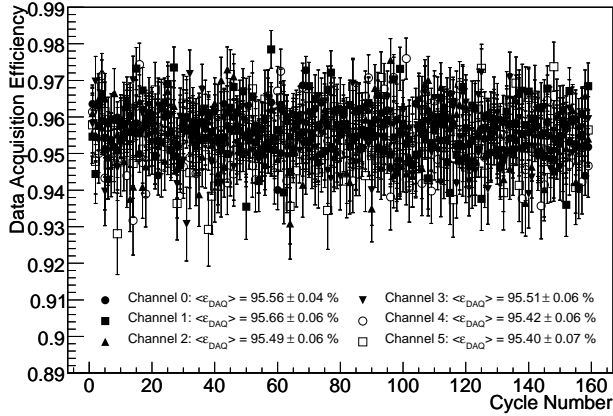


Fig. 5.5: Data acquisition efficiency in each cycle and channel of a single measurement in air at 400 hPa. One cycle corresponds to 10 minutes of measurement.

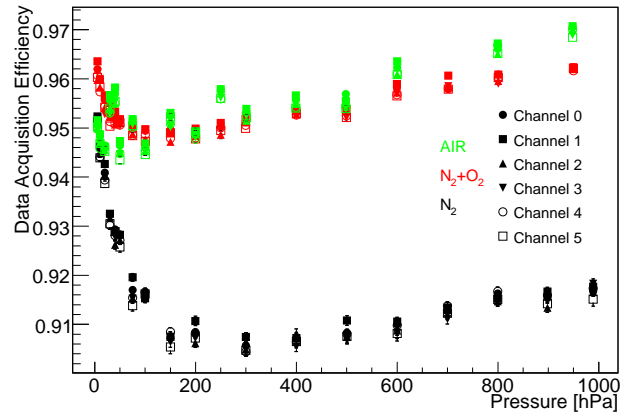


Fig. 5.6: Pressure dependence of the data acquisition efficiency. The data points correspond to all measurements used for the current analysis.

collisional quenching, the effective signal rate will again decrease until it reaches a certain equilibrium plateau. For low signal rates, the coincidence rate is mainly affected by the noise rate of the photon detectors. Therefore ε_{DAQ} even becomes sensitive to the ambient temperature. This explains the larger fluctuations between the data points in the case of air.

5.2.4 Detection Efficiencies

Unlike the data acquisition efficiency, which equally applies to all signals detected in a channel, the detection efficiency ε_{det} depends on the spectral sensitivity of the channel as well as the spectral distribution of the photons, which are going to be detected. According to equation (3.21), the detection efficiency can be calculated as

$$\varepsilon_{det} = \frac{N_{det}}{N_{real}} = \hat{f} \cdot \hat{\varepsilon}_{cut} \cdot \varepsilon_{\Omega} \cdot \underbrace{\int_{\lambda} \varepsilon_{QE}^0(\lambda) \cdot T(\lambda) \cdot \frac{d\hat{N}}{d\lambda} d\lambda}_{\varepsilon_s} \quad , \quad \hat{\varepsilon}_{cut} \equiv 1 \quad (5.14)$$

where N_{det} denotes the number of detected photons and N_{real} is the number of real photons with the normalized spectral distribution $\frac{d\hat{N}}{d\lambda}$. The efficiency $\hat{\varepsilon}_{cut}$ of the photoelectron cut is defined to unity, since its unknown value is already contained in the calibration constant \hat{f} . Nevertheless, its statistical run-to-run fluctuations have to be taken into account and have been estimated to $\sim 2\%$ by the comparison of many single-electron spectra, as is shown in Fig. 5.1. The calibration constants \hat{f} have been determined in Section 3.5.4 relatively to channel 3 and are listed in Table 3.3, whereas the value of $0.2586 \pm 0.0003\%$ for the acceptance ε_{Ω} has been obtained by means of Monte Carlo simulations described in Section 4.4. The transmission $T(\lambda)$ results to be the product of the transmissions of quartz window and filter, as is illustrated in Fig. 5.7.

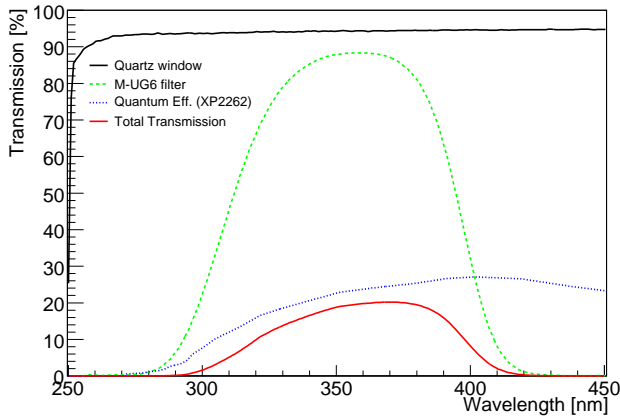


Fig. 5.7: Efficiencies of channel 0 with the M-UG6 filter. The total spectral efficiency is the product of all efficiencies.

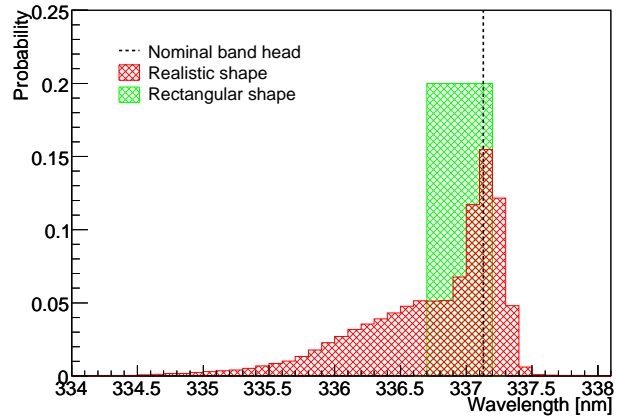


Fig. 5.8: Realistic and rectangular approaches for the spectral distribution of the $2P(0,0)$ transition at 337.13 nm.

Since the spectral efficiency ε_s depends on the spectral distributions $\frac{d\dot{N}}{d\lambda}$ of the fluorescence photons, which cannot be measured with this experiment, assumptions have to be made. Two approaches for $\frac{d\dot{N}}{d\lambda}$ have been investigated, as is shown in Fig. 5.8 for the $2P(0,0)$ transition. The first approach uses realistic spectral distributions of nitrogen transitions. The spectral information has been taken from a nitrogen spectrum [44] measured by means of a monochromator in air at 500 hPa. The single bands have been cut out and individually normalized to one. In doing so, the assumption is made that the spectral shape of these bands, which is caused by the rotational substructure, is not changing with pressure or the gas composition. The second approach used rectangular functions of 0.5 nm width, subdivided into five equidistant bins of 0.1 nm width, where the last bin with the longest wavelength is located around the position of the band head. With these assumptions about the spectral distributions, the spectral efficiencies have been evaluated similar to equation (3.27) for all transitions according to

$$\varepsilon_s = \sum_i \underbrace{\varepsilon_{QE}^0(\lambda_i) \cdot T(\lambda_i)}_{\varepsilon_s^i} \cdot P_i \quad (5.15)$$

where P_i denotes the probability of photons to emerge from the i -th wavelength bin. The error propagation in this case cannot be done by means of quadratic summation, since the main intensities of the spectral distributions are rather narrow. Under such conditions, the error of the spectral efficiencies ε_s^i has to be assumed to point always in the same direction. Therefore it has been calculated in terms of a weighted sum over all involved wavelength bins:

$$\Delta\varepsilon_s = \sum_i \Delta\varepsilon_s^i \cdot P_i \quad (5.16)$$

The error of the spectral efficiencies ε_s^i at a single wavelength λ_i is obtained by quadratic summation over the errors of the quantum efficiency and the filter transmission, whereas the error of the transmission through the quartz window again has been neglected. The

Trans.	Ch.	Filter	PMT	ε_s^{real} [%]	$\frac{\Delta\varepsilon_s^{real}}{\varepsilon_s^{real}}$ [%]	ε_s^{rect} [%]	$\frac{\Delta\varepsilon_s^{rect}}{\varepsilon_s^{rect}}$ [%]
2P(0,0)	0	M-UG6	XP2262	15.70 ± 0.81	5.14	15.80 ± 0.81	5.12
	4	340a	XP2262	5.81 ± 0.32	5.44	6.04 ± 0.33	5.41
2P(0,1)	0	M-UG6	XP2262	19.60 ± 0.86	4.39	19.60 ± 0.86	4.39
	2	360a	XP2262	5.04 ± 0.25	5.00	5.25 ± 0.26	4.95
2P(0,2)	0	M-UG6	XP2262	19.50 ± 0.79	4.08	19.40 ± 0.79	4.08
	3	380a	XP2262	10.70 ± 0.46	4.29	10.6 ± 0.45	4.29
2P(1,0)	0	M-UG6	XP2262	7.66 ± 0.55	7.18	7.72 ± 0.55	7.15
	1	317a	XP2268	9.33 ± 0.43	4.56	9.37 ± 0.43	4.56
2P(1,2)	0	M-UG6	XP2262	19.20 ± 0.86	4.46	19.20 ± 0.86	4.46
	2	360a	XP2262	1.26 ± 0.11	8.33	1.37 ± 0.11	8.18
2P(1,3)	0	M-UG6	XP2262	20.00 ± 0.83	4.15	20.00 ± 0.83	4.14
	3	380a	XP2262	7.28 ± 0.33	4.52	7.79 ± 0.35	4.47
2P(1,4)	0	M-UG6	XP2262	8.71 ± 0.34	3.86	8.50 ± 0.33	3.86
	5	394a	XP2262	4.75 ± 0.23	4.81	4.18 ± 0.21	5.00
1N(0,0)	0	M-UG6	XP2262	15.30 ± 0.60	3.91	15.20 ± 0.59	3.91
	5	394a	XP2262	7.76 ± 0.33	4.30	8.12 ± 0.35	4.27

Table 5.1: Spectral efficiencies in the different photo detector channels for all transitions considered in the current analysis, calculated for a realistic and a rectangular assumption for the spectral distribution of the nitrogen bands.

resulting values for ε_s for all transitions and channels are summarized in Table 5.1. As can be seen, the two approaches agree well within their estimated uncertainties. Therefore the following analysis has been done under the assumption of rectangular spectra for the individual transitions. This simplifies the fluorescence model and has the advantage of being nearly independent of other measurements.

Finally, the total relative error of the detection efficiencies is obtained by the quadratic sum over all error sources listed in Table 5.2. Depending on the transition and the photon detector channel, the relative error of ε_{det} ranges from 4.7 % to 9.0 %. Since the absolute calibration factor has not yet been determined precisely, it just is possible to quote an estimate of about 12 % according to the comments in Section 3.5.4. The analysis procedure is not affected by the absolute uncertainty, since it just accounts for relative differences between the single transitions.

5.2.5 Starting Values and optimal Fit Range

In order to be sure to find the global and not a local minimum of the χ^2 -function (5.10), the numerical minimization procedure needs good starting values for the parameters to be fitted. The very first value which has to be determined is the constant noise content per bin. This

Relative calibration \hat{f} :	$\sim 3\%$
Photoelectron cut ε_{cut} :	$\sim 2\%$
Spectral efficiency ε_s :	4 – 8%
Acceptance ε_Ω :	$\sim 0.4\%$
Detection efficiency ε_{det} :	5.4 – 8.8%

Table 5.2: Systematic errors of the detection efficiency.

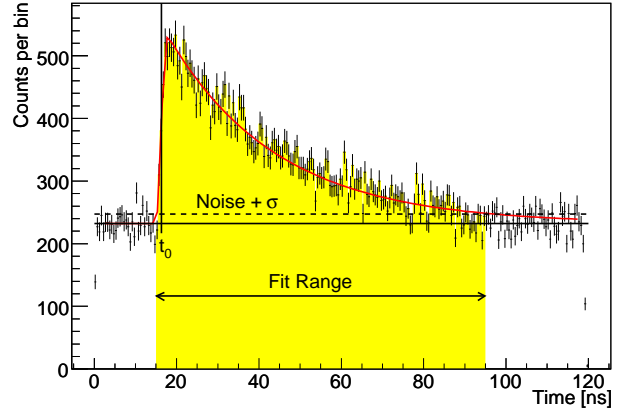


Fig. 5.9: Example for the determination of noise, time origin, and fit range. The noise is determined in the intervals between 2 ns and 12 ns as well as between 108 ns and 118 ns. The bin width amounts to 0.5 ns.

is done by averaging the bin contents in the interval between 2 ns and 12 ns according to

$$\langle N_{noise} \rangle = \frac{1}{N_{bins}} \sum_i^{N_{bins}} N_{noise}^i \quad , \quad \sigma_{N_{noise}} = \sqrt{\langle N_{noise}^2 \rangle - \langle N_{noise} \rangle^2} \quad (5.17)$$

which is always possible, since the fluorescence signal typically starts to rise at around 15 ns, as can be seen in Fig. 5.9. A second computation is done at the end of the coincidence interval in the range between 108 ns and 118 ns. For large fluorescence lifetimes, the signal tail may overlap with this interval. Therefore the second noise value is only used, if it is smaller than or equal to the first value. If this is the case, the weighted average of both values is taken as mean noise content per bin. Otherwise just the first value is used. The noise will be fixed during the entire analysis.

The next values, which have to be determined, are the time origin and the lifetime of the fluorescence signal. A first guess of the lifetime is obtained by a fit with a simple exponential function to the signal tail. Afterwards, the whole signal distribution is fitted by the function (5.7) over the complete coincidence interval, as is shown in Fig. 5.9, where the position of the maximum bin is taken as start value for the time origin and the time resolution is set to 0.8 ns. Superpositions of different signal contributions are not taken into account at this stage. These individual fits to each time spectrum deliver the final start values for the time origins, the lifetimes, the signal intensities, and the time resolutions. The obtained time origins and resolutions of all channels are plotted in Fig. 5.10 against the pressure. For pressures larger than 100 hPa both quantities are rather stable. The large fluctuations and systematical drifts at low pressures are due to the low statistics and the stronger influence of correlated background. Since the time origin and the resolution of a certain channel should approximately be the same for all pressures, they will be varied with a common value for each channel during the data analysis. The start values for the intensity ratios $R_{v',v''}$ of

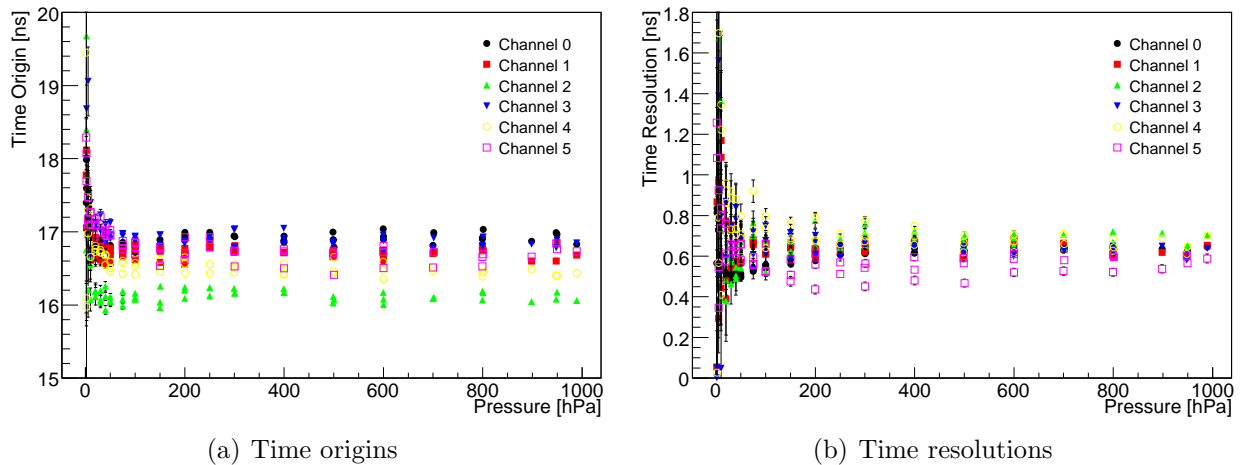


Fig. 5.10: Individually determined time origins and resolutions of all measurements, considered in the following analysis. Since these values should be approximately constant, they will be varied with a common value for each channel during the data analysis.

the considered transitions have been obtained from the ratios of the corresponding Einstein coefficients listed in Table 2.1.

Another important issue is the determination of the optimal fit range. Since the noise per bin will be fixed during the minimization, the fitting should consider only bins, where the signal is larger than the noise fluctuations. Otherwise, the minimization would result into too small χ^2 -values, which would bias the error calculation. Therefore the fit range $[t_{min}, t_{max}]$ is dynamically determined by the condition

$$f(t) > \langle N_{noise} \rangle + \sigma_{N_{noise}} \quad , \quad t_{min} < t < t_{max} \quad (5.18)$$

where $f(t)$ is the previously fitted function to the signal distribution, shown in Fig. 5.9. Since several TDC channels show fluctuations at the edges of the coincidence interval, as can be seen in Fig. 3.36, the maximum allowed fit range is always restricted to [12 ns, 95 ns]. Apart from these statistical considerations, the restriction of the fit range additionally speeds up the computing time, since the summations in equation (5.10) now have to be done over a much smaller number of bins.

5.3 Study of Nitrogen Quenching in different Gas Mixtures

According to the separation ansatz from equation (2.23), the excitation and the de-excitation can be considered as two independent processes. All the de-excitation parameters, as the intensity ratios between transitions from the same vibrational state, the quenching rate constants, and intrinsic lifetimes, do not depend on the mechanism of excitation. Once a molecular state is excited, it will relax according to the ambient conditions, regardless of

Transition	λ [nm]	Ch. 0 (M-UG6)	Ch. 1 (317a)	Ch. 2 (360a)	Ch. 3 (380a)	Ch. 4 (340a)	Ch. 5 (394a)
2P(3,2)**	311.67	×	×				
2P(2,1)*	313.60	×	×				
2P(1,0)	315.93	×	×				
2P(1,1)**	333.90	×				×	
2P(0,0)	337.13	×				×	
2P(1,2)	353.67	×		×			
2P(0,1)	357.69	×		×			
2P(4,6)**	364.17	×		×			
2P(3,5)**	367.19	×		×			
2P(2,4)**	371.05	×			×		
2P(1,3)	375.54	×			×		
2P(0,2)	380.49	×			×		
2P(3,6)*	389.46	×					×
1N(0,0)	391.44	×					×
2P(2,5)**	394.30	×					×
2P(1,4)	399.84	×					×

Table 5.3: Major contributions in the different photo detector channels. Transitions which are marked with an * or ** have not been taken into account in the analysis. Two ** denote transitions which are typically very weak or at the edges of the filter ranges.

the way it got excited. Therefore in this work the de-excitation is studied by means of the lifetimes and relative intensities of transitions emerging from the same vibrational state, which naturally decouples the de-excitation from the excitation process. Additionally, this allows the use of the full energy range from 250 keV to 2000 keV, to take advantage of the maximum statistic.

In the following analysis, only the most intensive nitrogen transitions, listed in Table 5.1, are taken into account. As already mentioned previously, these transitions originate only from the three independent transition systems $2P(0, v'')$, $2P(1, v'')$ and $1N(0, v'')$. The $2P(0,0)$ as well as the $2P(1,0)$ transitions are considered to be the only transitions within the filter range of the dedicated photon detectors. In the case of the $2P(0,0)$ transition this does not cause any problems, but for the $2P(1,0)$ transition it is just an approximate assumption, since there are other weak contributions of the $2P(2,1)$ and $2P(3,2)$ bands, as can be seen in Table 5.3 and Fig. 5.2. Unfortunately, these transitions cannot be considered by the minimization, since they have no strong or single counterpart in one of the other photon detectors. Therefore the minimization very likely would produce random values for these transitions, which could lead to an uncontrolled underestimation of the $2P(1,0)$ transition.

Another problem arises from the $1N(0,0)$ transition, since its dedicated channel 5 is contaminated by several weak bands of the higher vibrational transitions $2P(3,6)$, $2P(2,5)$, $2P(1,4)$. Luckily, transitions of the $1N$ system have much longer intrinsic lifetimes and

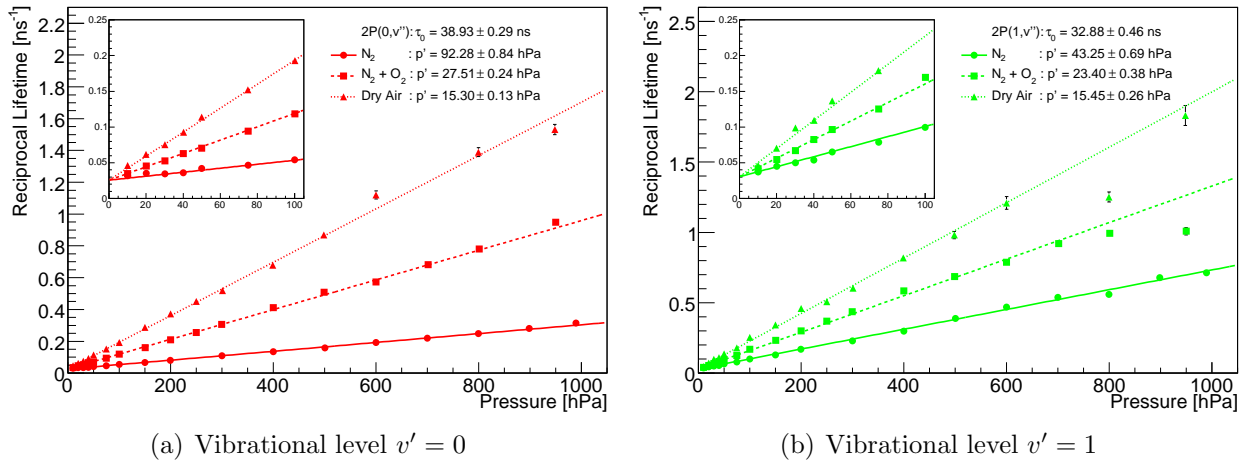


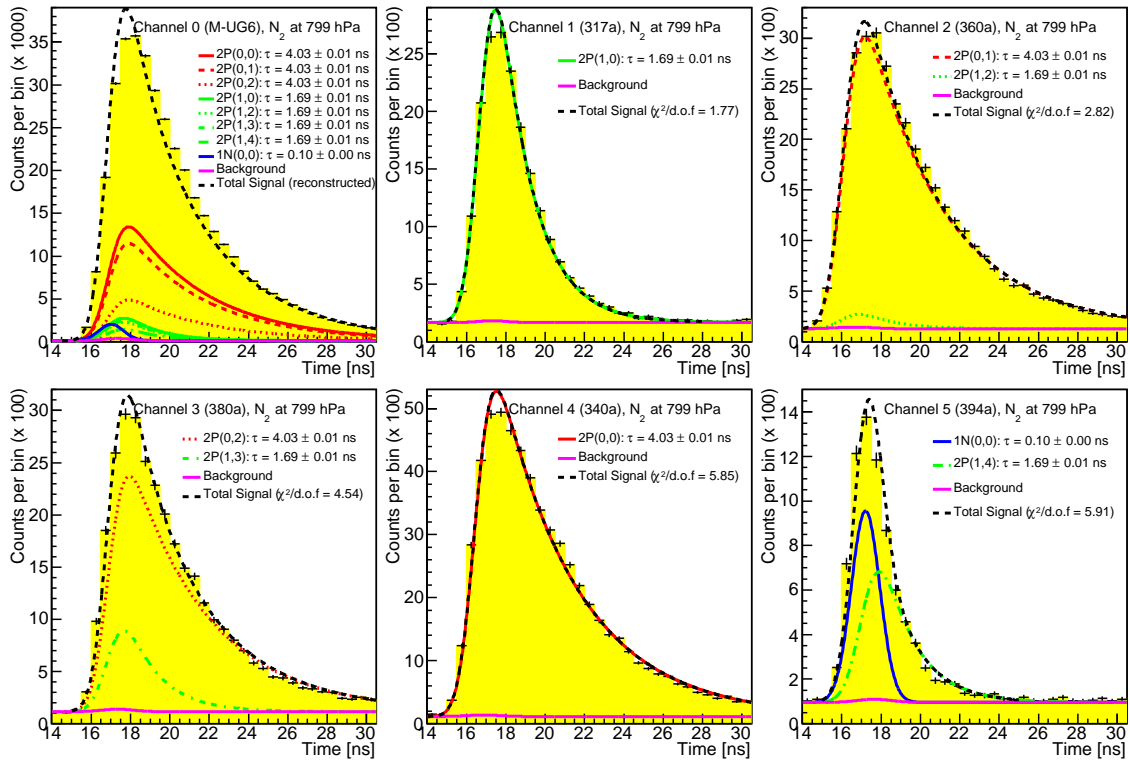
Fig. 5.11: Stern-Vollmer plots of the pressure dependence of the reciprocal lifetimes for the vibrational states $v' = 0, 1$ of the 2P system. The lines are not a direct fit to the data points but illustrate the pressure dependence derived from the lifetimes and the quenching rate constants, obtained by the final minimization with a linear constraint on the reciprocal lifetimes.

are also more affected by the collisional quenching than the 2P transitions. Therefore the evolution of their time spectra with the pressure differs much from the 2P transitions. This can be used as a handle to unscramble the 1N(0,0) transition from the 2P contaminations. In order to avoid negative effects on the results for the 2P transitions, the analysis is done in two steps. At first, only the transitions of the 2P system are studied by excluding channel 5 from the analysis. Afterwards, just channel 5 is analyzed, keeping the lifetime of the 2P(1,4) transition fixed to the values obtained by the previous analysis of the 2P system.

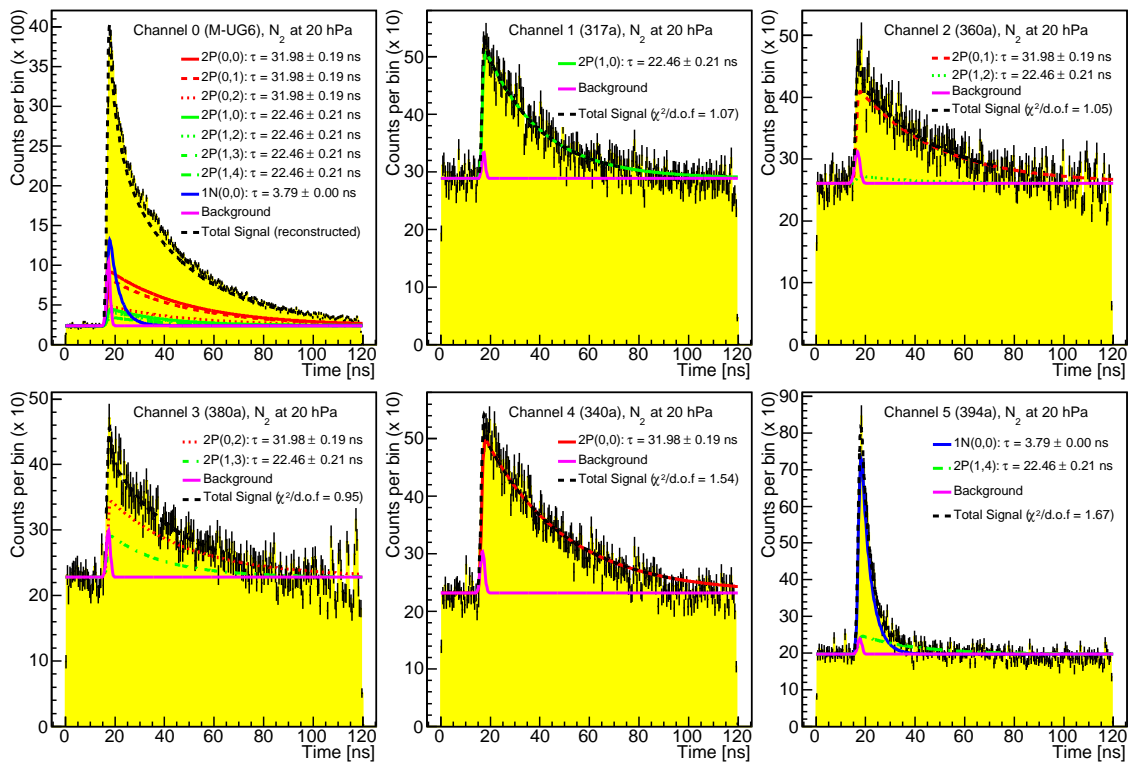
The analysis of the 2P system is only done for pressures higher than or equal to 10 hPa, in order to minimize systematic effects on the results due to small gas impurities. The time spectra of 46 single measurements in nitrogen, artificial air, and a mixture of nitrogen and oxygen (90:10) have been fitted simultaneously by the general minimization function (5.10). An example for the resulting contributions in each channel and their variability with the pressure is given by the time spectra in Fig. 5.12 and Fig. 5.13 for nitrogen and air at 20 hPa and 800 hPa. Channel 0 with the M-UG6 filter is always excluded from the minimization, but the sum of contributions to this channel has been reconstructed from the results in the other channels.

The obtained reciprocal lifetimes of the vibrational levels $v' = 0, 1$ are plotted against the pressure in the so-called Stern-Vollmer plot in Fig. 5.11 for the three gas mixtures. The data shows a clear linear dependence on the pressure. Some deviations may be explained by an insufficient separation of different contributions. Values for the intrinsic lifetimes $\tau_{0v'}$ and the reference pressures $p'_{v'}$ can be obtained by a linear combined fit to the data in Fig. 5.11 according to the model (2.41), which has been introduced in Section 2.3.3:

$$\frac{1}{\tau_{v'}(p)} = \frac{1}{\tau_{0v'}} \left(1 + \frac{p}{p'_{v'}} \right), \quad (5.19)$$

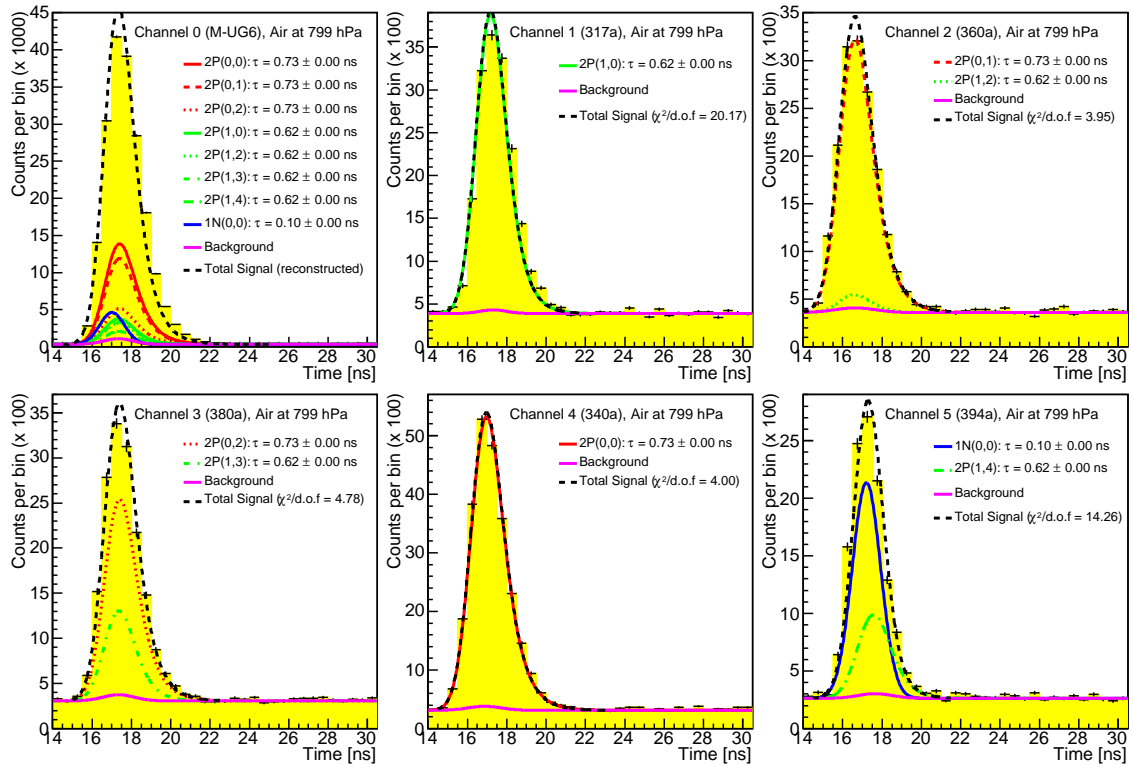


(a) Nitrogen at 800 hPa

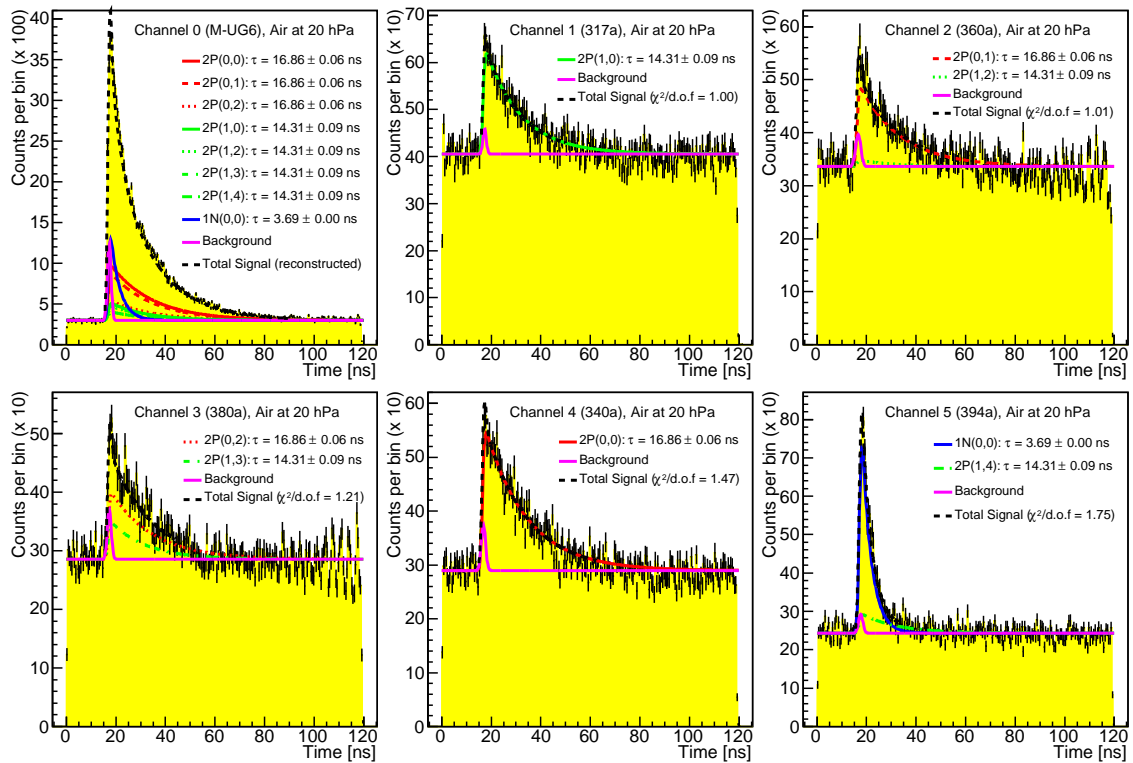


(b) Nitrogen at 20 hPa

Fig. 5.12: Time spectra in nitrogen at 20 hPa and 800 hPa (different time ranges are displayed in both cases). The signal in channel 0 is not fitted but has been reconstructed from the signals in the other channels (see also Fig. 5.16). For low pressures the background contributions are not negligible.



(a) Dry air at 800 hPa



(b) Dry air at 20 hPa

Fig. 5.13: Time spectra in dry air at at 20 hPa and 800 hPa (different time ranges are displayed in both cases). The signal in channel 0 is not fitted but has been reconstructed from the signals in the other channels (see also Fig. 5.16). For low pressures the background contributions are not negligible.

where $\tau_{0v'}$ is in common for all gases but the values $p'_{v'}$ depend on the gas mixture. The reference pressure p' is just a convenient physical quantity, if one deals with constant mixing ratios of the gas. The real nature of the quenching is better described by the collisional cross-sections or the more comfortable quenching rate constants of the different gas constituents. In this notation the reciprocal lifetimes can be expressed as

$$\frac{1}{\tau_{v'}(p)} = \frac{1}{\tau_{0v'}} \left(1 + \underbrace{\frac{\tau_{0v'}}{kT} \cdot \sqrt{\frac{T}{293 \text{ K}}} \cdot \left[f_{N_2} \cdot Q_{N_2}^{v'} + f_{O_2} \cdot Q_{O_2}^{v'} + f_{Ar} \cdot Q_{Ar}^{v'} \right]}_{1/p'_{v'}} \cdot p \right), \quad (5.20)$$

where f_x denotes the fractions of molecules or atoms of the corresponding gas constituent x . Since the pressure dependence of the reciprocal lifetimes turned out to be rather linear, as follows from Fig. 5.11, the minimization has been repeated by expressing the individual lifetimes in the minimization function (5.10) through equation (5.19). This condition leads to further “vertical” connections between the datasets in Fig. 5.4 and reduces the number of free parameters from 196 to 112. Additionally, it now is possible to account for slight temperature differences between the measurements. This minimization method directly leads to a consistent set of quenching rate constants, lifetimes, and intensity ratios, including the correlations between them. The reduced global χ_r^2 turned out to be 1.77 and the resulting parameter values are listed in Table 5.4 and Table 5.5 together with their correlation coefficients in Fig. 5.14. The pressure dependence of the reciprocal lifetimes, derived from these values, is illustrated by the lines in Fig. 5.11, which are in good agreement with the single data points obtained from the previous minimization.

The systematic error of the intensity ratios has been obtained from the systematic uncertainties of the detection efficiencies. According to equation (2.44), the intensity ratios are defined as

$$R_{v',v''} = \frac{N_{v',v''}}{N_{v',0}} = \frac{n_{v',v''}/\varepsilon_{v',v''}}{n_{v',0}/\varepsilon_{v',0}}, \quad (5.21)$$

where the $N_{v',v''}$ are the absolute and $n_{v',v''}$ denote the measured intensities of the transitions with a detection efficiency $\varepsilon_{v',v''}$. The relative systematic error of the ratio $R_{v',v''}$ thus becomes

$$\frac{\Delta R_{v',v''}}{R_{v',v''}} = \sqrt{\left(\frac{\Delta N_{v',v''}}{N_{v',v''}} \right)^2 + \left(\frac{\Delta N_{v',0}}{N_{v',0}} \right)^2} = \sqrt{\left(\frac{\Delta \varepsilon_{v',v''}}{\varepsilon_{v',v''}} \right)^2 + \left(\frac{\Delta \varepsilon_{v',0}}{\varepsilon_{v',0}} \right)^2} \quad (5.22)$$

In this case, the relative errors of the detection efficiencies have been calculated without taking into account the error of the acceptance ε_Ω , since the acceptance of each channel is identical and therefore does not affect the intensity ratios. However, the acceptance error is very small, as can be seen in Table 5.2, and is negligible with respect to the other errors.

As has already been pronounced previously, the quenching parameters of the 1N system have been determined separately by a combined analysis of channel 5 only. In order to separate the 1N(0,0) transitions from the 2P contaminations, the pressure dependence of the lifetimes of the 2P(1,4) transition has been fixed to the values obtained by the previous

Transition	τ_0 [ns]	Q_{N_2} [10^{10} cm 3 s $^{-1}$]	Q_{O_2} [10^{10} cm 3 s $^{-1}$]	Q_{Ar} [10^{10} cm 3 s $^{-1}$]
2P(0, v'')	38.93 ± 0.29	0.113 ± 0.000	2.764 ± 0.009	< 1.9 98 % C.L.
2P(1, v'')	32.88 ± 0.46	0.285 ± 0.001	2.697 ± 0.026	< 2.3 98 % C.L.
1N(0, v'')	65.22 ± 18.68	5.003 ± 0.165	5.240 ± 0.786	< 48.4 98 % C.L.

Table 5.4: Results for the intrinsic lifetimes $\tau_{0v'}$ and quenching rate constants. The quenching rate constants refer to a temperature of 20 °C. In the case of argon an upper limit is quoted for the quenching rate constants, since the argon fraction in the air has just been 1 %.

System	v'	v''	Intensity Ratio
2P	0	0	$1.00 \pm 0.00 \pm 0.00$
	0	1	$0.69 \pm 0.00 \pm 0.06$
	0	2	$0.29 \pm 0.00 \pm 0.02$
2P	1	0	$1.00 \pm 0.00 \pm 0.00$
	1	2	$0.33 \pm 0.03 \pm 0.04$
	1	3	$0.34 \pm 0.01 \pm 0.03$
	1	4	$0.46 \pm 0.02 \pm 0.04$
1N	0	0	$1.00 \pm 0.00 \pm 0.00$

Table 5.5: Results for the intensity ratios of the investigated nitrogen transitions. The second error accounts for systematic uncertainties of the detection efficiencies. The ratio of the 2P(1,4) transition is an effective ratio, since it still contains contributions of other 2P transitions.

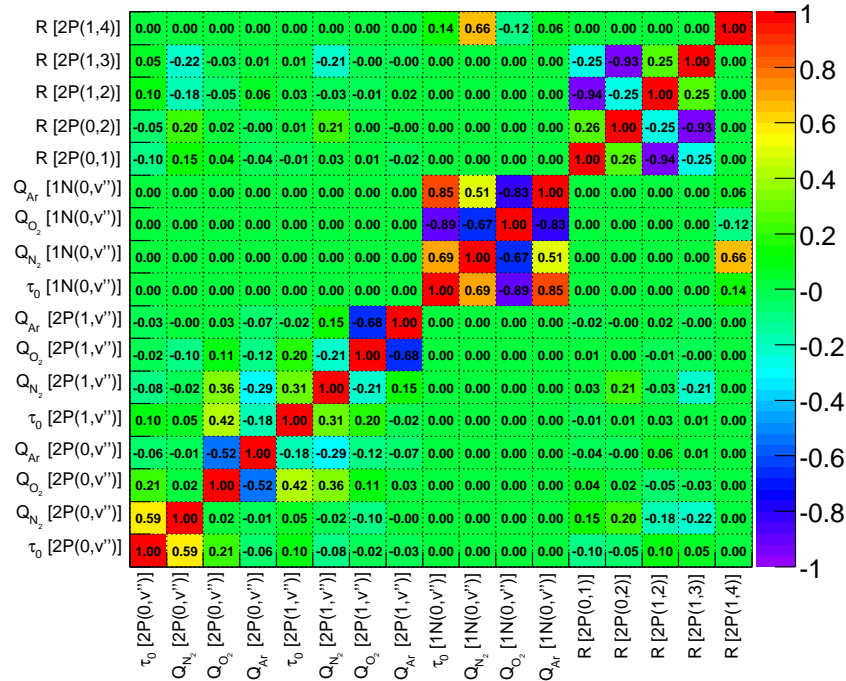


Fig. 5.14: Correlation matrix for the quenching parameters of the analyzed vibrational levels of the 2P and 1N system. Due to the separated analysis of the 2P and the 1N systems, the correlation between them is zero.

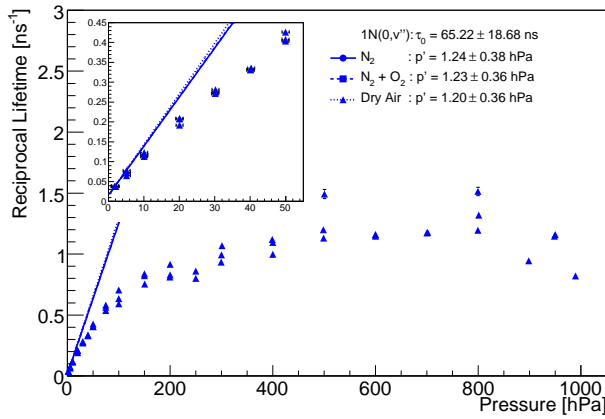


Fig. 5.15: Stern-Vollmer plots of the pressure dependence of the reciprocal lifetimes of the $1N(0, v'')$ transitions. The lines correspond to the pressure dependence obtained by the minimization with a linear constraint on the reciprocal lifetimes.

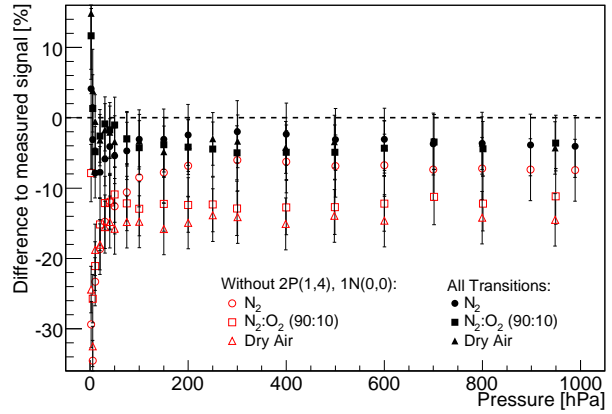


Fig. 5.16: Relative differences between the reconstructed and the measured signal in channel 0 with the M-UG6 filter (systematic errors are included). The red open symbols show the reconstructed signal without the transitions in channel 5.

analysis of the 2P system and just the intensity ratio was allowed to vary during the fitting by the general minimization function (5.10). The other 2P contaminations have been neglected, since they do not have a counterpart in the other channels. In contrast to the 2P system, even measurements at 2 hPa and 5 hPa have been considered in the analysis, since the relative intensities of the 1N transitions get much stronger at low pressures. Furthermore, the 1N system is less affected by gas impurities due to the large self quenching rate of nitrogen. The reciprocal lifetimes obtained by this analysis are shown in the Stern-Vollmer plot in Fig. 5.15. Compared to the corresponding plots of the 2P system in Fig. 5.11, a linear increase of the reciprocal lifetimes is hardly visible in this case. Just for pressures lower than 50 hPa the data seems to adopt a linear behavior. This is due to the 2P contaminations, which for pressures larger than ~ 50 hPa too much bias the minimization results. Below 50 hPa the intensity of the 1N transition is strong enough to be silhouetted against the 2P contaminations. Therefore the minimization has been repeated just for pressures between 2 hPa and 50 hPa by constraining the lifetimes through expression (5.19), as has already been done for the 2P system. The global reduced χ_r^2 value in this case turned out to be 1.26 and the resulting values for the lifetime, quenching rate constants, and intensity ratios are summarized in Table 5.4 and Table 5.5 together with the values of the 2P system. The intensity ratio of the 2P(1,4) transition is just an effective measure for all of the 2P contaminations in the 1N channel, since it still contains other contributions of the 2P system. The lines in Fig. 5.15 represent the pressure dependence of the reciprocal lifetimes for the three gases, as follows from the last minimization. Since their slopes (p' values) are roughly the same, there is nearly no difference between the three kinds of gases. Therefore the quenching of the $1N(v' = 0)$ state is mainly due to the nitrogen self quenching. The deviation of the data points from the lines below 50 hPa is still caused by 2P contaminations. Only

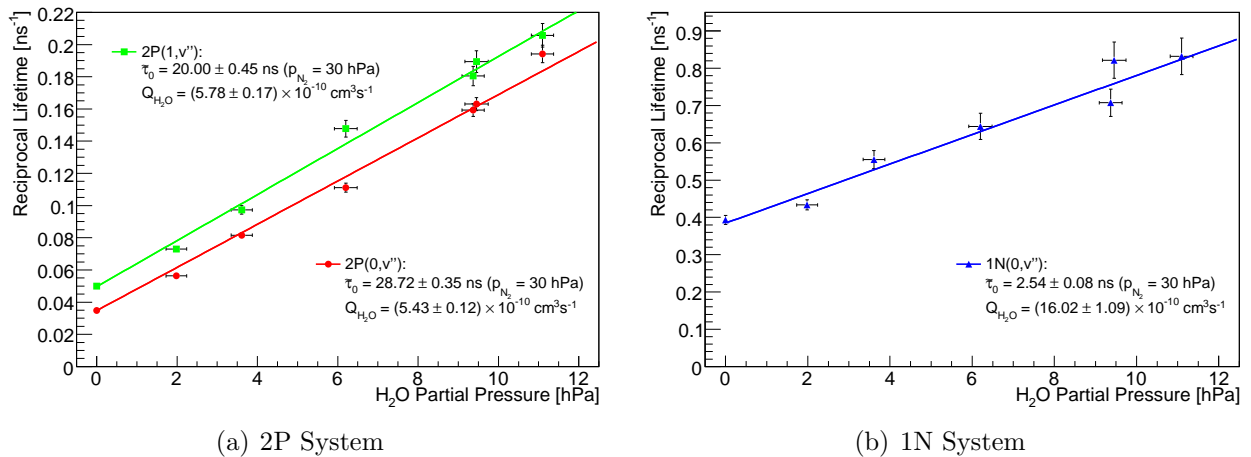


Fig. 5.17: Reciprocal lifetimes for mixtures of 30 hPa nitrogen plus a variable amount of water vapor according to the H_2O partial pressure on the x-axis. The data point at zero vapor partial pressure corresponds to the reciprocal lifetime $1/\tilde{\tau}_0$ of pure nitrogen at a pressure of 30 hPa.

the minimization with the linear constraint (5.19) is able to separate the 2P from the 1N contributions correctly.

The parameters in Table 5.4 and Table 5.5 completely describe the relative intensities and the pressure dependence of the investigated nitrogen transitions. To check their compatibility over the whole pressure range between 2 hPa and 1000 hPa, the complete set of measurements has been fitted again, where the values for the lifetimes, quenching rate constants, and intensity ratios have been fixed and just the intensities of the main transitions have been varied. The resulting relative differences between the reconstructed and the measured signal in channel 0, with the M-UG6 filter of the Pierre Auger fluorescence telescopes, are shown in Fig. 5.16, where the errors already account for systematic uncertainties. For pressures larger than 10 hPa the differences are in the order of -3 %. This deviation is not necessarily due to systematic effects. A small underestimation of the signal has to be expected, since not all the transitions in the M-UG6 filter range have been measured by the other channels. The open red symbols show the relative differences in the case of neglecting the 1N(0,0) and 2P(1,4) transition in channel 5.

5.4 Study of Humidity Effects

The study of the influence of water vapor on the quenching is important, because the water vapor concentration in the atmosphere is always changing according to the altitude and the current weather conditions. Therefore the description by means of the reference pressures p' is not suited anymore, but instead of this the quenching rate needs to be directly derived from the quenching rate constants or collisional cross sections for nitrogen-water collisions.

For the measurements of the quenching rate constants, the chamber has been completely evacuated and afterwards filled with a certain amount of water vapor as described in Sec-

Transition	$Q_{\text{H}_2\text{O}}$ [$10^{-10}\text{cm}^3\text{s}^{-1}$]
2P(0, v'')	5.43 ± 0.12
2P(1, v'')	5.78 ± 0.17
1N(0, v'')	16.02 ± 1.09

Table 5.6: Quenching rate constants for water vapor referring to a temperature of 20 °C.

tion 3.3. The water vapor concentration has been controlled by the humidity probe as well as the pressure sensor, which in this case is measuring the partial pressure of the water vapor. The humidity concentration needs some time to stabilize, since the water vapor attaches to the surfaces of the chamber. After the water vapor concentration has reached a rather stable value, 30 hPa of pure nitrogen have been added. Six individual measurements have been performed at room temperatures between 15 °C and 17 °C and relative humidities ranging from 10 % rH to 60 % rH. Each measurement lasted for roughly 30 hours. Only data of the last ~ 20 hours has been used for the analysis, to ensure the water vapor concentration to be in thermal equilibrium with the surrounding chamber walls.

The data analysis has been done by a simultaneous fit of all measurements by means of the general minimization function (5.10). The intensity ratios have been fixed to the values from the previous analysis listed in Table 5.5. The global reduced χ_r^2 value turned out to be 1.09 and the resulting lifetimes for the three transition systems are plotted in Fig. 5.17 against the water vapor partial pressure $p_{\text{H}_2\text{O}}$, which has been calculated from the relative humidity values of the humidity probe according to equation (2.48). The corresponding error has been derived from the absolute systematic uncertainty of 1.5 % rH of the humidity probe. Finally, the quenching rate constants $Q_{\text{H}_2\text{O}}$ for water vapor have been obtained through a fit of the linear expression

$$\frac{1}{\tau} = \frac{1}{\tau_0} + \sqrt{\frac{T}{293 \text{ K}}} \cdot \left(\frac{p_{\text{N}_2}}{kT} \cdot Q_{\text{N}_2} + \frac{p_{\text{H}_2\text{O}}}{kT} \cdot Q_{\text{H}_2\text{O}} \right) = \frac{1}{\tilde{\tau}_0} + \sqrt{\frac{T}{293 \text{ K}}} \cdot \frac{p_{\text{H}_2\text{O}}}{kT} \cdot Q_{\text{H}_2\text{O}} \quad (5.23)$$

to the data points in Fig. 5.17. The data point at zero pressure with lifetime $\tilde{\tau}_0$ has been added from the previous measurements in dry nitrogen at a pressure of 30 hPa. The obtained values for the quenching rate constants are listed in Table 5.6. For the 2P system the quenching rate constants of water vapor are roughly two times the corresponding values of oxygen, whereas the quenching of the 1N system by water vapor is roughly three times stronger than for nitrogen or oxygen. This large quenching rate may be explained by the polar nature of the H_2O and the N_2^+ molecules. However, the effect on the nitrogen quenching in the atmosphere is expected to be rather small, since the water vapor concentrations usually are much lower than the constant oxygen fraction of about 21 %. Further comments on the effect of water vapor are given in Section 5.6.

5.5 Study of Energy Dependence of the Fluorescence Yields

Once the quenching parameters are known, the signal intensities for the three main bands 2P(0,0), 2P(1,0) and 1N(0,0) at any pressure and temperature in principle can be calculated according to the model

$$N_{S(v')}(p, T) = N_{S(v')}^0 \cdot \frac{\tau_{0S(v')}}{\tau_{S(v')}(p, T)} = N_{S(v')}^0 \cdot \left(1 + \frac{p}{p'_{S(v')}(T)} \right) . \quad (5.24)$$

The only remaining unknown quantity is the parameter $N_{S(v')}^0$, which corresponds to the number of emitted photons into the band $S(v', 0)$ in the absence of collisional quenching. The fluorescence model described in Section 2.3 assumes $N_{S(v')}^0$ to be proportional to the total deposited energy E_{dep} in the gas

$$N_{S(v')}^0 = Y_{S(v')}^0 \cdot E_{dep} , \quad (5.25)$$

where the intrinsic fluorescence yield $Y_{S(v')}^0$ denotes the number of excited states per deposited energy, which, in the absence of collisional quenching, would optically relax with a mean lifetime $\tau_{0S(v')}$ into the lower state of the corresponding transition $S(v', 0)$.

For the determination of the intrinsic fluorescence yield $Y_{S(v')}^0$, the energy deposit in the gas has to be known. Since it cannot be measured directly, Monte-Carlo simulations have been performed as described in Section 4.3. The simulations provide the energy deposit profiles as well as the migration matrix of the electron energies at a given pressure. The migration matrix transforms the initial electron energy distribution at the collimator exit into the final energy distribution of the detected electrons and thus describes the migration between the bins of the energy spectra. Since the simulation assumes a perfect energy resolution of the scintillation detector, the energy deposit profile as well as the migration matrix have been individually smeared out for each dataset. This has been done by randomizing the detected energy in the simulation data by a Gaussian distribution, where the standard deviation $\sigma_E(E)$ corresponds to the energy resolution of the measured data, on which the simulation data has to be applied. An example of the final energy deposit profiles and the migration matrix is shown in Fig. 5.18 and 5.19. Since the atomic numbers and weights of nitrogen and oxygen are nearly the same and the nitrogen fraction in the mixtures is always larger than 80 %, the ionization energy loss for all gases used in the measurements is assumed to be the same as in pure nitrogen. The total energy deposit E_{dep} in the gas is obtained by averaging the simulated energy deposit profile over the measured energy distribution of the electrons $\frac{dN_e}{dE_f}$ according to

$$E_{dep} = \int \langle E_{dep}^{sim} \rangle \cdot \frac{dN_e}{dE_f} dE_f \quad (5.26)$$

Since the simulated energy deposit profiles correspond to the mean total energy, which has been deposited per detected electron in the whole chamber volume, even secondary delta electrons are treated correctly in this manner.

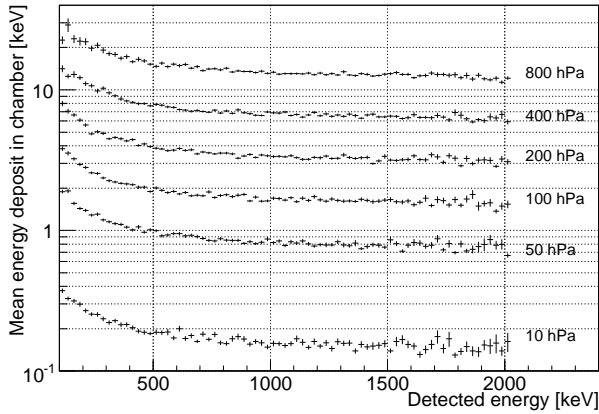


Fig. 5.18: Mean energy deposit $\langle E_{dep} \rangle$ per electron versus the detected energy in the scintillator for various pressures.

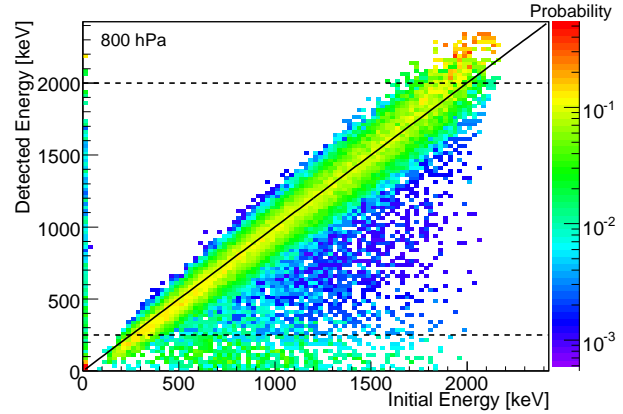


Fig. 5.19: Migration matrix, containing the probabilities for an electron with initial energy E_i to be detected with an final energy E_f .

The initial energy distribution of the electrons has been reconstructed by the linear transformation

$$\mathbf{N}_i = \mathbf{M}^{-1} \cdot \mathbf{N}_f \quad , \quad (5.27)$$

where \mathbf{M} is the migration matrix and the vectors \mathbf{N}_i , \mathbf{N}_f denote the histograms of the initial and final energy distributions. An example for the migration matrix is given in Fig. 5.19, where the horizontal dashed lines are the limits of the maximum energy range considered in the analysis. The summation over the single rows always results to be one. Entries in the column at zero initial energy correspond to secondary electrons induced by Bremsstrahlung photons, whereas the slight excess of entries in the rows below 250 keV stems from low energy secondary electrons, which have been detected instead of the primary electron. An example for differences between the detected and the initial energy spectra after the transformation is shown in Fig. 5.20. Since the energy spectra may have some tails, the median has been used instead of the mean value to characterize the average initial energy of the electrons. The corresponding error intervals have been chosen such, that 68 % of the electron energies emerge from the asymmetric error interval around the median. In case of a Gaussian energy distribution, this would correspond to the normal error definition in terms of one standard deviation.

With the knowledge of the average initial electron energies and the total energy deposit in the gas, the intrinsic fluorescence yield can be determined. This again has been done through the minimization of the general χ^2 -function (5.10) where the signal intensities N_{ds} in equation (5.11) have been substituted by the expression

$$N_{ds} = Y_s^0 \cdot E_{dep}^d \cdot \left(1 + \frac{p}{p'_s} \right)^{-1} \quad (5.28)$$

Besides Y_0^s , all the other parameters as well as the values for the time origins and time resolutions of each channel have been fixed to the values obtained in the previous quenching

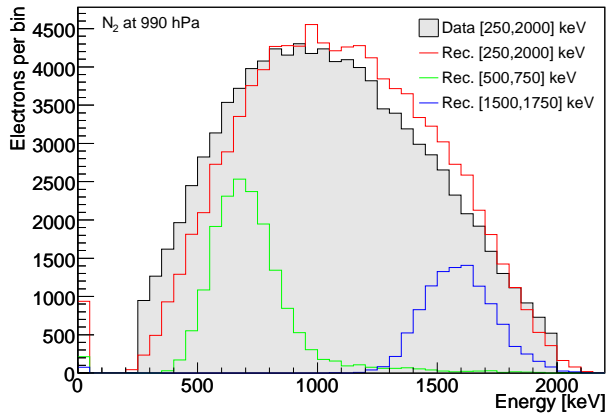


Fig. 5.20: Measured and reconstructed initial energy spectra at 990 hPa for different ranges of the detected energy

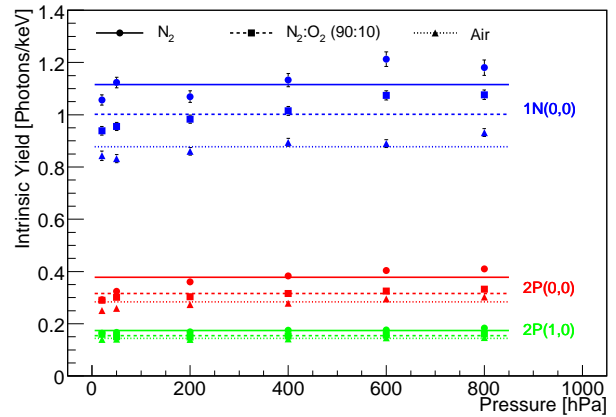
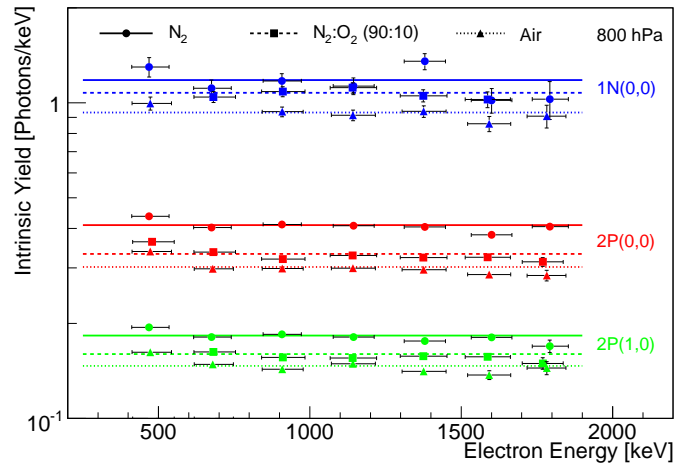


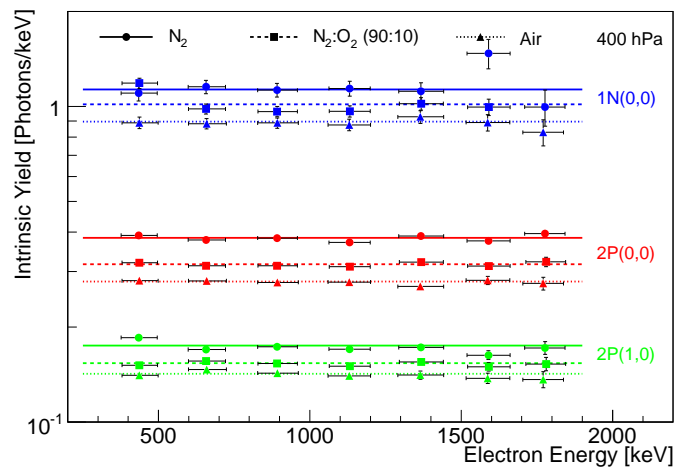
Fig. 5.21: Observed pressure dependence of the intrinsic fluorescence yield. The horizontal lines correspond to the values in Table 5.7 and denote the weighted average of the data points over the pressure.

analysis. To study the energy dependence of Y_0^s , the data has been divided into sub-samples of 7 energy intervals of 250 keV width, ranging from 250 keV to 2000 keV. Furthermore, the minimization has been individually applied to several measurements, distributed over the whole pressure range, to uncover potential pressure dependencies. The results of these studies are illustrated in Fig. 5.22 for three representative pressures. The electron energies and errors in these figures have been calculated by means of the migration matrix according to the method described above. The intrinsic fluorescence yields of the main transitions result to be fairly constant over the investigated energy range in all kinds of gases and in all pressure domains. Therefore their final values have been determined through a subsequent application of the minimization procedure on the complete energy range between 250 keV and 2000 keV. These values are represented by the horizontal lines in Fig. 5.22 and are in good agreement with the data points of the single energy intervals. The differences in the intrinsic fluorescence yield for the three kinds of gases roughly correspond to their different nitrogen proportions, as it was expected. An increase of the intrinsic fluorescence yield in air due to the 1 % argon contribution, as it is expected by several authors [14, 22], is hardly to state. To answer this question additional measurements with larger argon fractions would be needed.

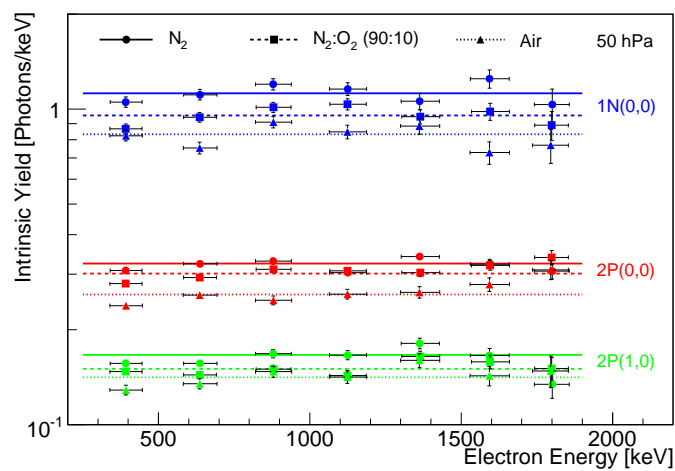
On closer examination of Fig. 5.22, a slight increase of the fluorescence yield with the pressure can be recognized. This effect can be better seen in Fig. 5.21, where the intrinsic fluorescence yields are plotted against the pressure. The data points in this figure correspond to the values of the horizontal lines in Fig. 5.22. Apparently, the 2P(0,0) transition in pure nitrogen shows the strongest pressure dependence. This effect is not yet understood but it is very likely due to experimental problems or inconsistencies in the model or the simulation data, as for instance energy deposit profiles, acceptances, or angular distributions, which in principle all depend on the pressure. Since the origin of this effect could not be clarified, the



(a) 800 hPa



(b) 400 hPa



(c) 50 hPa

Fig. 5.22: Energy dependence of the intrinsic fluorescence yields at three different pressures. The horizontal lines are not a direct fit to the data points, but represent the resulting values from the minimization over the complete energy range.

Gas	$Y_{2P(0,0)}^0$ [ph./keV]	$Y_{2P(1,0)}^0$ [ph./keV]	$Y_{1N(0,0)}^0$ [ph./keV]
N ₂	$0.378 \pm 0.001 \pm 0.049$	$0.174 \pm 0.001 \pm 0.011$	$1.115 \pm 0.010 \pm 0.076$
N ₂ + O ₂	$0.316 \pm 0.001 \pm 0.024$	$0.155 \pm 0.001 \pm 0.009$	$1.002 \pm 0.007 \pm 0.074$
Dry Air	$0.283 \pm 0.001 \pm 0.027$	$0.144 \pm 0.001 \pm 0.009$	$0.877 \pm 0.006 \pm 0.061$

Table 5.7: Intrinsic fluorescence yields for the three main transitions 2P(0,0), 2P(1,0) and 1N(0,0). The systematic errors are due to uncertainties in the detection efficiencies as well as the averaging over the pressure. The quoted values are still relative to channel 3. To obtain absolute results they have to be multiplied with the absolute calibration factor $C_{\text{abs}} = 1.195 \pm 0.141$ derived in Section 3.5.4.

final results for the intrinsic fluorescence yields have been derived as the weighted average over the whole pressure range. These values are represented by the horizontal lines in Fig. 5.21 and are summarized in Table 5.7. The systematic error due to the pressure dependence has been calculated as the standard deviation of the single data points to the averaged value and turned out to be in the order of 7 % for air and 12 % for pure nitrogen. Furthermore, the relative systematic uncertainties of the detection efficiencies need to be added quadratically to obtain the systematic errors quoted in Table 5.7.

The intrinsic fluorescence yield of any other transition can be calculated with the values quoted in Table 5.7 by multiplying with the corresponding intensity ratio from Table 5.5.

$$Y_{S(v',v'')}^0 = R_{S(v',v'')} \cdot Y_{S(v',0)}^0 \quad (5.29)$$

The systematic error in this case can be obtained just by substituting the relative detection efficiency error of the main transition $S(v',0)$ by the relative detection efficiency error of the transition $S(v',v'')$, without taking into account the systematic error of the intensity ratio. In this way a double counting of the systematic error of the main transition is avoided.

5.6 Results and Discussion

The following section summarizes the results of this work and compares them to the results of other authors. In the previous sections the eight strongest nitrogen transitions between 300 nm and 400 nm have been studied. These transitions emerge from just three independent electronic vibrational states, namely the $C^3\Pi_u$ state of the 2P system with vibrational levels $v' = 0, 1$ and the $B^2\Sigma_u^+$ state of the 1N system with vibrational level $v' = 0$. All transitions emerging from the same initial state show the same quenching behavior and thus depend equally on pressure and temperature, whereas the intensity ratios between these transitions remain always constant. A consistent model has been introduced in Section 2.3.4, which correctly accounts for these relations. According to this model, the fluorescence yield of a single transition, in terms of emitted photons per deposited energy, can be calculated as

$$Y_{S(v',v'')}(p, T) = Y_{S(v',0)}^0 \cdot R_{S(v',v'')} \cdot \frac{\tau_{S(v')}(p, T)}{\tau_{0S(v')}} \quad , \quad (5.30)$$

where $Y_{S(v',0)}^0$ and $\tau_{0S(v')}$ correspond to the intrinsic yield and lifetimes of the main transitions $S(v', 0)$ in the absence of collisional quenching. The intensity ratios $R_{S(v',v'')}$ refer to the main transitions $S(v', 0)$, for which $R_{S(v',0)} \equiv 1$. The reciprocal of the lifetimes $\tau_{S(v')}(p, T)$ in air can be calculated for each initial state $S(v')$ according to

$$\frac{1}{\tau_{S(v')}} = \frac{1}{\tau_{0S(v')}} + \frac{p}{kT} \cdot \sqrt{\frac{T}{293 \text{ K}}} \cdot \left[\left(0.78 \cdot Q_{\text{N}_2}^{S(v')} + 0.21 \cdot Q_{\text{O}_2}^{S(v')} \right) \cdot \left(1 - \frac{p_{\text{H}_2\text{O}}}{p} \right) + \frac{p_{\text{H}_2\text{O}}}{p} \cdot Q_{\text{H}_2\text{O}}^{S(v')} \right] \quad (5.31)$$

The factor $\sqrt{T/293 \text{ K}}$ accounts for the temperature dependence of the quenching rate constants Q , which refer to a temperature of 20 °C. A consistent set of model parameters has been determined for the investigated nitrogen transitions. These parameters are summarized in the following tables, compared with the corresponding values of other authors.

The values obtained for the intrinsic lifetime of the $2\text{P}(v' = 0)$ state is slightly smaller than the values of the more recent measurements of Pancheshnyi and Morozov et al., shown in Table 5.8. Apparently, the lifetime of the $2\text{P}(v' = 1)$ state turned out to be rather small. The reason is not well understood but it may be due to the fact, that the $2\text{P}(1,0)$ transition still contains contributions of the $2\text{P}(2,1)$ and $2\text{P}(3,2)$ transitions, which could not be separated in the analysis. On the other hand the difference to theoretical values of Gilmore et al. is of the same order as for the values of Pancheshnyi and Morozov. The intrinsic lifetime of the $1\text{N}(v' = 0)$ state has a large experimental error due to the steep decrease of the reciprocal lifetime with the pressure. Nevertheless, it agrees well with the old value, quoted by Bunner and the theoretical expectation of Gilmore et al..

The quenching rate constants at temperatures of 20 °C are summarized in Table 5.9. For nitrogen and oxygen the quenching rates for the 2P states are in good agreement to each other, except of the values of Bunner, which seem to be systematically lower. Larger differences occur for the 1N system. This may be addressed to the difficulty to separate the $1\text{N}(0,0)$ transition from contaminations of other band systems. Also for water vapor the values show large fluctuations. The reasons for this very likely are difficulties in the absolute determination of the water vapor concentration, since the water vapor attaches to the surroundings of the experiments or gets absorbed by hydrophil materials. The remarkable large value of the H_2O quenching rate constant of the $1\text{N}(v' = 0)$ state may be due to the polar nature of the colliding H_2O and N_2^+ molecules. No other published value could be found for comparison.

Only upper limits could be quoted for the quenching rate constants of argon in Table 5.4, since its contribution in air is just 1 %. Therefore the measured values for argon very likely more account for gas impurities or model deficiencies than for the true values. To clarify this question, additional measurements with larger argon fractions would be needed. The small amount of argon in the air is not expected to contribute much to the nitrogen quenching.

In Table 5.10 the intensity ratios are compared to the more recent measurements of Fons et al., the theoretical values of Gilmore et al., and the older values from Bunner, which have been derived from the fluorescence efficiencies quoted in his work. Values of Nagano et al. have not been compared, since their model does not consider the constance of the intensity ratios. The intensity ratios usually refer to the strongest transition from the initial

2P($v' = 0$)	2P($v' = 1$)	1N($v' = 0$)	Reference
38.9 ± 0.3	32.9 ± 0.5	65.2 ± 18.7	this work
42.0 ± 2.0	41.0 ± 3.0	-	Pancheshnyi et al. [36]
41.7 ± 1.4	41.7 ± 2.1	-	Morozov et al. [32]
44.5 ± 6.0	49.3	65.8 ± 3.5	Bunner [14]
37.1*	37.5*	62.3*	Gilmore et al. [20]

*Theoretical values

Table 5.8: Intrinsic (radiative) lifetimes τ_0 in nanoseconds for the initial states $C^3\Pi_u(v' = 0, 1)$ of the 2P system of and $B^2\Sigma_u^+(v' = 0)$ of 1N system.

Molecule	2P($v' = 0$)	2P($v' = 1$)	1N($v' = 0$)	Reference
N ₂	0.11 ± 0.00	0.29 ± 0.00	5.00 ± 0.17	this work
	0.13 ± 0.02	0.29 ± 0.03	-	Pancheshnyi et al. [36]
	0.12 ± 0.01	0.25 ± 0.01	-	Morozov et al. [32]
	0.10 ± 0.01	0.22 ± 0.03	3.80 ± 0.26	Nagano et al. [34]
	0.07	0.23	2.90	Bunner [14]
O ₂	2.76 ± 0.01	2.70 ± 0.03	5.24 ± 0.79	this work
	3.00 ± 0.30	3.10 ± 0.30	-	Pancheshnyi et al. [36]
	2.62 ± 0.19	2.77 ± 0.45	2.39 ± 0.40	Nagano et al. [34]
	1.35	-	8.38	Bunner [14]
H ₂ O	5.43 ± 0.12	5.78 ± 0.17	16.02 ± 1.09	this work
	3.90 ± 0.40	3.70 ± 0.40	-	Pancheshnyi et al. [36]
	7.10 ± 0.70	6.70 ± 0.70	-	Morozov et al. [32]

Table 5.9: Quenching rate constants in [$10^{-10}\text{cm}^3\text{s}^{-1}$] at 20 °C for the initial states $C^3\Pi_u(v' = 0, 1)$ of the 2P system of and $B^2\Sigma_u^+(v' = 0)$ of 1N system.

Transition	this work	Bunner [14]	Fons et al. [18]	Gilmore et al.[20]
2P(0,0) [†]	1.00 ± 0.00	1.00	1.00	1.00*
2P(0,1)	0.69 ± 0.06	0.75	0.63	0.67*
2P(0,2)	0.29 ± 0.02	0.26	0.25	0.27*
2P(1,0) [†]	1.00 ± 0.00	1.00	1.00	1.00*
2P(1,2)	0.33 ± 0.05	0.58	0.45	0.47*
2P(1,3)	0.34 ± 0.03	0.54	0.43	0.41*
2P(1,4)	0.46 ± 0.05	0.32	0.16	0.20*

[†]Main transition

*Theoretical values

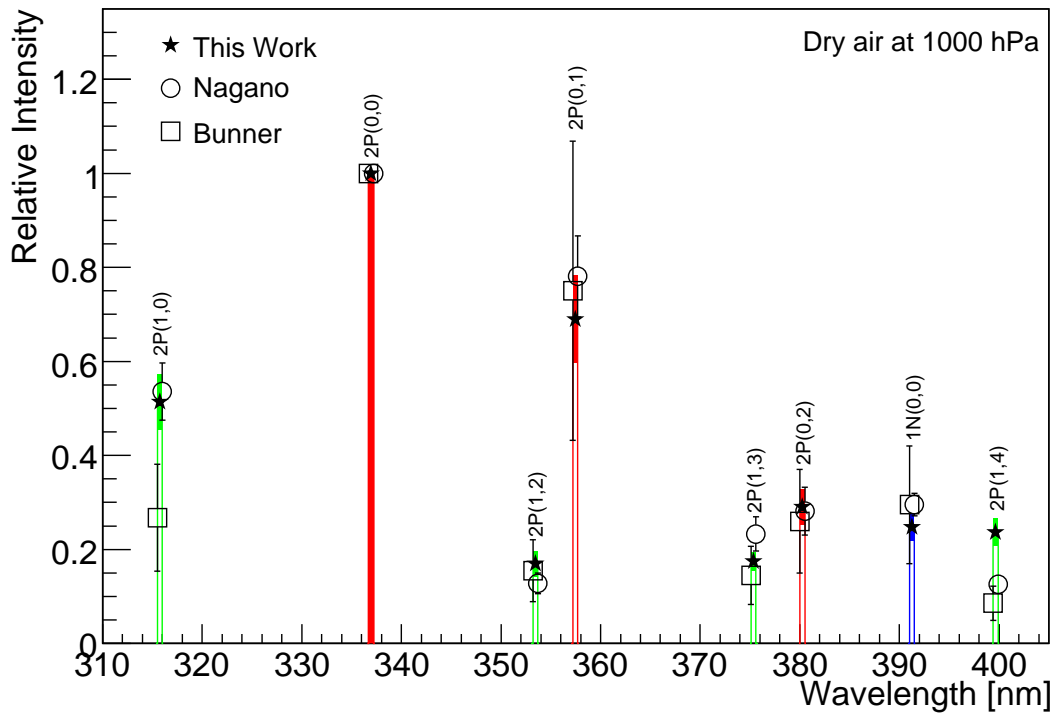
Table 5.10: Intensity ratios of the investigated transitions. Values of Bunner have been derived from the fluorescence efficiencies quoted in his work.

2P(0,0)	2P(1,0)	1N(0,0)	Reference
$0.338 \pm 0.001 \pm 0.051$	$0.172 \pm 0.001 \pm 0.023$	$1.048 \pm 0.007 \pm 0.144$	this work
$0.272 \pm 0.007 \pm 0.035$	$0.122 \pm 0.008 \pm 0.016$	$0.303 \pm 0.013 \pm 0.039$	Nagano et al. [35]

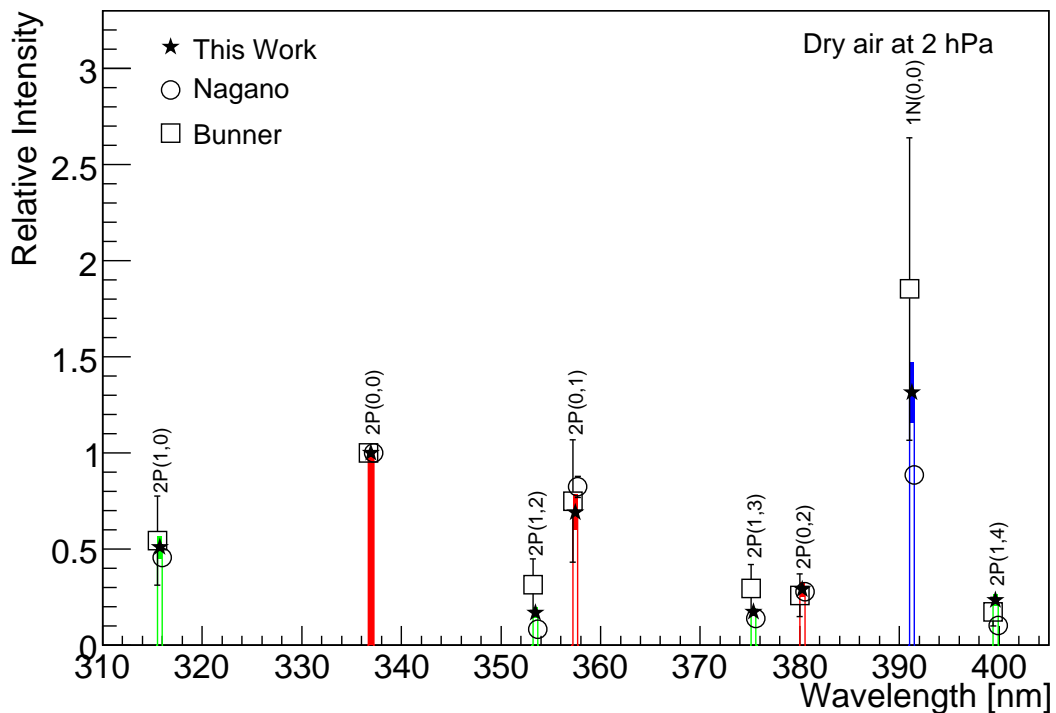
Table 5.11: Absolute values for the intrinsic fluorescence yields Y_0 in dry air for the three main transitions 2P(0,0), 2P(1,0), and 1N(0,0) in [photons/keV]. The yields are valid for an electron energy range between 250 keV and 2000 keV. The values of Nagano have been derived from values quoted at 1013 hPa.

state and are the ratio of the corresponding Einstein coefficients. The values obtained on the 2P(0, v'') transitions are in good agreement to the other measurements and to the theoretical expectations. The results of the 2P(1, v'') transitions do not match with the other authors. Qualitatively, these deviations are understood. The underestimation of the values of the 2P(1,2) and 2P(1,3) transitions stems from the fact that it was not possible to measure the pure 2P(1,0). Instead, there are some additional contributions of the 2P(2,1) and 2P(3,2) transition to this band, as has already been mentioned above at the discussion of the lifetimes. Therefore the measured intensity of the 2P(1,0) main transition is somewhat too large, which leads to the smaller values for the intensity ratios of other 2P(1, v'') transitions. An opposite effect causes the overestimation of the intensity ratio of the 2P(1,4) transition. The measured 2P(1,4) transition in this work contains additional contributions of the 2P(2,5) and the 2P(3,6) transitions, which are responsible for the larger value of the intensity ratio. Since the measurements are done with narrow band filters, the intensity ratios are also affected by the choice of the spectral shape for the individual transitions. For reasons of simplicity and to remain independent of other measurements, the spectral shape has been assumed to be rectangular with a width of 0.5 nm, as is explained in Section 5.2.4. The differences to realistic spectra in most cases have been found to be in the same order as the systematic error of the detection efficiency. The results for the lifetimes and the quenching rate constants should not depend strongly on the spectral shape, since they just rely on the time distributions.

Absolute values for the intrinsic fluorescence yields $Y_0^{S(v',0)}$ of the main transitions in dry air are listed in Table 5.11. The intrinsic fluorescence yield corresponds to the number of photons per deposited electron energy in the gas, which would be emitted in the absence of collisional quenching. The values obtained in this work are systematically larger with respect to the values of Nagano et al., which have been derived in air from the fluorescence efficiencies, quoted in terms of photons per meter of electron track length, for a mean electron energy of 850 keV. The systematic errors in this work still are rather large, since an absolute calibration has not yet been performed. The values for the intrinsic yields of the 2P system are still of the same order, whereas the intrinsic yield of the 1N(0,0) transition in this work turned out to be significantly larger than the value obtained by Nagano. The Fluorescence yields in pure nitrogen and a nitrogen oxygen mixture (90:10) have also been measured but are not listed here, since they are of no importance for air fluorescence. They roughly scale with the nitrogen fraction in the gas and are shown in Table. 5.7. An enhancement of the fluorescence yield in air due to the 1 % argon contribution as discussed by several authors [14, 22] could



(a) Dry air at 1000 hPa



(b) Dry air at 2 hPa

Fig. 5.23: Relative intensities of the investigated nitrogen bands, normalized on the 2P(0,0) transition, in dry air at 2 hPa and 1000 hPa, compared with the results of Nagano et al [35] and Bunner [14]. For better visibility of the errors, the data points of Nagano and Bunner are shifted by 0.25 nm in opposite directions. The errors of this work are represented by the colored areas around the data points.

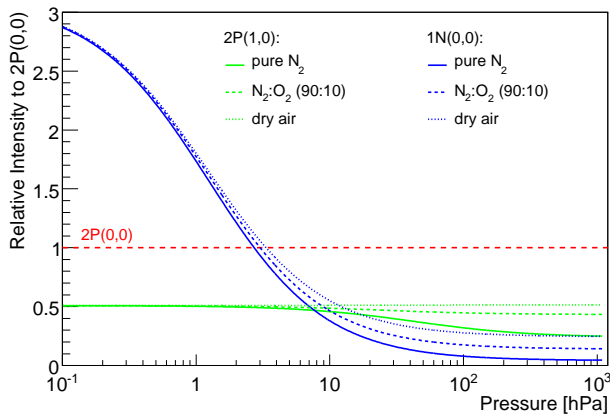


Fig. 5.24: Pressure dependence of the relative intensities of the main transitions with respect to the $2P(0,0)$ transition in the gas mixtures used for the measurements.

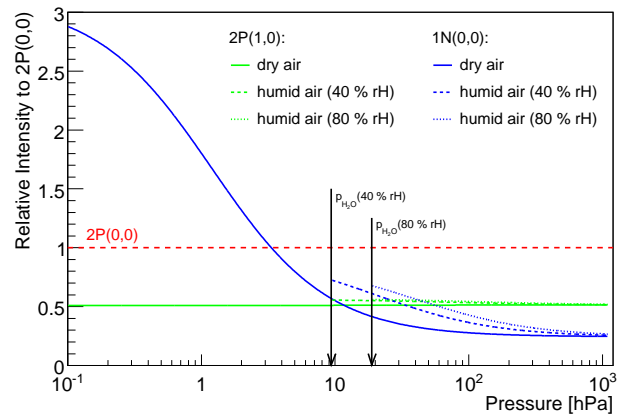


Fig. 5.25: Pressure dependence of the relative intensities in air at 20 °C with different water vapor concentrations. Pressures below the partial pressure of the water vapor are physically not allowed.

not be recognized in this work. For this purpose, additional measurements with larger argon fractions would be needed.

A relative comparison of the fluorescence spectra in dry air at 1000 hPa and 2 hPa is given in Fig. 5.23. Except of the $2P(1,0)$ and the $2P(1,4)$ transitions, a fair agreement within the errors over the whole pressure range can be stated. In the case of the $2P(1,0)$ transition the values of this work and Nagano et al. seem to agree to each other, but the value of Bunner does not. This is due to similar experimental methods used in this work and by Nagano et al.. In both cases the $2P(1,0)$ contribution could not be completely separated from the other $2P$ transitions in the same filter range. Therefore the $2P(1,0)$ transition contains additional contributions of the other transitions, which results in a similar overestimation of the $2P(1,0)$ transition in both experiments. The same problem arises for the $2P(1,4)$ transition, which also contains additional contributions of other $2P$ transitions as explained above for the intensity ratios. However, in this case Nagano was able to separate some of these transitions by the use of narrower filter bands. For pressures lower than 10 hPa significant differences between the different measurement intensities of the $1N(0,0)$ transition appear.

The variations with pressure of the relative intensities of the three main transitions with respect to the $2P(0,0)$ transition are shown in Fig. 5.24 for the three gases used in the measurements. The relative intensities at zero pressure correspond to the ratios of the intrinsic yield values. The intrinsic yield of the $1N(0,0)$ transition is three to six times larger than the intrinsic yields of the $2P$ transitions. This leads to the conclusion, that most of the nitrogen excitation are caused by ionizations. Nevertheless, the $1N(v' = 0)$ state is also strongly affected by the collisional quenching, and thus the net effect of the $1N(0,0)$ transition to the total fluorescence is relatively small at pressures higher than 10 hPa. The addition of oxygen or other quench gases enhances the relative intensities of the $1N(0,0)$ but also of the $2P(1,0)$ transition. This is because the corresponding states are already more affected by the

nitrogen self quenching than the $2P(v' = 0)$ state and therefore the relative increase of their quenching rates is smaller. In dry air the total quenching rates of the $2P(v' = 1)$ state and the $2P(v' = 0)$ state happen to be almost the same and thus the intensity ratios between the corresponding transitions remain nearly equal over the whole pressure range. Addition of a certain amount of water vapor leads to a slight increase of the relative intensity of the $2P(1,0)$ transition in air, as is illustrated in Fig. 5.25. Especially the $1N(0,0)$ transition gets more pronounced in humid air, since it is less affected by the water vapor quenching than the $2P$ transitions.

Chapter 6

Summary and Outlook

Within this thesis the energy and pressure dependence of the nitrogen fluorescence yield in air has been studied for electron energies between 250 keV and 2000 keV and pressures ranging from 2 hPa to 950 hPa. A precise knowledge of the fluorescence yield in air is necessary to enable the correct determination of the deposited energy in extensive air showers, which have been measured by fluorescence telescopes.

The AirLight experiment has been built up in order to perform the fluorescence yield measurements. It consists of a cylindrical chamber, where electrons from a ^{90}Sr -source are entering along the chamber axis. Seven photomultipliers, equipped with narrow band interference filters, are mounted perpendicular to the chamber axis to detect the induced fluorescence photons in different wavelength ranges. The complete experimental setup has been designed and developed in cooperation with the technicians of our institute. A big part of the time was spent for the development of the data acquisition system including the programming of the experimental control. Furthermore, appropriate calibration procedures have been developed and applied to the data. A complete GEANT4 simulation of the experiment was written in order to obtain precise information about the angular distributions of the photons, the acceptance of the photon detectors, the pressure dependence of the electron energy spectra as well as the energy deposit in the chamber.

The eight strongest nitrogen transitions have been measured simultaneously for different pressures. A new description of the nitrogen fluorescence yield has been introduced, which correctly accounts for all relations between the individual nitrogen bands. The basic properties of this model are:

- Separation of excitation and de-excitation processes.
- The investigated transitions can be subdivided into the three sub-spectra $2\text{P}(v' = 0)$, $2\text{P}(v' = 1)$, $1\text{N}(v' = 0)$.
- Transitions from the same sub-spectrum are emerging from the same initial electronic-vibrational state.
- All transitions within a sub-spectrum have the same excitation- and quenching-cross-sections and thus behave totally equal for different pressures and electron energies.

- The intensity ratios between transitions of the same sub-spectrum are constant and are given by the ratio of their Einstein-coefficients.

According to this model, the measured data has been analyzed in two steps. First of all the de-excitation parameters, such as intrinsic lifetimes, quenching rate constants, and intensity ratios, have been determined by sophisticated χ^2 -minimizations, globally applied to the complete data sample. In this way a consistent set of parameters, including their correlations, has been obtained. These parameters completely describe the relative intensity variations of the three sub-spectra with pressure and temperature. Additionally the influence of water vapor on the nitrogen quenching has been analyzed.

In the second step, the absolute values of the intrinsic fluorescence yields for each sub-spectrum have been determined for different energy ranges between 250 keV and 2000 keV. The intrinsic fluorescence yields turned out to be constant over the whole energy range even for energies below 500 keV, where the electrons cannot be considered anymore as minimal ionizing particles. Therefore it can be stated, that the number of emitted fluorescence photons in this energy range is proportional to the energy deposit in the air. Nevertheless, slight pressure variations of the intrinsic fluorescence yields in the order of 7 % in air have been observed but the reason is not yet understood. This effect is not expected to be a real physical property of the fluorescence yield. It is more likely due to experimental problems or related to the simulation. The total systematic uncertainty of the absolute fluorescence yields turned out to be in the order of 15 %. This relatively large error is due to the still missing absolute calibration of the experiment, which is planned to be done in the near future. With an appropriate absolute calibration the systematic error is expected to adopt a value in the order of 10 %.

Acknowledgements

I am deeply indebted to Prof. Dr. J. Blümer who gave me the possibility to enter into this interesting topic and who provided support whenever needed.

Many thanks also to Prof. Dr. G. Quast for taking over the report as co-referee at short notice.

I would like to express my deep gratitude to Dr. H. Klages for supervising my work and for always supporting my activities.

I am very grateful to Dr. R. Engel for the support and his helpful suggestions.

It is a pleasure for me to thank Dr. M. Unger for his help and support in statistical matters and for the careful reading and correcting of this manuscript.

I am indebted to G. Wörner who constructed the whole experimental structure and for his patience with me and my special requests.

For the very pleasant working atmosphere, I want to thank all the personnel of the *Institut für Kernphysik* at Forschungszentrum Karlsruhe and especially the members of the Auger group.

I would like to thank Simone for her patience and the careful revision of my English skills.

Finally, I would like to thank my family for the support especially during the last few months of this work.

Bibliography

- [1] *GEANT4: Physics Reference Manual*, <http://geant4.web.cern.ch/geant4>.
- [2] J. ABRAHAM ET AL., *Properties and performance of the prototype instrument for the Pierre Auger Observatory*, Nucl. Instrum. Meth., A523 (2004), pp. 50–95.
- [3] S. AGOSTINELLI ET AL., *GEANT4: A simulation toolkit*, Nucl. Instrum. Meth., A506 (2003), pp. 250–303.
- [4] F. A. AHARONIAN AND J. W. CRONIN, *Influence of the universal microwave background radiation on the extragalactic cosmic ray spectrum*, Phys. Rev., D50 (1994), pp. 1892–1900.
- [5] C. ANDERSON, Phys. Rev., 43 (1933), p. 491.
- [6] P. AUGER, Rev. Mod. Phys., 11 (1938), p. 288.
- [7] H. BEHRENS AND J. JÄNECKE, *Numerical Tables for Beta-Decay and Electron Capture*, vol. 4, Springer-Verlag Berlin, Heidelberg, New York, 1969.
- [8] H. BEHRENS AND L. SZYBISZ, *Shapes of Beta Spectra*, vol. 6-1 of Physics Data, Zentralstelle für Atomkernenergie-Dokumentation, 1976.
- [9] W. A. BINGEL, *Theorie der Molekülspektren*, Verlag Chemie GmbH, Bergstraße, Weinheim, 1967.
- [10] D. J. BIRD ET AL., *The Cosmic ray energy spectrum observed by the Fly’s Eye*, Astrophys. J., 424 (1994), pp. 491–502.
- [11] V. BLOBEL AND E. LOHRMANN, *Statistische und numerische Methoden der Datenanalyse*, Teubner, Stuttgart, Leipzig, 1998.
- [12] J. BLÜMER, *Cosmic rays at the highest energies and the Pierre Auger Observatory*, J. Phys., G29 (2003), pp. 867–879.
- [13] R. BRUN AND F. RADEMAKERS, *ROOT: An object oriented data analysis framework*, Nucl. Instrum. Meth., A389 (1997), pp. 81–86.

-
- [14] A. N. BUNNER, *Cosmic Ray Detection by Atmospheric Fluorescence*, PhD thesis, Graduate School of Cornell University, February 1967.
- [15] W. DEMTRÖDER, *Experimentalphysik 3, Atome, Moleküle und Festkörper*, Springer-Verlag, Berlin Heidelberg New York, 1996.
- [16] R. ENGEL, *Very High Energy Cosmic Rays and Their Interactions*, Nuclear Physics B (Proc. Suppl.), 151 (2006), pp. 437–461.
- [17] R. W. ENGSTROM, *Photomultiplier Handbook*, RCA Corporation, 1980.
- [18] T. J. FONS, R. S. SCHAPPE, AND C. C. LIN, *Electron-impact excitation of the second positive band system ($C^3\Pi_u \rightarrow B^3\Pi_g$) and the $C^3\Pi_u$ electronic state of the nitrogen molecule*, Phys. Rev. A, 53 (1996), pp. 2239–2247.
- [19] T. GAISSER, *Cosmic Rays and Particle Physics*, Cambridge University Press, 1990.
- [20] F. GILMORE, R. R. LAHER, AND P. J. ESPY, *Franck-Condon factors, r -centroids, electronic transition moments, and Einstein coefficients for many nitrogen and oxygen band systems*, J. Phys. Chem. Ref. Data, 21 (1992), p. 1005.
- [21] K. GREISEN, *End to the cosmic ray spectrum?*, Phys. Rev. Lett., 16 (1966), pp. 748–750.
- [22] A. E. GRÜN AND E. SCHOPPER, Z. Naturforschg., 9a (1954), p. 134.
- [23] H. HAKEN AND H. C. WOLF, *Molekülphysik und Quantenchemie*, Springer-Verlag, Berlin Heidelberg New York, 1992.
- [24] D. HECK, J. KNAPP, J. N. CAPDEVIELLE, G. SCHATZ, AND T. THOUW, *CORSIKA: A Monte Carlo Code to Simulate Extensive Air Showers*, Report FZKA, 6019 (1998).
- [25] V. HESS, Z. Phys., 13 (1912), p. 1084.
- [26] F. JAMES AND M. ROOS, *'MINUIT' A system for function minimization and analysis of the parameter errors and correlations*, Comput. Phys. Commun., 10 (1975), pp. 343–367.
- [27] F. KAKIMOTO ET AL., *A Measurement of the air fluorescence yield*, Nucl. Instrum. Meth., A372 (1996), pp. 527–533.
- [28] K. KAMPERT ET AL., *Cosmic ray energy spectra and mass composition at the knee: Recent results from KASCADE*, Nucl. Phys. Proc. Suppl., 136 (2004), pp. 273–281.
- [29] S. KLEPSE, *Optische Elemente des AirLight-Experiments zur spektralen Messung der Fluoreszenzausbeute von Luft*, Master's thesis, Universität Karlsruhe, Institut für Experimentelle Kernphysik, 2004.

-
- [30] W. R. LEO, *Techniques for Nuclear and Particle Physics Experiments*, Springer-Verlag, 1994.
- [31] A. LETESSIER-SELVON, *Ultra high energy cosmic rays and the Auger observatory*, To appear in the Proc. of 25th Int. Symposium on Physics in Collision (PIC 05), eprint: astro-ph/0510627, (2005).
- [32] A. MOROZOV, R. KRÜCKEN, J. WIESER, AND A. ULRICH, *Gas kintec studies using a table-top set-up with electron beam excitation: quenching of molecular nitrogen emission by water vapor*, Eur. Phys. J. D, 33 (2005), pp. 207–211.
- [33] F. W. MURRAY, *On the Computation of Saturation Vapor Pressure*, J. Appl. Meteorol., 6 (1967), pp. 203–204.
- [34] M. NAGANO, K. KOBAYAKAWA, N. SAKAKI, AND K. ANDO, *Photon yields from nitrogen gas and dry air excited by electrons*, Astropart. Phys., 20 (2003), pp. 293–309.
- [35] M. NAGANO, K. KOBAYAKAWA, N. SAKAKI, AND K. ANDO, *New measurement on photon yields from air and the application to the energy estimation of primary cosmic rays*, Astropart. Phys., 22 (2004), pp. 235–248.
- [36] S. V. PANCHESHNYI, S. M. STARIKOVSKAIA, AND A. Y. STARIKOVSKII, *Collisional deactivation of $N_2(C^3\Pi_u, v = 0, 1, 2, 3)$ states by N_2 , O_2 , H_2 and H_2O molecules*, Chem. Physics, 262 (2000), pp. 349–357.
- [37] R. W. B. PEARSE AND A. G. GAYDON, *The Identification of Molecular Spectra*, Chapman and Hall Ltd, 11 New Fetter Lane, London EC4P 4EE, 1976.
- [38] W. H. PRESS ET AL., *Numerical Recipes in C. The Art of Scientific Computing*, Cambridge University Press, New York, 1992.
- [39] M. RISSE, *private communication*.
- [40] M. RISSE AND D. HECK, *Energy release in air showers*, Astropart. Phys., 20 (2004), p. 661.
- [41] S. M. SELTZER AND B. M. J., *Evaluation of the Collision Stopping Power of Elements and Compounds for Electrons and Positrons*, Int. J. Appl. Radiat. Isot., 33 (1982), pp. 1189–1218.
- [42] K. SHINOZAKI AND M. TESHIMA, *AGASA results*, Nucl. Phys. Proc. Suppl., 136 (2004), pp. 18–27.
- [43] R. W. SPRINGER, *Recent results from the HiRes air fluorescence experiment*, Nucl. Phys. Proc. Suppl., 138 (2005), pp. 307–309.
- [44] A. ULRICH, *private communication*.

- [45] H. ULRICH, *Untersuchungen zum Primären Energiespektrum der kosmischen Strahlung im PeV-Bereich mit dem KASCADE-Experiment*, PhD thesis, University of Karlsruhe (TH), Forschungszentrum Karlsruhe, 2004.
- [46] G. M. VOSE AND G. WILLIAMS, *LabVIEW: Laboratory Virtual Instrument Engineering Workbench*, byte, (1986), pp. 84–92.
- [47] J. WEFEL, *Cosmic Rays, Supernovae and the Interstellar Medium*, NATO ASI Series, 337C (1991), p. 29.
- [48] G. ZATSEPIN AND V. KUZMIN, *Upper limit of the spectrum of cosmic rays*, JETP Lett., 4 (1966), pp. 78–80.